Switching processes in mesoscopic systems

Im Fachbereich Physik
der Freien Universität Berlin
eingereichte

Dissertation

von

Elina Locane

Berlin, im Februar 2018

1. Gutachter: Prof. Dr. Piet W. Brouwer
2. Gutachter: Prof. Felix von Oppen, PhD

Tag der Einreichung: 16. Februar 2018
Tag der Disputation: 20. März 2018

Selbstständigkeitserklärung

Hiermit versichere ich, dass ich in meiner Dissertation alle Hilfsmittel und Hilfen angegeben habe, und auf dieser Grundlage die Arbeit selbstständig verfasst habe. Diese Arbeit habe ich nicht schon einmal in einem früheren Promotionsverfahren eingereicht.

Kurzfassung

Schaltprozesse sind in Natur und Technik allgegenwärtig. Beispiele liefern Rezeptorschalter in Zellmembranen oder Halbleitertransistoren, die in fast allen elektronischen Geräten vorkommen. Schalter spielen eine wichtige Rolle in Kommunikationsprozessen, da ihre diskreten Zustände eine erhöhte Rauschtoleranz zur Folge hat.

Ein anderer Aspekt der Informationsverarbeitung ist die seit sechzig Jahren fortschreitende Miniaturisierung von integrierten Schaltungen. Die Größe der Bauelemente erreicht mittlerweile Dimensionen, bei denen Quanteneffekte wie Interferenz oder die Ladungsquantisierung relevant werden. Es ist daher nötig, zu untersuchen, wie elektronische Bauteile auf sehr kleinen Längenskalen funktionieren.

Diese Dissertation verbindet die beiden genannten Aspekte und betrachtet verschiedene Schaltprozesse auf der Nanoskala. Dabei sind Schaltprozesse schon in der diskreten Natur von quantenmechanischen Systemen eingebaut — wie zum Beispiel durch Energie- oder Spinquantisierung. Im Folgenden betrachten wir drei verschiedene Modelle, die Schaltprozesse involvieren.

Im ersten Fall geht es um den Spin von Elektronen. Die Möglichkeiten zur Kontrolle und Manipulation von Spins haben das Feld der Spintronik hervorgebracht, welches Spins für Informationsaustausch und -verarbeitung benutzen möchte. In dieser Arbeit untersuchen wir das Schalten von Spins auf topologischen Isolatoren durch Oberflächenströme. In diesen Materialien erlaubt die perfekte Korrelation von elektronischem Impuls und Spin ohne externe Magnetfelder auszukommen und ermöglicht eine im Vergleich zu anderen Materialien erhöhte Effizienz.

Ein anderes Modell stammt aus dem Feld der elektronischen Quantenoptik, welche versucht quantenoptische Experimente mit Elektronen anstatt mit Photonen zu reproduzieren. Wir untersuchen, wie das abrupte Schalten eines Quantenpunktkontakts als Teil eines Protokolls für Elektronentomographie die Form des transmittierten Wellenpakets beeinflusst. Insbesondere untersuchen wir, wie sich die Wignerfunktion des Wellenpakets während Streuung an verschiedenen Potentialen verändert und leiten einen quantenmechanischen Ausdruck für die durch den Quantenpunktkontakt transmittierte Ladung her.

Ein drittes Modell ist der Einzel-Molekül-Transistor. Die Motivation für unsere Arbeit besteht aus einer experimentell beobachteten Leitfähigkeitslücke im Basisspannungs-Vorspannungs-Diagramm, welche nicht durch die Theorie des Ein-Elektronentransistors erklärbar ist. Wir modifizieren das Modell, indem wir für das Molekül verschiedene Konformationen mit unterschiedlich geladenen Niedrigenergiezuständen annehmen. Diese Modifikation kann die experimentellen Resultate qualitativ erklären. Der Einzel-Molekül-Transistor kann auf zwei Arten als Schalter verstanden werden — zunächst im konventionellen Sinne als auch als konformativer Schalter, der durch die angelegten Spannungen kontrolliert werden kann.

Abstract

Switching processes are widespread in nature and technology, from receptor switches in cell membranes to semiconductor transistors present in almost every electronic device today. They play a crucial role in communication, since the inherent discreteness of these processes leads to higher noise tolerance compared to analog communication.

Another observation concerning information processing is the rapid miniaturization of integrated circuits that has taken place during the past six decades. The size of the components of an electronic device is reaching the regime where quantum interference and charge quantization become important. It is therefore necessary to investigate how electronic devices function at very small size scales.

This thesis connects the two aforementioned aspects and looks at different switching processes at the nanoscale. The discrete nature of quantum mechanical systems, such as energy and spin quantization, often provides a setting where some kind of switching is built-in. We look at three different models that involve switching.

The first one is concerned with electron spin. The possibility to control and manipulate it has created the field of spintronics that aims to use the spin degree of freedom for information transfer and processing. In this work we investigate the switching of spins on the surface of a topological insulator by passing a current through the surface. The perfect correlation between electron spin and momentum on topological insulator surfaces provides a handle for the spin without the need to apply a magnetic field. The spin-momentum locking also increases the efficiency of the mechanism compared to other materials.

Another model we investigate stems from electron quantum optics, a field that aims to reproduce quantum optics experiments with electrons instead of photons. We look at how an abrupt switching of the conductance of a quantum point contact affects the shape of a transmitted wave packet as part of a protocol for electron tomography. In particular, we investigate how the Wigner function of the wave packet transforms during scattering off different potentials and derive a quantum mechanical expression for the transmitted charge through a quantum point contact under the influence of the potential.

A third model we look at is that of a single-molecule transistor. The motivation for this is an experimentally observed conductance gap in the gate voltage-bias voltage diagram that differs from the expected single-electron transistor picture. We introduce a modification in the model by allowing the molecule to be in different conformations whose lower-energy states are differently charged. This leads to a qualitative agreement with the experimental results. This single-molecule transistor can be regarded as a switch in two aspects—in the conventional transistor sense, as well as a conformational switch that can be controlled with the gate or bias voltage.

Contents

1. Introduction

Many systems involving information transfer and processing—both in nature and in technology—rely on digital signals. Their discreteness leads to less noise, lower error rates, and more stability. Examples of such systems include DNA molecules that carry genetic information using four different nucleobases, as well as signal transfer in neurons via the action-potential—an electrochemical pulse that operates on an all-or-none principle and only depends on whether the signal that caused it exceeded a certain threshold. In technology, discrete signals are ubiquitous and nowadays almost all electronic computation is digital—information is stored and processed as strings of ones and zeros. The most widespread physical realizations of these binary information units are transistors acting as switches and magnetic domains whose magnetization can point in two different directions, representing the two possible states of a bit. With the miniaturization of electronics starting to reach size scales where quantum mechanical effects such as charge quantization and interference play a role, it is necessary to understand the implications of quantum physics in nanoscale devices. In this context, the present thesis is concerned with switching processes in mesoscopic systems. In particular, we look at three different models where some form of switching—either of spin state, molecular conformation, or an abrupt change in point contact conductance—takes place. We introduce the background for each of the three models in the following sections.

1.1. Switching magnetic moments

In Chapter 2, we investigate the possibility of switching a spin coupled to the surface or edge of a topological insulator (TI) by passing a current through the surface/edge. Manipulation of individual spins is one of the main goals of spintronics, a field that has developed considerably since its beginnings in the 1980s and the discovery of the giant magnetoresistance [Baib 88, Bina 89]. Its success has enabled an exponential increase in hard disk drive memory density. The principle behind information readout in hard disk drives is the spin-dependent scattering in magnetic materials. When passing a current through a material consisting of alternating thin magnetic and non-magnetic layers, the resistance will depend considerably on whether the magnetic layers have parallel or antiparallel magnetization. This enables the detection of the magnetization of a region on the hard disk drive by measuring the resistance through the readout head as one of its magnetic layers is kept constant but the other is magnetized in the same direction as the region on the drive. Recently, the tunnel magnetoresistance effect has made it possible to improve the readout sensitivity even more. In 2008, a tunnel magnetoresistance of 604% at room temperature was observed [Iked 08].

For information storage (as opposed to readout), magnetic fields are commonly used to change the magnetization of a memory domain, but other ways to control magnetization

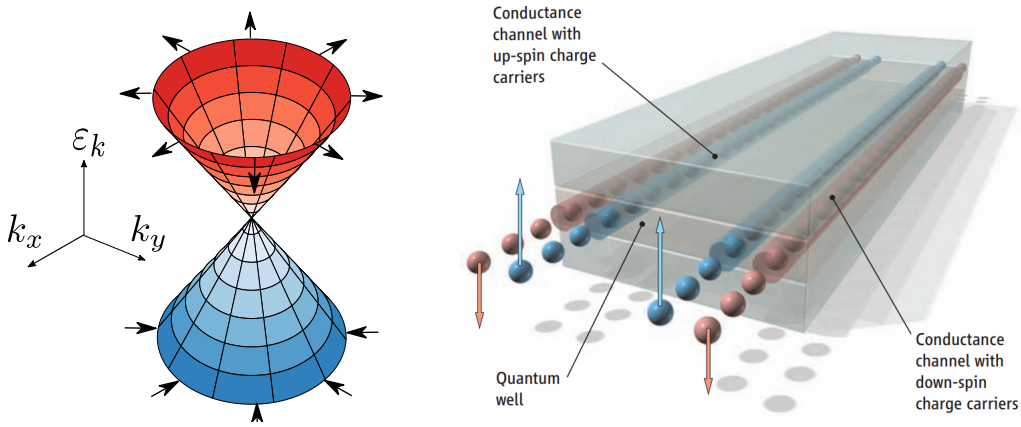

Figure 1.1.: Left: Dispersion of the surface states of a three-dimensional topological insulator and the respective spin polarization, denoted by the arrows. Right (figure from [Koni 07]): a schematic of the spin-polarized edge states corresponding to the one-dimensional version of Eq. (1.1) and exhibiting conducting edge channels in which electrons with opposite spin projections propagate in opposite directions.

are also being investigated. In particular, the spin-transfer torque [Ralp 08], predicted by Berger [Berg 96] and Slonczewski [Slon 96] in 1996, has gained considerable attention and provides a way to switch magnetization with lower current densities than those needed for approaches with magnetic fields. In this setting, spin-polarized currents are passed through magnetic layers to switch their orientation. Initially, the strength of the current required to move a magnetic domain wall was unrealistically high (tens of amperes), but with the ability to produce smaller samples, these values have decreased to milliamperes. And as the size of technological devices keeps shrinking, it becomes relevant to explore different ways to control not just layers of magnetic materials, but individual spins. An efficient way to produce spin-polarized currents is also required.

With this goal in mind, in this thesis we look at spins coupled to topological insulator surfaces. The reason why this combination could be promising is the perfect correlation of the spin and momentum of the electrons on TI surfaces. In the most general sense, topological systems are ones whose Hamiltonians cannot be continuously transformed into that of vacuum without closing a gap in the spectrum. This means that if two topologically different insulators are in contact, the interface between them will be conducting. Thus, in the context of insulators, a sufficient definition of a topological insulator is that it should exhibit symmetry-protected conducting surface states while the bulk remains insulating. The closing of the energy gap in the vicinity of the band touching point (for a two-dimensional surface) can be approximated with a linear effective Hamiltonian,

$$H = \hbar v \sigma \cdot \mathbf{k}, \tag{1.1}$$

where v is the Fermi velocity, $\sigma = (\sigma_x, \sigma_y, \sigma_z)$ are the Pauli matrices, and $\mathbf{k} = (k_x, k_y, 0)$ is the momentum of the surface electrons. The eigenstates of such a Hamiltonian have the

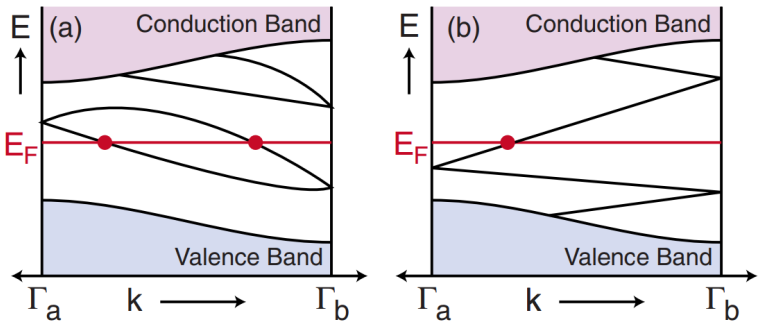

Figure 1.2.: The dispersion of the surface states of a trivial (left) and a non-trivial topological (right) insulator between the two time-reversal-symmetric momenta of the Brillouin zone, Γ_a=0 and $\Gamma_b = \pi/a$. In the first case, the states always cross the Fermi energy E_F an even number of times, whereas in the second case the number is always odd. Figure taken from [Hasa 10].

spin of an electron pointing in the direction of its momentum, as illustrated in Fig. 1.1. This means that the spin of the surface electrons is determined by their momentum, and, if we can control their momentum, we can in turn control their spin. Since the momentum of charged particles can be changed by applying an electric field, this provides a way to control magnetic degrees of freedom with electric fields.

The spin-polarized surface states of topological insulators are protected by time-reversal symmetry and arise from spin-orbit coupling [Fu 07, Hasa 10]. Spin-orbit interaction splits the spin-up and spin-down degeneracy in the whole Brillouin zone, except for the time-reversal-invariant momenta 0 and π/a, where a is the lattice constant. Depending on the way these time-reversal-invariant points are connected, the number of surface states at the Fermi energy can be either even or odd, see Fig. 1.2. The case of an even number of surfaces states at the Fermi energy corresponds to a trivial insulator, and an odd number of suface states corresponds to a topological insulator. A transition between the two is not possible without closing the energy gap in the bulk spectrum, and these two different cases lead to a $\mathbb{Z}_2$ classification of topological insulators [Schn 08, Kita 09, Schn 09].

The first proposals considered graphene as a candidate for a two-dimensional topological insulator, but the spin-orbit interaction in graphene turned out not to be sufficiently strong. HgCdTe quantum wells (two-dimensional materials consisting of layers of CdTe/HgTe/CdTe) are a much more suitable material due to the heavy elements with strong spin-orbit coupling, as well as the p and s level inversion in HgTe. The conduction and valence bands in HgTe are inverted in comparison to CdTe—the hole band is the conduction band and the electron band is the valence band, as shown schematically in Fig. 1.3. However, below a certain layer thickness d_c, these bands switch again due to confinement. It was predicted by Bernevig *et al.* [Bern 06] that a phase transition from a trivial insulator with vanishing conductance to a topological insulator with a quantized conductance would take place as the thickness of the HgTe layer is varied from below d_c to above d_c. In the latter case, the edge states could be described with the one-dimensional

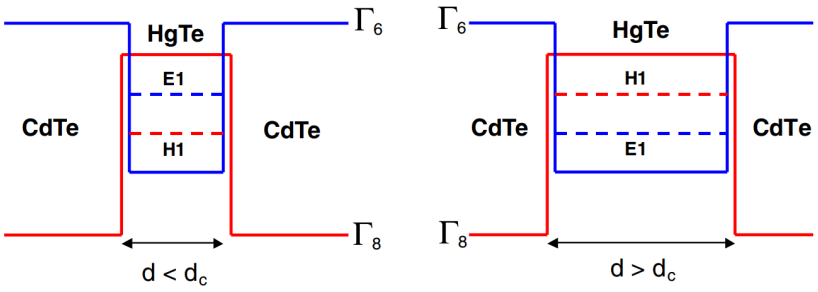

Figure 1.3.: A schematic of the conduction and valence bands in HgCdTe quantum wells below (left) and above (right) the critical HgTe thickness d_c. When the thickness is above d_c, the bands in HgTe are inverted in comparison with CdTe, in which case the material will have conducting edge states. Figure taken from [Koni 08].

version of Eq. (1.1) and correspond to helical channels in which spin-up electrons move in one direction, and spin-down electrons in the opposite direction. This two-dimensional topological insulator phase is known as the quantum spin Hall insulator and was observed experimentally by König *et al.* in 2007 [Koni 07]. In this experiment, the longitudinal resistance of HgCdTe quantum well structures at zero magnetic field and temperature $T = 30$ mK was measured as the gate voltage was varied, scanning through different Fermi energies from below to above the bulk conductance gap. The results for different representative samples are shown in Fig. 1.4. The black curve, denoted by I, corresponds to a sample in which the thickness of the HgTe layer is below the critical $d_c \approx 6.3$ nm. The plateau corresponds to the Fermi energy being in the gap, and the resistance in this case is above 10^7 Ω, reaching the detection limit of the measurement device. This is in accordance with the expectation that below the critical thickness the material should be a trivial insulator with a conductance gap in the bulk as well as the edge. When the HgTe layer thickness is larger than 6.3 nm (the blue (II), the green (III), and the red (IV) curves), the resistance is finite and corresponds to the conductance quantum $2e^2/h$ for small enough sample lengths (red and green curves). When a magnetic field is applied to the sample, this residual conductance is removed, indicating that the conducting edge states are protected by time-reversal symmetry.

The red and green curves in Fig. 1.4 differ only by the width of the sample, and exhibit the same residual conductance. This indicates that the current must be flowing at the edges of the sample. A more direct experimental proof of this fact was provided by Nowack *et al.* [Nowa 13], using superconducting quantum interference devices to measure the magnetic field produced by the currents flowing in the sample. They showed that all transport indeed takes place only at the edges. However, the spin-polarized nature of the edge states of a quantum spin Hall system has not yet been shown directly. For three-dimensional topological insulators, this has been done with spin- and angle-resolved photoemission spectroscopy (spin-ARPES) [Hsie 09b, Hsie 09a]. An example of such a measurement for the surfaces of the topological insulators Bi_2Se_3 and Bi_2Te_3 is shown in

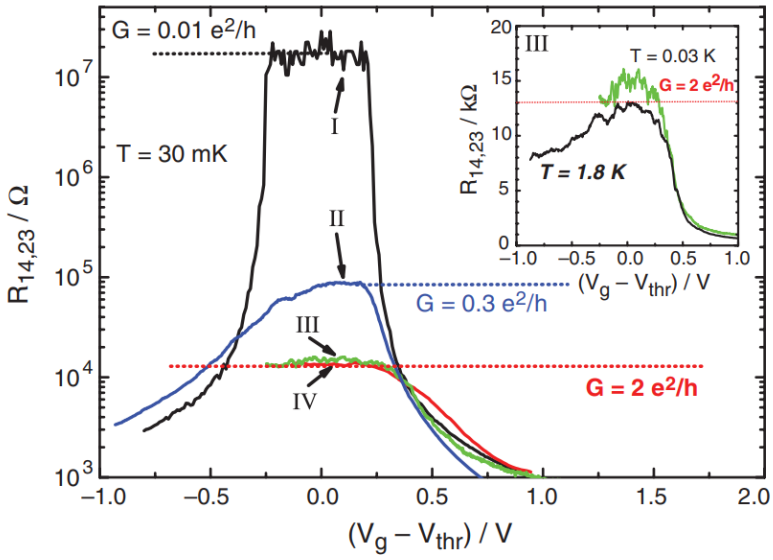

Figure 1.4.: Longitudinal resistance of a HgCdTe quantum well structure as a function of the gate voltage for a sample with HgTe layer thickness of 5.5 nm (black curve (I)) and 7.3 nm (blue (II), green (III), and red (IV) curves). The sample sizes are 20.0×13.3 µm^2 for curves I and II, 1.0×1.0 µm^2 for sample III, and 1.0×0.5 µm^2 for sample IV. The measurements were performed at zero magnetic field and $T = 30$ mK. The inset shows the sample III at two different temperatures $T = 30$ mK and $T = 1.8$ K. Figure taken from [Koni 07].

Fig. 1.5. The upper panels show the signal intensity and spin projection at the Fermi energy and the two lower panels show the electronic dispersion at a fixed momentum k_y. This confirms the Dirac-like nature and the spin-momentum locking of the surface electrons. Unlike the quantum spin Hall system, three-dimensional topological insulators have also been shown to exist at room temperature.

The spin-momentum locking of the surface states of TIs has already been employed to switch the magnetization of nanomagnets and thin films coupled to TI surfaces. For example, the magnetization of a thin permalloy layer in contact to a Bi_2Se_3 layer could be switched by passing an in-plane current through the surface of Bi_2Se_3 [Mell 14], and the spin-transfer torque per unit current density exerted on the permalloy layer was larger than achieved with any other approach. Therefore the typical current density needed for magnetization switching in setups involving topological insulators is orders of magnitude smaller than that required with other methods. It is expected that the current densities needed to switch individual spins would be even lower, making the potential applications in memory devices very efficient.

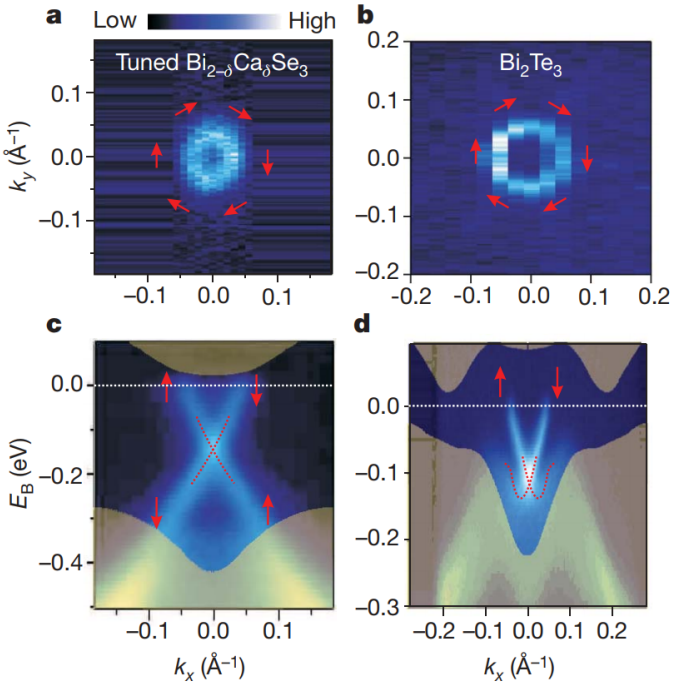

Figure 1.5.: Upper panels: Spin-ARPES measurement data for Bi_2Se_3 (left) and Bi_2Te_3 (right) at the Fermi energy, with the red arrows indicating the spin projection. Lower panels: Dispersion of the surface states of Bi_2Se_3 (left) and Bi_2Te_3 (right) at a fixed k_y, with the red arrows indicating spin projection. Figure taken from [Hsie 09a].

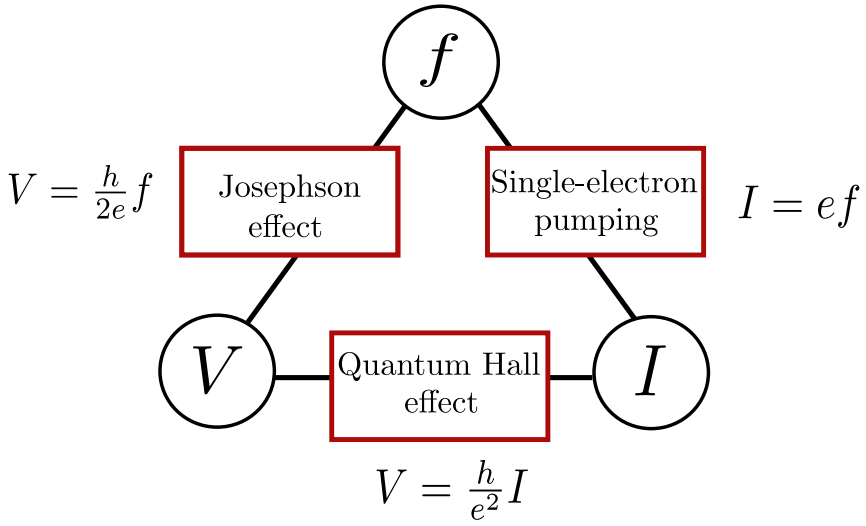

Figure 1.6.: The quantum metrological triangle connecting voltage, current, and frequency through three quantum experiments and the fundamental constants h and e. Connecting these three experiments (for example, by passing the current from a single-electron pump through a quantum Hall edge and measuring the Josephson voltage created by this current) provides a consistency check for h and e, as well as a new way to define electrical units.

1.2. Electron quantum optics

In Chapter 3, we consider electron scattering in quantum Hall edge states in a time-dependent potential. Among the different time-dependences that we look at is also a sharp step-like change in the value of the potential. This kind of sudden ramp can be used in electron wave packet detection to probe the arrival time distribution of the wave packet. By making the potential step very high such that no electrons can be transmitted after the voltage has been switched on and by varying the time at which this is done, one can measure what part of the wave packet arrives before a certain time, and therefore obtain the cumulative probability distribution, from which the arival time distribution follows.

Another application for a sharp voltage signal—if applied periodically—is charge pumping, a controlled emission of electrons from a quantum dot one by one at a constant rate. If done at a very high frequency and with high accuracy, this could serve as a new standard for the ampere. Together with the resistance standard based on the quantum Hall effect and the voltage standard based on the Josephson effect, this forms the quantum metrological triangle [Piqu 04, Kell 08, Milt 10, Sche 12], see Fig. 1.6. The quantum metrological triangle was first proposed in 1985 [Likh 85] and provides a consistency check for the fundamental constants h and e. It connects voltage, current, and frequency through quantum effects with coefficients that only contain h and e. It could therefore be possible to define the units of ohm, volt, and ampere by fixing the value of h and e. This is desirable because it would decouple the standard of the ampere from the standard of the kilogram, which is

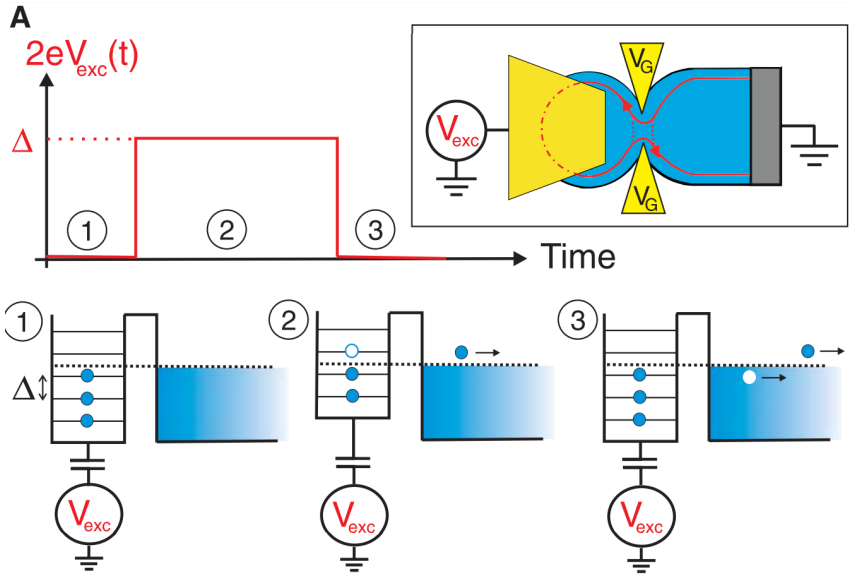

Figure 1.7.: Schematics for single-electron pumping carried out in [Feve 07]. Top left: the gate voltage V_{exc} used to shift the energy levels of the quantum dot as a function of time. Top right: The setup of the experiment. A quantum dot (circular red line) is connected to quantum Hall edge channels via a tunnel barrier controlled by the gate voltages V_G. The levels of the dot are tuned using V_{exc}. Bottom: The three stages of the pumping cycle. Figure taken from [Feve 07].

still based on the platinum-iridium cylinder stored by the International Bureau of Weights and Measures in France since 1889. The extremely accurate quantization (at least 1 part in 10^9) in the quantum Hall and the Josephson effects has already made possible the use of the new units of ohm and volt defined in the General Conference of Weights and Measures in 1990. The accuracy of the single-electron pumping experiments is currently the weak link of the quantum metrological triangle due to the inherently statistical nature of electron tunneling, and metrology institutes are working towards increasing it.

Single-electron pumps are made of quantum dots—effectively zero-dimensional regions of space with discrete electronic energy levels—that are operated by varying some external parameters (usually gate and/or bias voltages) in a periodic manner such that exactly one electron is released from the dot each cycle. An example of such a charge pump is shown in Fig. 1.7. A periodic rectangular gate voltage $V_{\mathrm{exc}}(t)$ shifts the levels of the quantum dot up and down each cycle, allowing exactly one level to rise above the Fermi energy of the lead tunnel-coupled to the dot. While the level is above the Fermi energy, it becomes energetically favourable for it to tunnel into the lead. As the empty dot level is shifted below the Fermi energy again, an electron from the lead tunnels into the dot, "recharging" the pump and leaving a hole in the lead. To achieve higher pumping frequencies (required for a precise enough definition of the ampere) without losing the accuracy, it needs to be ensured that exactly one electron is emitted per cycle with a

very high probability. This means that the timescale of one pumping cycle is limited from below by the electron dwell time on the dot when the highest energy level is raised. For this reason, a charge pump is characterized by the resistance R and the capacitance C of its tunnel barrier, the product of which gives the dwell time $t_D = RC$. This means that, to obtain a higher pumping frequency, it is desirable to decrease the tunneling resistance. However, it cannot be decreased indefinitely—the regime $R \gg R_K$ (where $R_K = h/e^2$ is the resistance quantum) needs to be maintained to avoid quantum fluctuations spoiling the charge quantization on the dot. A typical tunnel capacitance in pumping devices is of the order of femtofarads, which gives roughly $RC \approx 0.1$ ns. Recently, experimental progress in single-electron emitters has made high-accuracy gigahertz charge pumping possible [Blum 07, Feve 07, Conn 13], and a revised definition of the ampere has been proposed for consideration at the 26th General Conference on Weights and Measures in 2018 [Mohr 16].

Single-electron emitters are also used as charge sources in electron quantum optics, a field that aims to recreate typical quantum optics experiments with electrons instead of photons. Electron quantum optics is also the context in which we look at electron scattering under step-like time-dependent potentials as well as other shapes of potential in Chapter 3. To illustrate the typical setup of an electron quantum optics experiment, we have shown an example of a Hong-Ou-Mandel experiment in Fig. 1.8. The classical photon analog was performed in 1987 and used particle indistinguishability to measure time intervals between two photon emissions [Hong 87]. In the electron variant of the Hong-Ou-Mandel experiment, the sample is based on a two-dimensional electron gas, typically created at the interface of gallium arsenide heterostructures. By applying a strong magnetic field perpendicular to the sample, the integer quantum Hall regime is reached. The chiral quantum Hall channels that appear at the edges of the sample provide ballistic waveguides for the electrons, which is a crucial requirement for being able to reproduce quantum optics experiments with electrons. The quantum Hall channels are indicated with blue lines in the figure, and the two-dimensional electron gas is constrained to the blue regions by applying gate voltages. Two independent charge sources (quantum dots) are tunnel-coupled to the quantum Hall channels. The emission from the sources is controlled by applying rectangular voltages $V_{\mathrm{exc1/exc2}}$ to the dots, and the tunneling from the dots to the channels is determined by the gate voltages $V_{\mathrm{g1/g2}}$. The emitted electrons travel from the source to the beam splitter in the middle of the sample. Whereas in photon quantum optics a half-silvered mirror or a polarizer is often used as a beam splitter, in electron quantum optics settings it is realized using a quantum point contact. The voltage V_{qpc} determines the transmission coefficient of the quantum point contact, and is set to 50% in the Hong-Ou-Mandel experiment. Electrons from the two different sources approach the quantum point contact from different directions and have an equal probability to be either reflected or transmitted, and continue to propagate to the detectors through channels 3 and 4. If the electrons are indistinguishable, Pauli exclusion principle dictates that they cannot exit the quantum point contact in the same output (known as anti-bunching). This is one of the main differences with photon quantum optics (others being the different nature of vacuum for photons and electrons, as well as the existence of interactions between electrons), where indistinguishability of bosons leads to two photons always exiting the beam splitter in the same output channel (bunching). If low frequency noise is measured

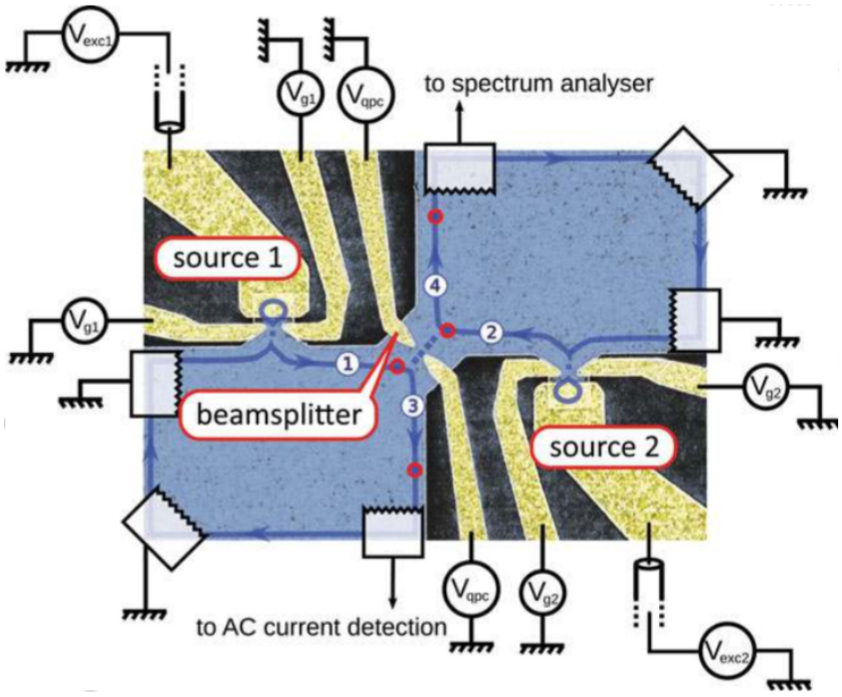

Figure 1.8.: A modified STM picture of an electronic Hong-Ou-Mandel experiment. The quantum Hall edges (drawn in dark blue) of a two-dimensional electron gas (blue) are used as waveguides for electrons emitted at sources 1 and 2 (controlled by $V_{\mathrm{exc1/exc2}}$ and coupled to the edge channels by $V_{\mathrm{g1/g2}}$) travelling to the beam splitter (a quantum point contact tuned by V_{qpc}) and then along edges 3 and 4. Low frequency noise is measured at the end of channel 4, and AC current is measured at the end of channel 3. Figure taken from [Bocq 14].

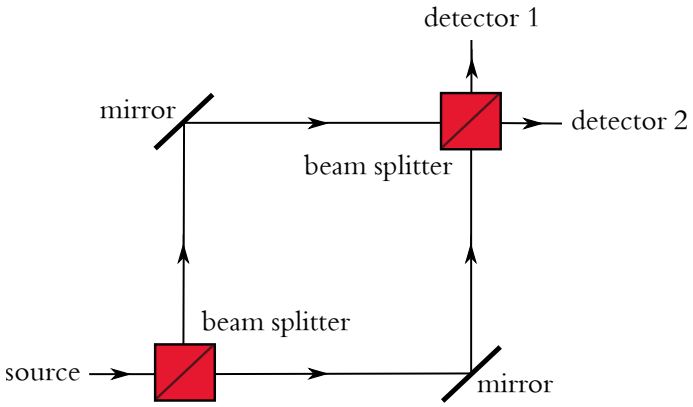

Figure 1.9.: A schematic of the setup of the Mach-Zehnder interferometer.

at one of the outputs (in this case at the end of channel 4) as a function of the delay time τ between the two sources, a so-called Pauli dip is observed around $\tau = 0$. The size of the dip gives information about the indistingishability of the two emitted wave packets. The other detector arm (at the end of channel 3) measures the alternating current created by the stream of electrons and holes (as shown before in Fig. 1.7, the single-particle pump emits holes as well as electrons). This can characterize the reliability of the pumping cycles (whether a significant part of the tunneling events are omitted) by how precisely the average current is quantized.

Using the same ingredients—single-particle pumps as electron sources, quantum Hall edges as ballistic waveguides, and quantum point contacts as beam splitters—other kinds of photon quantum optics experiments have also been reproduced with electrons, such as the Mach-Zehnder interferometer and the Hanbury-Brown and Twiss experiment. In the Mach-Zehnder experiment, single-particle interference is observed by splitting the source signal, letting the two different beams take different paths and then letting them interfere, as shown in Fig. 1.9. This setup is used to investigate quantum entanglement, and has many practical applications as well due to its capability of detecting very small changes in the length of one of the paths taken by the beam. In electron quantum optics, Mach-Zehnder interferometer is used to probe the wave-like properties of electrons, as well as to characterize the coherence of electron sources. The Hanbury-Brown and Twiss experiment, on the other hand, probes the particle nature of electrons and is used to characterize the statistical properties of electron sources. A sketch of the setup is shown in Fig. 1.10. In contrast to the Mach-Zehnder interferometer, here the two different beams are not joined after initially splitting them, but their intensities are measured separately at two different detectors. The correlations and anti-correlations between the intensities will depend on the bosonic or fermionic nature of the particles in the beam.

On the whole, electron quantum optics setups provide ways to investigate coherence and statistical properties of electron sources, single- and two-particle interference, electron wave packet propagation in ballistic waveguides, as well as electron state tomography. Motivated by a recent experiment, we explore a generic protocol for electron tomography

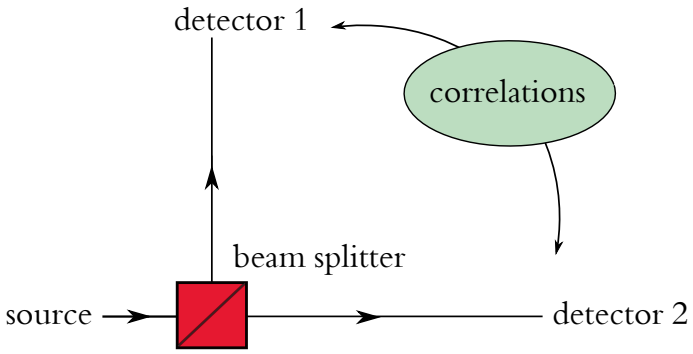

Figure 1.10.: A schematic of the setup of the Hanbury-Brown and Twiss intensity interferometer.

in Chapter 3.

1.3. Single-electron transistor

In the previous section, we discussed the application of a gated quantum dot as an electron pump. In Chapter 4, we look at another incarnation of the same physics—a single-electron transistor. In this particular case it is experimentally realized using a phtalocyanine molecule adsorbed on an InAs(111)A substrate, using the substrate and an STM tip as electrodes and indium adatoms for gating.

Single-electron transistors [Kast 92] are among the outcomes of the continued trend to decrease the size of electronic circuit elements. As observed by Moore [Moor 98], the density of transistors in integrated circuits has been increasing exponentially since the invention of integrated circuits in the 1960s. This miniaturization has increased the available computational power as well as decreased the production costs of electronic computation units. An obstacle in shrinking the circuit elements is power dissipation. Unwanted capacitances form between neighbouring elements of the circuit, dissipating energy $C_pV^2/2$ upon changing the voltage in a part of the circuit by V, where C_p is the parasitic capacitance. This means that large switching voltages for transistors result in considerable power losses. This is especially problematic for high operation frequencies, which is the case in information processing devices. A single-electron transistor contains a small number of elementary charges and is therefore more sensitive to changes in voltage. It would therefore require lower switching voltages and lead to lower enegy dissipation. This, in addition, to its small size (around 1 nm), makes the single-electron transistor a candidate for a next-generation transistor. Some of their potential applications also include memory cells as well as charge [Koro 92, Scho 98] and displacement [Knob 03] sensors.

1.3.1. Transport properties of single-electron transistors

Single-electron transistors are quantum dots tunnel-coupled to a source and a drain electrode that determine the bias voltage across the dot, as well as a gate electrode that shifts

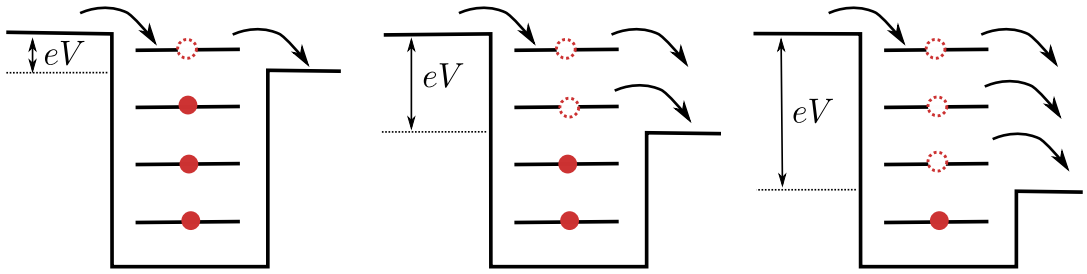

Figure 1.11.: A sketch of a quantum dot for different bias voltages, illustrating the origin of the steps in current-voltage diagrams of single-electron transistors. As the bias voltage V is increased, more energy levels start participating in transport. Due to the discreteness of the levels, the increase in current will resemble a staircase.

the potential of the dot. The name of the single-electron transistor comes from the fact that it transmits single electrons at a time. This is due to the spatial confinement of electrons, which leads to discrete energy levels and relatively small capacitances between the quantum dot and the electrodes. In general, the capacitance of a circle is proportional to its radius. Thus, by making the quantum dot smaller, its capacitance C can be made small and its electrostatic charging energy $E_C = q^2/2C$ large (q is the charge on the dot). If the charging energy is larger than the temperature and than the width of the energy levels in the dot, the addition of a single electron to the dot will be costly and charge quantization will become observable. This regime of a quantum dot is called the Coulomb blockade [Naza 09].

A manifestation of the Coulomb blockade is the observation of the step-like I-V or q-V curves known as the Coulomb staircase. This is done by keeping the gate voltage constant and varying the bias voltage applied to the dot. As the bias window is increased, more electrons will take part in the transport through the dot, as illustrated in Fig. 1.11. Because the energy levels of the quantum dot are discrete, the current flowing through the dot will only change after a new level enters the voltage bias window. The current will then change in a step-like manner, corresponding to the contribution of the new energy level. The first experimental observation of the Coulomb staircase was made by Lafarge *et al.* in 1991 [Lafa 91]. In the experiment, they created a micrometer-sized electron box coupled to the source and drain electrodes via two tunnel junctions using electron-beam lithography and shadow evaporation. Next to the electron box on the same chip, they patterned another single-electron transistor that was used as en electrometer to measure the charge residing in the electron box. The experimental data are shown in Fig. 1.12. As seen in the figure, for temperatures much lower than the charging energy of the dot (which corresponds to the Coulomb blockade regime), the number of elementary charges on the dot is a good quantum number and the steps of the staircase are very sharp. As the temperature is increased, the steps get washed out, and disappear completely as the temperature becomes much larger than the charging energy.

Another illustration of the transport properties of single-electron transistors is the ap-

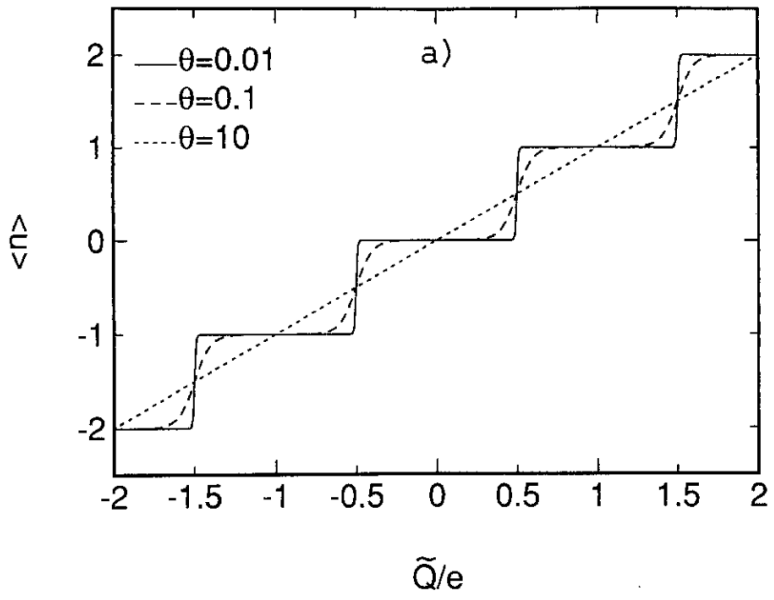

Figure 1.12.: Measurement data of the number of elementary charges $\langle n \rangle$ residing in an electron box as a function of the bias charge $\tilde{Q}$. The bias charge is related to the bias voltage V through $V = \tilde{Q}/\tilde{C}$, where $\tilde{C}$ is the capacitance between the box and the electrode through which the bias is applied. The different lines correspond to different values of the parameter θ that describes the ratio between the temparature and the charging energy, $\theta = k_B T C_\Sigma / e^2$. C_Σ is the total capacitance of the electron box. Figure taken from [Lafa 91].

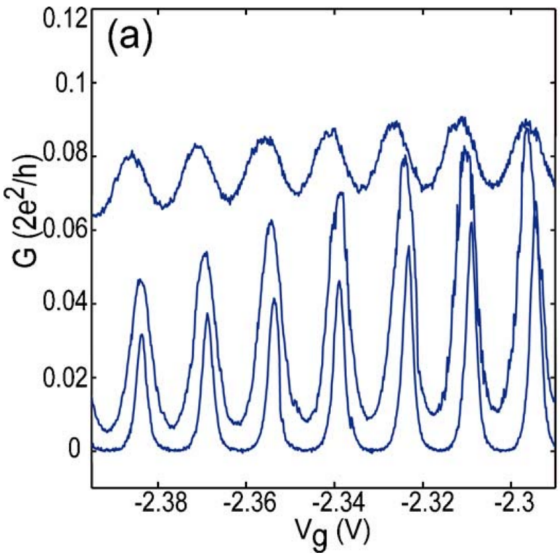

Figure 1.13.: Conductance oscillations of a quantum dot as a function of the gate voltage V_g. The different lines correspond to the temperatures $T = 0.314$, 1, and 3 K from bottom to top. The charging energy of the dot is 7.5 meV. Figure taken from [Chou 06].

pearance of conductance oscillations at very low temperatures, called the Coulomb oscillations [Been 91]. In contrast to the Coulomb staircase, here the bias voltage is kept fixed at zero, and instead the gate voltage V_g is varied. This means that transport through the dot will only be possible if one of the energy levels lies exactly at the chemical potential of the source and drain electrodes. Since varying the gate voltage has the effect of shifting the energy levels of the dot by eV_g, we expect sharp peaks in the conductance-gate voltage diagram that correspond to the resonances of the dot and are spaced by Δ/e, where Δ is the spacing between the energy levels of the dot. Coulomb oscillations have been observed experimentally many times, and one such example, realized in a GaN/AlGaN heterostructure, is given in Fig. 1.13. Similarly to the case of the Coulomb staircase, the oscillations become less pronounced as the temperature is increased.

When the same conductance measurement is repeated at non-zero bias voltages, the singular gate voltage values for which the conductance is finite extend into intervals of such values. Typically, the bias voltage is chosen smaller than Δ, such that only one level at a time can enter the bias window. If the bias voltage is chosen larger than the spacing, conductance increases accordingly. If the conductance is plotted in the V-V_g plane, the resulting diagram is known as the Coulomb diamonds. This will be explained in detail in Chapter 4. A recent experimental observation of the Coulomb diamonds is shown in Fig. 1.14.

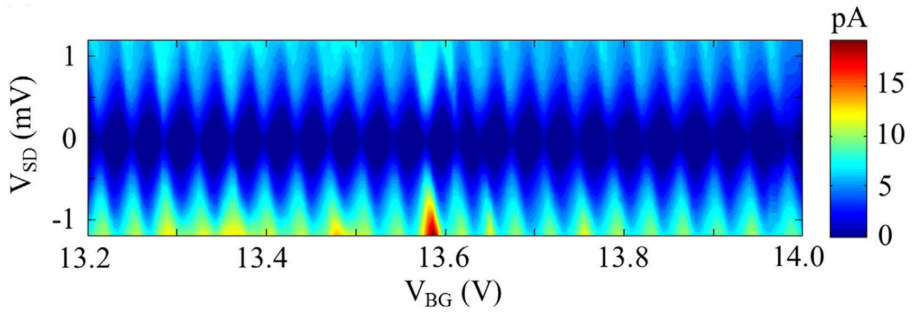

Figure 1.14.: Experimental data for the current flowing through a WS_2 quantum dot as a function of the gate voltage V_{BG} and the bias voltage V_{SD}. Figure taken from [Song 15].

1.3.2. Fabrication

All of the aforementioned transport properties of single-electron transistors in the Coulomb blockade regime have been observed in various setups. A common and one of the earliest realizations of single-electron transistors uses electron-beam lithography [Clel 13] to create the desired pattern on a resist, which is then placed on a semiconductor heterostructure. The metal chosen for the electrodes is then evaporated on top of the developed resist and lifted off together with the resist, leaving a metallic pattern on the surface of the heterostructure. In the interface between the semiconducting materials making up the heterostructure, a two-dimensional electron gas is formed. The layer between the gas and the electrodes needs to be thin enough so that the electric potential of the electrodes is felt by the electron gas. In this way, electrostatically-defined quantum dots are formed, which together with the source, drain, and gate electrodes constitute the single-electron transistor. A scanning tunneling microscope image of such a structure is shown in Fig. 1.15.

While the typical size of a quantum dot fabricated with top-down approaches such as lithography can be around tens of nanometers, approaches using self-assempbly can reach at least an order of magnitude smaller sizes, i.e., the size of an atom [Lu 07]. As mentioned before, a decrease in size leads to considerably larger charging energies and therefore higher temperatures at which the single-electron transistor can be operated. Even so, some devices fabricated with electron-beam lithography operating at room temperature have been reported [Guo 97, Pash 00]. However, this can be achieved more easily with other methods where the growth process of the quantum dot naturally leads to atomic-scale sizes.

One example of such a method is the use of nanocrystal particles as quantum dots [Klei 96, Klei 97]. Figure 1.16 shows a schematic and a scanning electron micrograph of such a system. The electrodes are still fabricated using electron-beam lithography, but the quantum dot is created by attaching self-assembled metallic colloids to the sample. This is done using a monolayer of organic linker molecules. If one of the colloidal nanocrystals attaches itself between the source and the drain electrodes, a single-electron transistor is

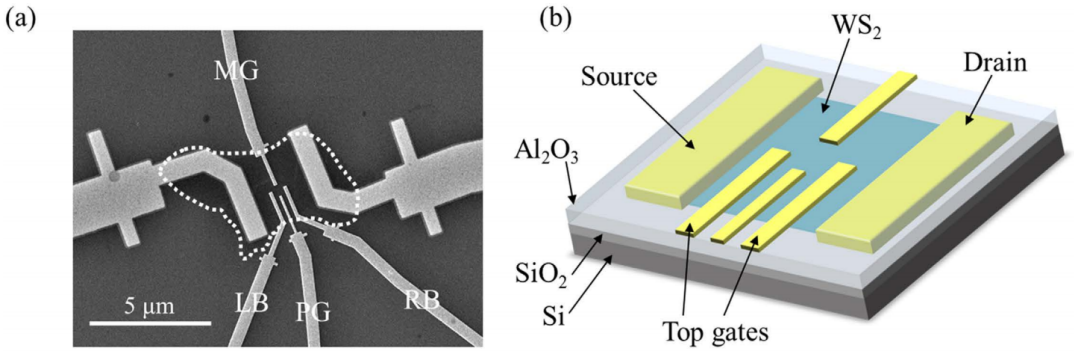

Figure 1.15.: Scanning electron microscope image of a single-electron transistor (left) and a schematic of the same device (right). The gates denoted by MG (middle gate), LB (left barrier), and RB (right barrier) create the electrostatic confinement creating the quantum dot. The plunger gate (PG) tunes the energy levels of the dot. Figure taken from [Song 15].

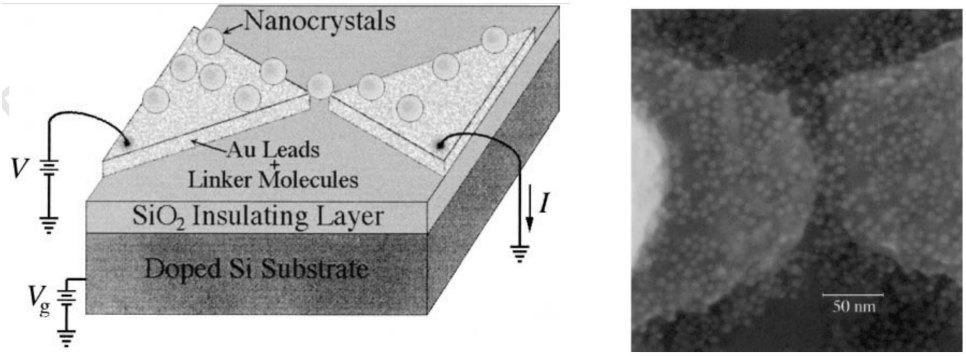

Figure 1.16.: Schematic (left) and a scanning electron micrograph (right) of a single-electron transistor formed by attaching CdSe nanocrystals to a sample with source and gate electrodes. In the micrograph, the smaller light dots are the nanocrystals. Due to the size of the gap between the electrodes, only one of the nanocrystals will be able to tunnel-couple to the electrodes and serve as a quantum dot. Figure taken from [Klei 97].

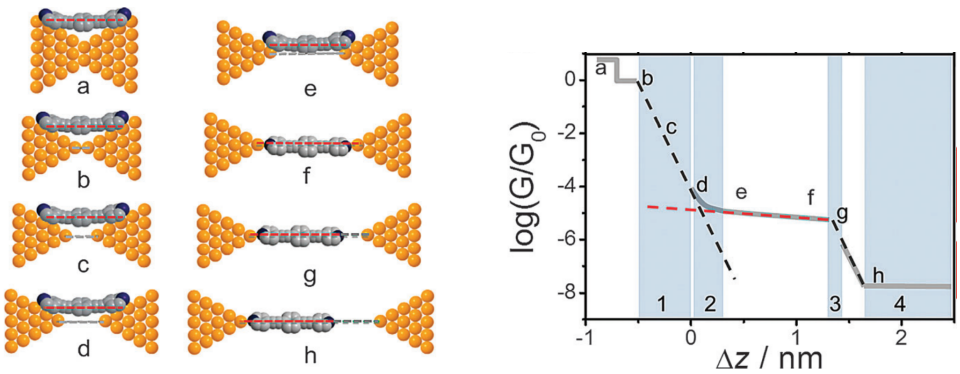

Figure 1.17.: Subsequent steps of establishing a molecular break junction (left) and a schematic representation of the conductance G of the junction as a function of the distance Δz between the electrodes (right). Conductance steps (grey solid line in the plot) are observed until the junction breaks at point b. From b to d the main contribution to conductance is still from tunneling between the electrodes (black dashed line). At point e the electrode-molecule-electrode junction forms and the transport is mainly through the molecule (red dashed line). If Δz is increased even further, the conductance quickly decreases. Figure taken from [Huan 15].

formed. The typical size of such nanocrystals is 5 nm. However, their position on the sample is random and therefore not ideal for a controlled fabrication and investigation of quantum dots. It has also been shown that such a setup can be destroyed by applying very large bias voltages.

A more controlled way to create quantum dots is to use break junctions [Ohni 98, Selz 06]. In this method, a single-atom-wide contact is established between two electrodes. For example, in scanning-tunneling-microscope break junctions this is done by first driving the STM tip into the substrate and then pulling it up again till the contact at its weakest point is only one atom wide. That only one atom remains between the electrodes is ensured by measuring the conductance of the junction as the electrodes are pulled farther away from each other. When the conductance reaches one conductance quantum $2e^2/h$, the contact is one atom wide. The tip and the substrate are submerged in a solution containing some (typically organic) molecules. If the electrodes are pulled even farther apart, the metallic contact breaks, and the molecules from the solution can enter the gap between the electrodes, forming a double tunnel-junction. This idea is illustrated in Fig. 1.17. Experimentally, the gating of such break junctions has proven to be challenging [Huan 15].

As graphene has gained a lot of attention since its discovery in 2004 [Novo 04], many graphene device applications have been proposed, single-electron transistors among them [Pono 08]. Conductance peaks were indeed observed in graphene devices larger than 100 nm, as shown in Fig. 1.18. Interestingly, when the devices were smaller than 100 nm, the conductance peaks were no longer equidistant, owing to the fact that, because of the

masless nature of the charge carriers, the single-particle level spacings in graphene quantum dots are considerably larger than for massive carriers. For even smaller device sizes, chaotic behavior is observed. In addition to graphene single-electron transistors, devices based on carbon nanotubes have also displayed Coulomb blockade physics [Bock 97, Tans 97, Yao 99, Post 01].

Another possible way to produce single-electron transistors is to use organic molecules (which can be viewed as naturally occurring quantum dots) adsorbed on a surface in a controlled manner and then biased with an STM tip. This will be the subject of Chapter 4, where we look at the realization of single-molecule transistor as a conformational switch.

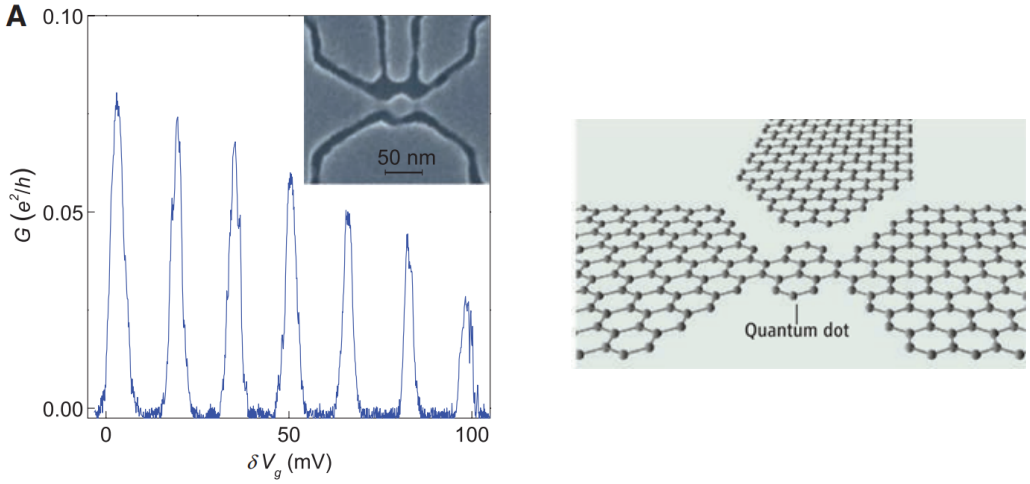

Figure 1.18.: Conductance measurements of a graphene single-electron transistor as a function of the gate voltage (left) and a schematic of the device (right). Figure taken from [Pono 08].

2. Current-induced switching of magnetic molecules on topological insulator surfaces

In this chapter, we show that electrical currents at the surface or edge of a topological insulator can be used to switch the orientation of a molecular magnet weakly coupled to the surface or edge of a topological insulator. For the edge of a two-dimensional topological insulator as well as for the surface of a three-dimensional topological insulator the application of a well-chosen surface/edge current can lead to a complete polarization of the molecule if the molecule's magnetic anisotropy axis is appropriately aligned with the current direction. For a generic orientation of the molecule a nonzero but incomplete polarization is obtained. We calculate the probability distribution of the magnetic states and the switching rates as a function of the applied current.

The chapter is organized as follows: We start with a short overview and motivation of the problem in Section 2.1. In Section 2.2 we consider a molecular magnet at the edge of a two-dimensional TI. We calculate the probability with which current-induced switching takes place, the current-induced switching rate, and the zero-current relaxation rate that arises from the exchange coupling of the molecule's spin to the TI edge. In Section 2.3 we consider the same questions for a molecular magnet on the surface of a three-dimensional topological insulator, which is the more likely candidate for an experimental realization. We conclude with a brief outlook in Section 2.4. The chapter mainly focuses on molecules with integer spin S. The case of a half-integer spin, which requires a technically more demanding analysis, is discussed in Appendix A.

2.1. Introduction

The central idea behind the field of spintronics is to use the electron's spin degree of freedom, not its charge, for information storage and processing [Zuti 04, Bade 10, Hoff 15]. Since the energy required to generate magnetic fields scales unfavorably at small length scales, electrical mechanisms for the manipulation and detection of magnetic moments are crucial for successful spintronics applications. The spin transfer torque [Slon 96, Berg 96] has been established as a reliable effect to manipulate the magnetization of a thin ferromagnetic layer with a spin-polarized current [Ralp 08]. Whereas injection from a ferromagnet was used as a spin-polarized current source in the original realization, devices based on spin-orbit coupling have also been realized [Ando 08, Pi 10, Liu 11, Miro 11, Liu 12, Kim 13, Fan 13, Gare 13, Emor 13, Ryu 13].

An extreme form of spin-orbit coupling exists in the surface states of topological insulators (TIs) [Fu 07, Hasa 10]: These states have complete spin-momentum locking, *i.e.*,

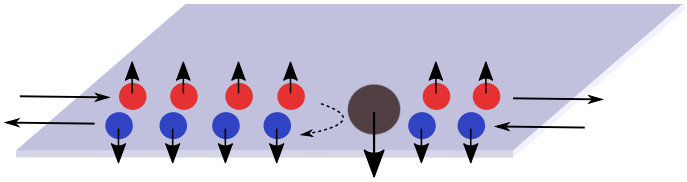

Figure 2.1.: Current-induced switching of a localized spin 1/2 weakly coupled to the helical edge of a two-dimensional topological insulator. Backscattering of a right-moving electron is accompanied by a flip to the spin "up" state of the localized spin, leaving it in a fully polarized state after a single backscattering event. For a sufficiently large applied current the reverse scattering process, which would return the localized spin to the "down" state, is strongly suppressed.

the electron spin and its direction of motion are perfectly correlated. One consequence of the spin-momentum locking is that a surface charge current in a TI is automatically spin-polarized. Recent proposals have concentrated on exploiting this effect to control the dynamics of thin magnetic layers in the proximity of the surface of a three-dimensional TI [Tser 12, Chen 14, Lind 14, Mahf 12, Mahf 16, Fisc 16, Ndia 17, Reza 16] or magnets coupled to the edge of a two-dimensional TI [Meng 14, Silv 16]. Experiments on metallic magnetic layers in contact to a TI have reported a spin-transfer torque exceeding the values found in non-topological spin-orbit materials [Fan 14, Mell 14, Wang 15].

In this chapter, we investigate the possibility to use the spin-polarized surface currents of a topological insulator to control the magnetic moment of a molecular magnet adsorbed on the surface of a three-dimensional topological insulator or at the edge of a two-dimensional topological insulator. Like a ferromagnet, a molecular magnet has degenerate magnetic ground states, separated by an energy barrier [Boga 08, Gatt 11], although in the case of a molecular magnet the barrier is microscopic, not macroscopic, which leads to a finite relaxation time of the molecule's magnetic moment. Of particular interest are the so-called "single-molecule magnets" [Frie 10], which consist of a magnetic core with a spin $S \sim 6 - 12$, shielded from the environment by a (typically) organic ligand. For single-molecule magnets magnetic lifetimes of several years have been reported for temperatures below the "blocking temperature" set by the anisotropy barrier between the two magnetic ground states [Chri 00]. Single-molecule magnets have been shown to preserve their magnetic properties, including long magnetic lifetimes, when adsorbed on conducting surfaces [Cand 11, Mann 09, Kahl 12, Mala 15, Marg 09]. The mechanism by which an applied electrical current at the surface of a TI can be used to switch the orientation of a molecular magnet is best illustrated using the example of a localized spin 1/2 coupled to the edge of a two-dimenstional topological insulator [Maci 09, Tana 11, Lund 12, Prob 15]. The electronic state at the edge of a two-dimensional TI is helical, so that electrons moving in opposite directions have opposite spin [Fu 07, Hasa 10]. Hence, a particle current to the right is polarized as "spin up", see Figure 2.1. By spin conservation, backscattering of a right-moving electron into a left-moving state requires the localized spin to flip from down to up, so that a single backscattering event is sufficient to polarize the spin 1/2 in the "up" state. If the applied current to the right is sufficiently large, the Pauli principle forbids

backscattering of left-moving electrons—which would be accompanied by a spin flip in the opposite direction—, so that the spin 1/2 remains in the "up" state as long as the current is being applied. This simple picture needs to be refined for molecules with a higher spin and for molecular magnets adsorbed to the two-dimensional surface of a three-dimensional TI. Unlike the spin 1/2 of the example of Figure 2.1, a higher-spin molecule comes with its own anisotropy axis, and the argument based on spin conservation no longer applies in this simple form if the molecule's anisotropy axis is not aligned with the spin quantization axis of the TI edge state. (Spin conservation is also violated if the exchange coupling between the magnetic molecule and the helical edge is not isotropic. This scenario already applies to spin 1/2, see Refs. [Vayr 14, Vayr 16, Kimm 16].) Simple spin conservation arguments cannot be applied to a molecular magnet on the surface of a three-dimensional topological insulator either, because in that case there is no unique spin quantization axis, as electrons can propagate in an arbitrary direction along the surface. As we will show below, in this generic situation current-induced switching of molecular magnet on a TI surface is not perfect, although appreciable polarizations can be achieved even for randomly oriented molecules. An interesting observation is that, unlike in the example above, for a molecular magnet on the surface of a three-dimensional TI the current-induced polarization is not a monotonously increasing function of the applied current, but has a maximum at intermediate current densities.

2.2. Molecular magnet at edge of a two-dimensional TI

2.2.1. Spin 1/2

To introduce our notation and to provide a reference for further calculations, we start by considering a localized moment of spin $S = 1/2$ exchange-coupled to the helical edge of a two-dimensional topological insulator. We assume that there is only a single localized spin coupled to the edge and that the temperature is large enough that the Kondo effect can be neglected. In that case transitions between different spin states can be described using rate equations.

The coupling between the edge and the magnetic moment is described by the exchange Hamiltonian

$$H_{\text{ex}} = vJ\delta(z)\mathbf{S}\cdot\boldsymbol{\sigma}, \tag{2.1}$$

where z labels the coordinate along the helical edge, v is the velocity of the helical edge state, and J is the dimensionless exchange coupling. Since the dominant source of anisotropy for molecular magnets is the molecule's intrinsic anisotropy energy (see next subsection), for simplicity we have taken the exchange interaction (2.1) to be isotropic. (Note, however, that for the case $S = 1/2$ intrinsic anisotropy is not possible, so that the exchange interaction is the only source of anisotropy, see, *e.g.*, Refs. [Vayr 14, Vayr 16, Kimm 16].) Because of spin-momentum locking of the edge states, backscattering of edge electrons from the molecular magnet involves simultaneous flips of the spin of the edge electrons and of the localized spin of the molecular magnet. We fix the spin z axis along the direction of the spin quantization axis for the edge-state electrons,

$$H_{\text{edge}} = vp_z\sigma_z, \tag{2.2}$$

so that right-moving electrons at the edge have spin up and left-moving electrons have spin down. We note that the spin z axis need not be in the same direction as the laboratory z axis. (In fact, for the edge of a two-dimensional topological insulator, the spin quantization axis is commonly taken to be perpendicular to the plane of the TI [Brun 12].) The states $|k\pm\rangle$ in the helical edge are labeled by their energy $\varepsilon = \hbar v k$ and the propagation direction $\tau = \pm$, where we take $\tau = +$ for right-moving electrons (positive z direction) and $\tau = -$ for left-moving electrons. (Note that in this notation k merely parameterizes the energy; its magnitude $|\hbar k|$ equals the magnitude of the momentum, but the sign of k is that of the energy ε, not of the momentum.)

The transition rates $\Gamma_{s,s'}$ between the spin states are calculated from Fermi's golden rule. The rate $\Gamma_{\downarrow,\uparrow}$ for transitions from the spin up state $|\uparrow\rangle$ to the spin down state $|\downarrow\rangle$ is

$$\begin{aligned}\Gamma_{\downarrow,\uparrow} &= \frac{2\pi}{\hbar}\int_{-\infty}^{+\infty}\frac{dkdk'}{(2\pi)^2}n_-(\varepsilon_k)[1-n_+(\varepsilon_{k'})] \\ &\quad\times|\langle+,\downarrow|H_{\rm ex}|-,\uparrow\rangle|^2\delta(\varepsilon_k-\varepsilon_{k'}) \\ &= \frac{J^2}{2\pi\hbar}\int_{-\infty}^{+\infty}d\varepsilon n_-(\varepsilon)(1-n_+(\varepsilon)).\end{aligned} \tag{2.3}$$

(The matrix elements of $H_{\rm ex}$ do not depend on k and k', which is why we have suppressed k, k' in our notation.) Similarly, the rate $\Gamma_{\uparrow,\downarrow}$ at which transitions from the spin down state to the spin up state take place reads

$$\Gamma_{\uparrow,\downarrow} = \frac{J^2}{2\pi\hbar}\int_{-\infty}^{+\infty}d\varepsilon n_+(\varepsilon)(1-n_-(\varepsilon)). \tag{2.4}$$

The distribution function at temperature T and chemical potential μ in the presence of an edge current $\mathcal{I} = Ie$ is

$$n_\tau(\varepsilon) = \frac{1}{1+e^{(\varepsilon-\mu-\tau\pi\hbar I)/k_{\rm B}T}}, \tag{2.5}$$

as one can easily verify from the relation $I = (1/2\pi\hbar)\int d\varepsilon[n_+(\varepsilon)-n_-(\varepsilon)]$. For definiteness, we will assume throughout that the particle current is to the right, $I > 0$. Performing the integrations in Eqs. (2.3) and (2.4) then gives

$$\Gamma_{\downarrow,\uparrow} = J^2 g(I), \qquad \Gamma_{\uparrow,\downarrow} = J^2 g(-I), \tag{2.6}$$

where we abbreviated

$$g(I) = \frac{I}{e^{2\pi\hbar I/k_{\rm B}T}-1}. \tag{2.7}$$

For high applied currents, $\hbar I \gg k_{\rm B}T$, scattering processes in which a left-moving electron is scattered into a right-moving one and, correspondingly, the rate $\Gamma_{\downarrow,\uparrow}$, are exponentially suppressed. On the other hand, for low applied currents $|I| \ll k_{\rm B}T/\hbar$, scattering of thermally excited charge carriers dominates the spin switching rates, and the application of the current I only gives a slight asymmetry.

In the absence of coherences between the spin states $|1/2\rangle$ and $|-1/2\rangle$ the probabilities $P_\uparrow$ and $P_\downarrow$ to find the spin in a state of $s = \uparrow, \downarrow$ can be solved from the stationary solutions of the rate equation

$$\frac{dP_s}{dt} = \sum_{s' \neq s} (\Gamma_{s,s'} P_{s'} - \Gamma_{s',s} P_s). \tag{2.8}$$

(In principle, one needs a density matrix to describe possible coherent superpositions of the degenerate states $|1/2\rangle$ and $|-1/2\rangle$, see, *e.g.*, Refs. [Naza 93, Gurv 98, Koni 03, Brau 04, Brai 05, Prob 15] and Appendix A. However, such coherences do not occur in the present case, in which there is no external magnetic field and a single spin quantization axis for the conduction electrons at the TI edge and the localized spin.) Substituting the rates (2.6) one immediately finds (see also Refs. [Lund 12, Vayr 14, Vayr 16])

$$P_\uparrow = 1 - P_\downarrow = \frac{1}{1 + e^{-2\pi\hbar I / k_\mathrm{B} T}}. \tag{2.9}$$

The same result also follows from the observation that the coupling to the conduction electrons at the TI edge effectively amounts to a Zeeman shift $2\pi\hbar I$ between the spin up and spin down states of the molecule. We conclude that the application of a current $I \gg k_\mathrm{B} T/\hbar$ leads to a complete polarization of the molecule's spin.

2.2.2. Higher-spin molecules

Although the application of a current through the helical edge of a two-dimensional topological insulator causes a polarization of a spin 1/2 exchange-coupled to the edge state, the induced magnetic moment quickly disappears as soon as the current is switched off. In our model, in which the coupling to the helical edge state is the only source of relaxation, the corresponding relaxation rate Γ is given by the low-current limit of Eq. (2.6),

$$\Gamma_{\uparrow,\downarrow} = \Gamma_{\downarrow,\uparrow} = \frac{J^2 k_\mathrm{B} T}{2\pi\hbar}. \tag{2.10}$$

Longer relaxation times in the absence of an applied current requires molecules with a higher spin S. In this case, magnetic anisotropy,

$$H_\mathrm{anis} = -\frac{2\pi}{\hbar} D(\mathbf{S} \cdot \mathbf{e})^2, \tag{2.11}$$

imposes an energy barrier between states with maximal and minimal spin $\pm\hbar S$ (measured along the anisotropy axis $\mathbf{e}$), see Figure 2.2, which, if $k_\mathrm{B} T$ is lower than the barrier energy, leads to strongly enhanced lifetimes. (See below for a quantitative estimate for our model.) In our analysis, we have adopted a simple easy-axis anisotropy strength D (which we take to have the units of frequency) with $D > 0$, although our considerations also carry over to other forms for the anisotropy energy in which there are two different minima. (The case $D < 0$ is for easy-plane anisotropy, which does not have two separated energy minima and will not be considered here.) We label the spin states with the quantum number $s = -S$, $-S+1, \ldots, S$ for the spin component $\hbar s$ along the $\mathbf{e}$-direction. (For $S = 1/2$, s takes the values $s = \pm 1/2$, corresponding to the notation "$\uparrow$" and "$\downarrow$" in the previous subsection.)

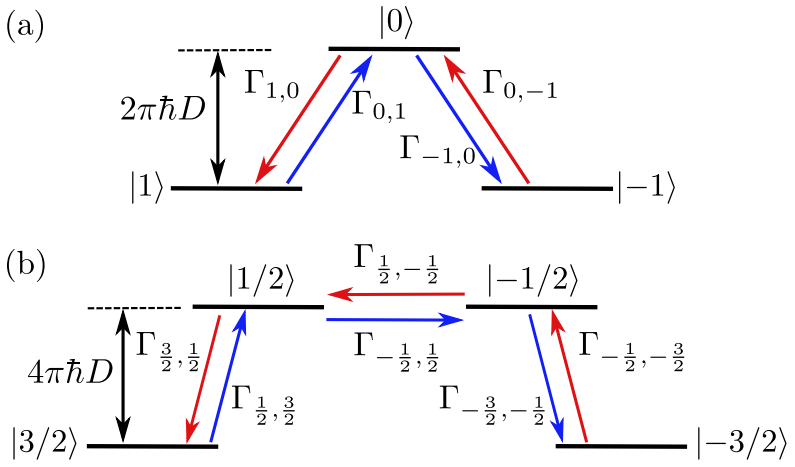

Figure 2.2.: Schematic drawing of energy levels and transition rates $\Gamma_{s\pm1,s}$ (a) for a spin-1 molecule and (b) for a spin-3/2 molecule.

If the anisotropy axis is aligned with the spin quantization axis for the helical edge state, the analysis of the previous subsection immediately carries over, and one finds

$$\Gamma_{s\pm1,s} = J^2(S \mp s)(S \pm s + 1)g[\mp(I + D(2s \pm 1)]. \tag{2.12}$$

For the probabilities P_s one then finds

$$P_s = \frac{1}{Z} e^{(2\pi s\hbar I + 2\pi\hbar D s^2)/k_\mathrm{B}T}, \tag{2.13}$$

where the prefactor is fixed by the normalization condition $\sum_s P_s = 1$.

If the temperature is much smaller than the anisotropy energy, which is a condition that we will assume throughout this chapter, the rate equations can be solved directly, using detailed balance, to give the zero-current switching rate $\Gamma_\mathrm{switch}(0)$ between the two magnetic ground states $|S\rangle$ and $|-S\rangle$,

$$\Gamma_\mathrm{switch}(0) \approx \frac{1}{2} J^2 S(S+1) D e^{-2\pi\hbar D S^2/k_\mathrm{B}T} \tag{2.14}$$

if S is integer and

$$\Gamma_\mathrm{switch}(0) \approx J^2(S+1/2)^2 \frac{k_\mathrm{B}T}{2\pi\hbar} e^{-2\pi\hbar D(S^2-1/4)/k_\mathrm{B}T} \tag{2.15}$$

if S is half integer.

The application of a current I slightly larger than $D(2S-1)$ leads to a quick and complete spin polarization of the molecule. The switching rate $\Gamma_\mathrm{switch}(I)$ can be estimated as the inverse of the sum of inverse transition rates $\Gamma_{s,s+1}$, which gives

$$\Gamma_\mathrm{switch}(I) \sim J^2 I(S+1/2)/\ln(4S+1) \tag{2.16}$$

for large S. A smaller current $k_{\mathrm{B}}T \ll \hbar I \ll \hbar D(2S+1)$ also polarizes the molecule, but since thermal activation is still needed in the switching process, the time required to reach the polarized state is still large (though much shorter than the zero-current lifetime),

$$\Gamma_{\mathrm{switch}}(I) \approx \Gamma_{\mathrm{switch}}(0) e^{2\pi\hbar I S/k_{\mathrm{B}}T} \tag{2.17}$$

if S is integer and

$$\Gamma_{\mathrm{switch}}(I) \approx \Gamma_{\mathrm{switch}}(0) e^{2\pi\hbar I (S-1/2)/k_{\mathrm{B}}T} \tag{2.18}$$

if S is half integer.

If $\mathbf{e}$ is not aligned with the z axis, the expression for the rates $\Gamma_{s\pm1,s}$ involves the matrix elements

$$\begin{aligned}
\langle \tau', s-1|H_{\mathrm{ex}}|\tau, s\rangle &= \frac{Jv\hbar}{2}\sqrt{(S+s)(S-s+1)} \\
&\quad \times \begin{cases} -\tau \sin\theta & \text{if } \tau' = \tau, \\ \tau'(1+\tau'\cos\theta)e^{-i\phi\tau'} & \text{if } \tau' = -\tau, \end{cases} \\
\langle \tau', s+1|H_{\mathrm{ex}}|\tau, s\rangle &= \frac{Jv\hbar}{2}\sqrt{(S-s)(S+s+1)} \\
&\quad \times \begin{cases} -\tau \sin\theta & \text{if } \tau' = \tau, \\ \tau(1+\tau\cos\theta)e^{i\phi\tau} & \text{if } \tau' = -\tau, \end{cases}
\end{aligned} \tag{2.19}$$

where θ and ϕ are the polar angles corresponding to the anisotropy axis $\mathbf{e} = \cos\theta\mathbf{e}_z + \sin\theta\cos\phi\mathbf{e}_x + \sin\theta\sin\phi\mathbf{e}_y$. This gives

$$\begin{aligned}
\Gamma_{s\pm1,s} = &\frac{1}{4}J^2(S\mp s)(S\pm s+1) \\
&\times \sum_{\tau} \Big\{ g[\mp D(2s\pm1)]\sin^2\theta + (1\mp\tau\cos\theta)^2 g[\tau I \mp D(2s\pm1)] \Big\}.
\end{aligned} \tag{2.20}$$

One verifies that the zero-current rates are the same as those of Eqs. (2.12), independent of the direction $\mathbf{e}$ of the anisotropy axis, so that Eqs. (2.14) and (2.15) still apply.

Because of the degeneracy of the states $|1/2\rangle$ and $|-1/2\rangle$ the rate equation (2.8) is not sufficient to describe transitions between these two states and, instead, one has to use a master equation for the reduced 2×2 density matrix that is able to account for coherent superpositions of the states $|1/2\rangle$ and $|-1/2\rangle$. For that reason we here restrict ourselves to the case of integer S, for which this complication does not occur. A complete analysis and final expressions for half-integer S are given in Appendix A.

We first discuss the case of an "intermediate" current $k_{\mathrm{B}}T \ll \hbar I \ll \hbar D(2S-1)$, for

which the transition rates (2.20) can be approximated as

$$\begin{aligned}\Gamma_{s+1,s} &\approx \frac{J^2 D}{4}(S-s)(S+s+1)|2s+1| \\ &\times \begin{cases} 4 & \text{if } s \geq 0, \\ (1+\cos\theta)^2 e^{2\pi\hbar(I-D|2s+1|)/k_{\mathrm{B}}T} & \text{if } s < 0, \end{cases} \\ \Gamma_{s-1,s} &\approx \frac{J^2 D}{4}(S+s)(S-s+1)|2s-1| \\ &\times \begin{cases} (1-\cos\theta)^2 e^{2\pi\hbar(I-D|2s-1|)/k_{\mathrm{B}}T} & \text{if } s > 0, \\ 4 & \text{if } s \leq 0. \end{cases} \end{aligned} \tag{2.21}$$

The large difference between "upstream" transitions to higher-energy spin states and "downstream" transitions to lower-energy spin states ensures that the molecule will predominantly be in one of its two magnetic ground states $|S\rangle$ and $|-S\rangle$. The presence of the applied current breaks the symmetry between these two ground states and leads to a preferred population of the state $|S\rangle$ if $\theta < \pi/2$ and $|-S\rangle$ if $\theta > \pi/2$, although there is no longer a perfect polarization for generic θ,

$$\begin{aligned} P_S &= 1 - P_{-S} \\ &= \frac{(1+\cos\theta)^{2S}}{(1+\cos\theta)^{2S} + (1-\cos\theta)^{2S}}. \end{aligned} \tag{2.22}$$

Switching between the magnetic ground states involves thermal activation, which is why the switching rate between the magnetic ground states is exponentially long in $2\pi\hbar DS^2/k_{\mathrm{B}}T$, although the rate is parametricaly larger than the spontaneous relaxation rate at zero current. Defining $\Gamma_{\mathrm{switch}}(I)$ as the switching rate from $|-S\rangle$ to $|S\rangle$ we have

$$\Gamma_{\mathrm{switch}}(I) = \Gamma_{\mathrm{switch}}(0)\left(\frac{1+\cos\theta}{2}\right)^{2S} e^{2\pi\hbar IS/k_{\mathrm{B}}T}, \tag{2.23}$$

where $\Gamma_{\mathrm{switch}}(0)$ is the zero-current relaxation rate of Eq. (2.14). The switching rate for the inverse process is obtained upon replacing $\theta \to \pi - \theta$. The difference between the case $\theta = 0$ and generic θ is most pronounced in the "high-current" limit $I \gg D(2S-1)$, in which the rates $\Gamma_{s\pm1,s}$ in Eq. (2.20) are dominated by the terms proportional to $g[-I \mp D(2s\pm1)]$. Approximating $g[-I \pm D(2s \mp 1)] \approx I$ for $I \gg D(2S-1)$, we find

$$\Gamma_{s\pm1,s} = \frac{I}{4}J^2(S \mp s)(S \pm s + 1)(1 \pm \cos\theta)^2. \tag{2.24}$$

For the probabilities P_s this gives immediately

$$P_s = \frac{4\cos\theta(1-\cos\theta)^{2(S-s)}(1+\cos\theta)^{2(S+s)}}{(1+\cos\theta)^{2(2S+1)} - (1-\cos\theta)^{2(2S+1)}}. \tag{2.25}$$

For θ close to zero this still gives a narrow distribution around $s = S$, but perfect polarization is not reached if $\theta \neq 0$ independent of the magnitude of the current I. Examples

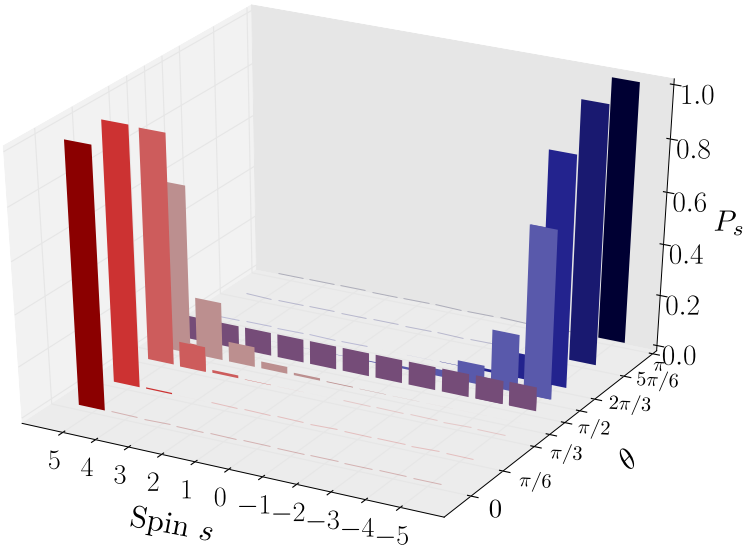

Figure 2.3.: Steady-state probability distribution (2.25) for $S = 5$ and for angles $\theta = 0$, $\theta = \pi/6$, $\theta = \pi/3$, $\theta = 5\pi/12$, $\theta = \pi/2$, $\theta = 7\pi/12$, $\theta = 2\pi/3$, $\theta = 5\pi/6$ and $\theta = \pi$.

of the distribution (2.25) are shown in Figure 2.3 for $S = 5$ and for several representative angles θ.

Figure 2.4 shows the mean values $\langle \mathbf{S} \cdot \mathbf{e} \rangle$ of the spin component along the anisotropy axis and $\langle S_z \rangle = \langle \mathbf{S} \cdot \mathbf{e} \rangle (\mathbf{e} \cdot \mathbf{e}_z)$ of the spin component along the current direction as a function of the angle θ for two different values of the total spin S. Except for $\theta = \pi/2$, the application of a current always results in a net spin in the current direction. For a randomly oriented molecule, the average moment in the current direction approaches $S/2$ in the limit of large S. Without a perfect current-induced polarization, we should define the current-induced "switching rate" $\Gamma_{\text{switch}}(I)$ as the rate at which the steady-state probability P_s is approached, starting from $|-S\rangle$ (if $\theta < \pi/2$). The estimate (2.16) for the switching rate $\Gamma_{\text{switch}}(I)$ obtained above for $\mathbf{e}$ parallel to the z axis remains valid as a good order-of-magnitude estimate for the case of a general orientation of the anisotropy axis in the high-current regime.

2.3. Three-dimensional topological insulator

The main result of the previous section is that the current-induced polarization of a molecular magnet coupled to the edge of a two-dimensional TI is complete only if the molecule's anisotropy axis is aligned with the spin quantization axis for the TI edge state, whereas the polarization is incomplete—but generally nonzero—for arbitrary orientations of the molecule. The analysis was simplified by the fact that the edge of a two-dimensional TI has a unique propagation direction and, hence, a unique spin quantization axis. This is the

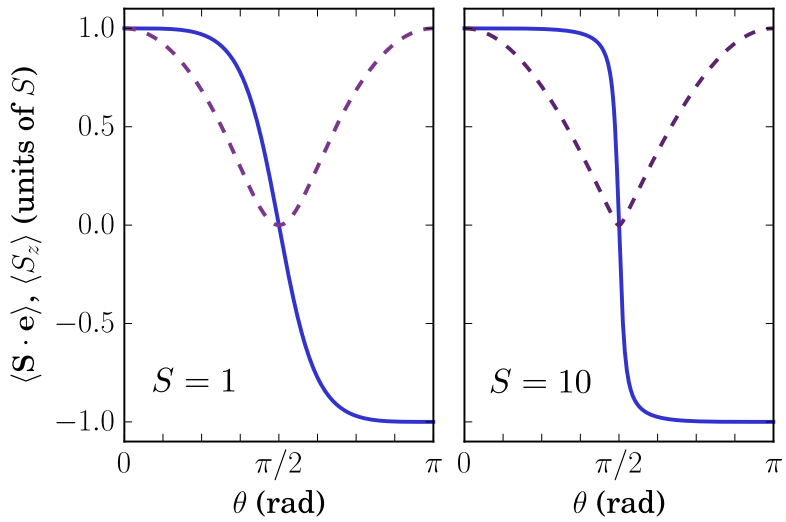

Figure 2.4.: Mean spin component $\langle \mathbf{S}\cdot\mathbf{e}\rangle$ along the direction of the anisotropy axis (solid curves) and the mean spin component $\langle S_z\rangle$ in the current direction (dashed), as a function of the angle θ, for $S = 1$ (left panel) and $S = 10$ (right panel).

main difference with the case of a molecule coupled to the surface of a three-dimensional TI: Electrons at the surface of a three-dimensional TI can propagate in all directions in the plane of the surface, even in the presence of a large applied current. Hence, there is not a unique spin quantization axis, and there will always be surface-state electrons with a spin that is not aligned with the anisotropy axis of the molecular magnet. Nevertheless, as we show below, even for a molecule adsorbed on the surface of a three-dimensional TI the application of an electrical current can lead to a complete spin polarization, provided the molecule's anisotropy axis is aligned with the current direction and the magnitude of the applied current is appropriately chosen. As in the case of a two-dimensional TI, the spin polarization of the molecular magnet is not complete (but generally nonzero) if the molecule's magnetic anisotropy axis is not aligned with the current direction. To keep the notation close to that of the previous section, we take the TI surface to be the xz plane and take the direction of (particle) current flow to be the positive z direction, see Figure 2.5. The electrons at the TI surface are then described by the Hamiltonian

$$H_{\text{surface}} = v(p_x\sigma_x + p_z\sigma_z). \tag{2.26}$$

We write the current density $\mathbf{j}$ as

$$\mathbf{j} = \frac{1}{4}k_{\text{F}}I\mathbf{e}_z, \tag{2.27}$$

where k_{F} is the Fermi wavenumber and I has the dimension of current. For the exchange Hamiltonian we take

$$H_{\text{ex}} = \frac{2v}{k_{\text{F}}}J\delta(x)\delta(z)\mathbf{S}\cdot\boldsymbol{\sigma}, \tag{2.28}$$

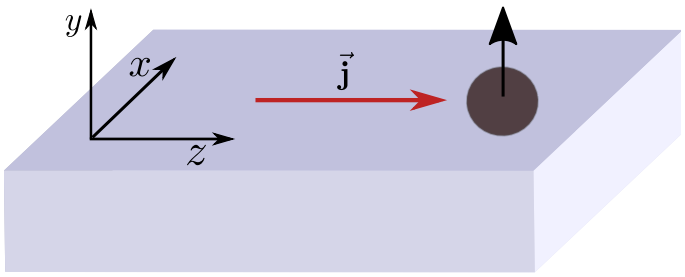

Figure 2.5.: Molecular magnet on the surface of a three-dimensional topological insulator. The TI surface is the xz plane. A current is applied in the positive z direction.

where, as in the previous section, a prefactor has been included to make the strength J of the exchange interaction dimensionless. The Hamiltonian $H_{\rm anis}$ for the magnetic anisotropy of the magnetic molecule is the same as in the previous subsection, see Eq. (2.11). The eigenstates of $H_{\rm surface}$ are labeled by the energy $\varepsilon = \hbar v k$ and by the angle φ of the propagation direction in the xz plane, such that $\varphi = 0$ corresponds to the positive z direction. We assume that the chemical potential $\mu = \hbar k_{\rm F} v \gg \max(k_{\rm B}T, \hbar I)$, which ensures that thermally excited carriers as well as carriers contributing to the current flow remain well away from the Dirac point. In that case the distribution function in the presence of a particle current density $1/4k_{\rm F} I \mathbf{e}_z$ is

$$n(\varepsilon,\varphi) = \frac{1}{1+e^{(\varepsilon-\mu-\pi\hbar I\cos\varphi)/k_{\rm B}T}}. \tag{2.29}$$

Equation (2.29) both follows from a solution of the Boltzmann equation and maximizes the entropy under the constraint of a fixed current density $\mathbf{j} = k_{\rm F} I \mathbf{e}_z/4$.

For the calculation of the transition rates between different spin states we need the matrix elements

$$\begin{aligned}\langle\varphi', s\pm1|H_{\rm ex}|\varphi, s\rangle &= \frac{Jv\hbar}{k_{\rm F}}\sqrt{(S\mp s)(S\pm s+1)}\Big[(\cos\theta\cos\phi \pm i\sin\phi)\sin\varphi_+ \\ &\pm (\cos\phi \pm i\cos\theta\sin\phi)\sin\varphi_- - \sin\theta\cos\varphi_+\Big],\end{aligned} \tag{2.30}$$

where we abbreviated $\varphi_\pm = (\varphi' \pm \varphi)/2$. Equation (2.30) generalizes Eq. (2.19) to the case of a surface state. As in Eq. (2.19), θ and ϕ are the polar angles marking the direction of the anisotropy axis. For the transition rates we then find, again assuming $\mu \gg \max(k_{\rm B}T, \hbar I)$,

$$\begin{aligned}\Gamma_{s\pm1,s} &= J^2(S\mp s)(S\pm s+1)\int\frac{d\varphi'}{2\pi}\frac{d\varphi}{2\pi}(1\pm\cos\theta\cos\varphi+\sin\theta\cos\phi\sin\varphi) \\ &\times (1\mp\cos\theta\cos\varphi'+\sin\theta\cos\phi\sin\varphi') \\ &\times g[I(\cos\varphi'-\cos\varphi)/2 \mp D(2s\pm1)],\end{aligned} \tag{2.31}$$

where the function $g(I)$ was introduced in Eq. (2.7). We will now analyze these rates and the resulting probabilities P_s in the regimes of low current densities, $\hbar|I| \ll k_{\rm B}T$, intermediate current densities, $k_{\rm B}T \ll \hbar I \ll \hbar D(2S-1)$, and high current densities,

$\hbar I \gg \hbar D(2S-1)$. (For $S = 1/2$ no intermediate regime exists and the high-current regime is defined as $\hbar I \gg k_\mathrm{B}T$.)

For low current densities $\hbar|I| \ll k_\mathrm{B}T$ the expressions (2.31) for the transition rates simplify to

$$\begin{aligned}\Gamma_{s+1,s} &\approx \Gamma_{-s-1,-s} \approx J^2(S-s)(S+s+1) \\ &\times \begin{cases} D|2s+1| & \text{if } s > -1/2, \\ k_\mathrm{B}T/2\pi\hbar & \text{if } s = -1/2, \\ D|2s+1|e^{-2\pi\hbar D|2s+1|/k_\mathrm{B}T} & \text{if } s < -1/2. \end{cases}\end{aligned} \tag{2.32}$$

The resulting zero-current switching rate $\Gamma_\mathrm{switch}(0)$ is given by the same expression as in the two-dimensional case, see Eqs. (2.14) and (2.15).

For intermediate current densities, $k_\mathrm{B}T \ll \hbar I \ll \hbar D(2S-1)$, the exponential suppression of the transition rates to higher-energy spin states is reduced, whereas the transition rates into the lower-energy states remains approximately as in the low-current regime. For a quantitive analysis we restrict ourselves to the case of integer spin S, referring to the Appendix for a discussion of half-integer S. In the intermediate-current regime the transition rates can be approximated as

$$\begin{aligned}\Gamma_{s+1,s} &\approx J^2(S-s)(S+s+1) \\ &\times \begin{cases} D|2s+1| & \text{if } s \geq 0, \\ \frac{k_\mathrm{B}T}{2\pi^2\hbar I}(1+\cos\theta)^2 D|2s+1|e^{2\pi\hbar(I-D|2s+1|)/k_\mathrm{B}T} & \text{if } s < 0, \end{cases} \\ \Gamma_{s-1,s} &\approx J^2(S+s)(S-s+1) \\ &\times \begin{cases} \frac{k_\mathrm{B}T}{2\pi^2\hbar I}(1-\cos\theta)^2 D|2s-1|e^{2\pi\hbar(I-D|2s-1|)/k_\mathrm{B}T} & \text{if } s > 0, \\ D|2s-1| & \text{if } s \leq 0. \end{cases}\end{aligned} \tag{2.33}$$

As in the two-dimensional case, the applied current breaks the symmetry between states with positive and negative spin s, leading to an imbalance between the populations of the ground states $|S\rangle$ and $|-S\rangle$,

$$\begin{aligned}P_S &= 1 - P_{-S} \\ &= \frac{(1+\cos\theta)^{2S}}{(1+\cos\theta)^{2S} + (1-\cos\theta)^{2S}}.\end{aligned} \tag{2.34}$$

The population of the excited states $|s| < S$ remains exponentially small in $\hbar D(2S-1)/k_\mathrm{B}T$. The current-induced switching rate from the state $|-S\rangle$ into $|S\rangle$ is

$$\begin{aligned}\Gamma_\mathrm{switch}(I) &= \Gamma_\mathrm{switch}(0)\left[\frac{k_\mathrm{B}T(1+\cos\theta)^2}{2\pi^2\hbar I}\right]^S \\ &\times e^{2\pi\hbar SI/k_\mathrm{B}T}.\end{aligned} \tag{2.35}$$

The inverse rate is given by the same expression, but with $\cos\theta$ replaced by $-\cos\theta$.

The case $\theta = 0$ that the molecule's anisotropy axis is aligned with the current direction requires to be considered separately. In this case the leading approximation of Eq. (2.33)

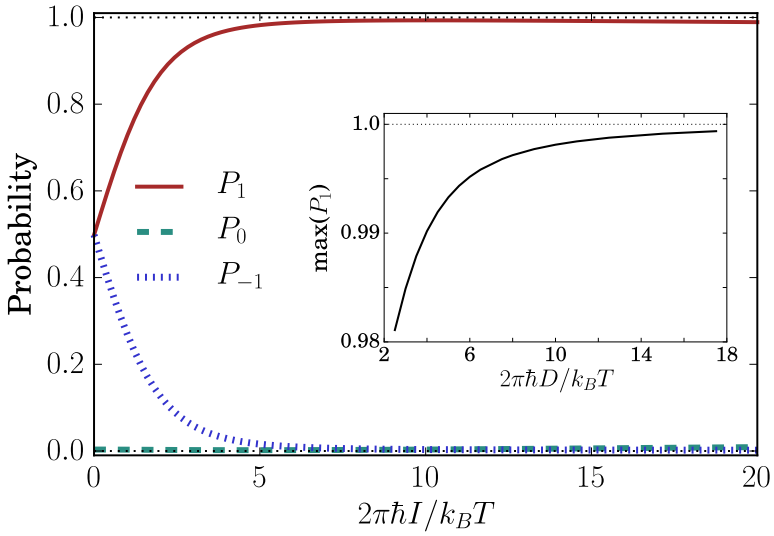

Figure 2.6.: The probabilities P_1, P_0, and P_{-1} for a spin-1 molecule on the surface of a three-dimensional topological insulator to be in the corresponding spin state as a function of $2\pi\hbar I/k_\mathrm{B}T$. We have set $2\pi\hbar D/k_\mathrm{B}T = 5$. The inset shows the maximum value of the probability P_1 for a molecule with $S = 1$ as a function of $2\pi\hbar D/k_BT$.

vanishes for the "upstream" rate $\Gamma_{s-1,s}$ with $s > 0$ and subleading contributions in the small parameter I/D must be taken into account. One finds

$$\Gamma_{s-1,s} \approx J^2(S+s)(S-s+1)\frac{D|2s-1|(k_\mathrm{B}T)^3}{8\pi^4\hbar^3 I^3} \times e^{2\pi\hbar(I-D|2s-1|)/k_\mathrm{B}T} \tag{2.36}$$

if $s > 0$. Asymptotically, for $\hbar I \gg k_\mathrm{B}T$ [but still $I \ll D(2S-1)$], this leads to a complete spin polarization of the molecule,

$$P_s = \delta_{S,s}. \tag{2.37}$$

[The probability P_{-S} vanishes $\propto (k_\mathrm{B}T/\hbar I)^{2S}$; all other probabilities are exponentially small in $\hbar D(2S-1)/k_\mathrm{B}T$.] The perfect polarization can be understood if one observes that the surface-state electrons responsible for the transitions to higher-energy spin states are predominantly electrons moving in the positive z direction, which are then backscattered to the negative z direction. These electrons have a unique spin quantization axis, and their scattering leads to a well-defined change of the molecule's spin state $|s\rangle$. The switching rate from the state $|-S\rangle$ to $|S\rangle$ is given by Eq. (2.35) with $\theta = 0$. The rate for the inverse process $|S\rangle \to -|-S\rangle$ vanishes in the limit $k_\mathrm{B}T \ll \hbar I$.

Remarkably, the complete polarization is lost again when the current is increased further. If $I \gg D(2S-1)$, not only electrons moving in the positive z direction but essentially all electrons that contribute to the current $\mathbf{j}$ can scatter off the localized magnetic moment and change its spin. For high current densities the transition rates are (for arbitrary

direction of the anisotropy axis)

$$\Gamma_{s\pm1,s} \approx \frac{J^2 I(S\mp s)(S\pm s+1)}{2\pi} F_\pm(\theta) \tag{2.38}$$

where we abbreviated

$$F_\pm(\theta) = \frac{4(4-\sin^2\theta)}{3\pi} \pm \frac{\pi}{2}\cos\theta, \tag{2.39}$$

and one quickly obtains the steady-state distribution from here,

$$P_s = \frac{[F_+(\theta)-F_-(\theta)]F_+(\theta)^{S+s}F_-(\theta)^{S-s}}{F_+(\theta)^{2S+1}-F_-(\theta)^{2S+1}}. \tag{2.40}$$

Since $F_\pm(0) = (32\pm3\pi^2)/6\pi$, even for a perfectly aligned molecule no perfect polarization occurs in the limit of large currents. The probability P_S to find the molecule in the maximal-spin state saturates at a value slightly above 96% for molecules with large spin S. Although no perfect polarization results for current densities $I \gg D(2S-1)$, the rate at which the steady-state distribution is approached is considerably enhanced in comparison to the intermediate current-density regime, see Eq. (2.16).

As an illustration, we show the probabilities P_s for $s = -1, 0, 1$ for a molecule with $S = 1$ as a function of the applied current density for $2\pi\hbar D/k_BT = 5$, see Figure 2.6. Notice the (faint) maximum of P_1 for $I \sim D$. The inset shows that the maximum value of P_1 approaches unity in the limit when the anisotropy energy is much larger than the temperature, $\hbar D \gg k_\mathrm{B}T$.

Figure 2.7 shows the mean spin components $\langle \mathbf{S}\cdot\mathbf{e}\rangle$ along the molecule's anisotropy axis and $\langle S_z\rangle$ along the current direction as a function of the angle θ for $S = 5$, for the intermediate-current regime and for the high-current regime. As in the case of a two-dimensional TI, except for $\theta = \pi/2$, the application of a current always results in a net spin in the current direction. For a randomly oriented molecule, the average moment in the current direction approaches $S/2$ in the limit of large S.

We can apply the results obtained here to a topological insulator surface with a dilute covering of molecular magnets. For a dilute covering our single-molecule analysis can be used to obtain the net polarization of the molecular layer. Assuming that the molecules have randomly orientated anisotropy axis—a valid assumption if the magnetic core is shielded by an approximately spherical shell, see, *e.g.*, Ref. [Herm 13]—the net polarization is found by averaging a single molecule's average moment over the directons of the anisotropy axis $\mathbf{e}$. The calculation is straightforward in principle, starting from the steady-state distributions (2.34) and (2.40). [See Eqs. (A.22) and (A.25) for steady-state distributions for half-integer spin S.] Instead of reporting the resulting expressions, which are rather cumbersome, we refer to Figure 2.8, which shows the resulting net polarization per molecule as a function of S.

2.4. Conclusion

The strict spin-momentum locking at the surface of a topological insulator provides an appealing mechanism to use electric currents to switch the spin state of a molecular magnet

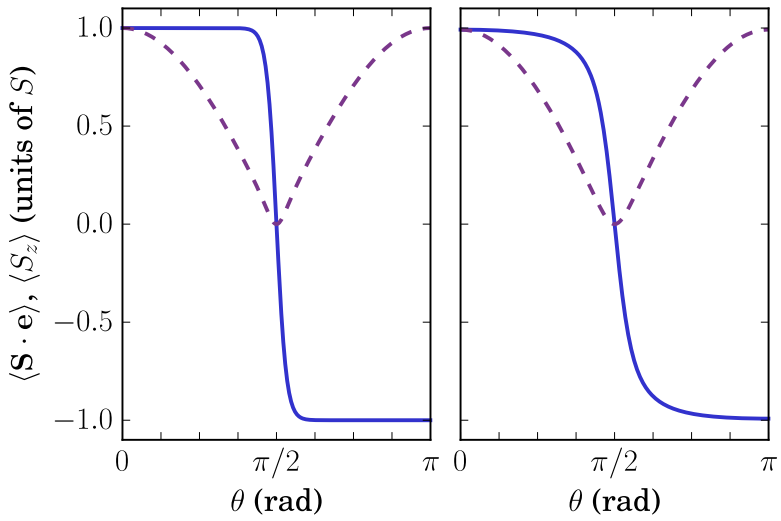

Figure 2.7.: Mean spin component $\langle \mathbf{S} \cdot \mathbf{e} \rangle$ along the direction of the anisotropy axis (solid curve) and the mean spin component $\langle S_z \rangle$ in the current direction (dashed), as a function of the angle θ, for total spin $S = 5$. Left panel: intermediate-current regime $k_\mathrm{B}T \ll \hbar I \ll \hbar D(2S-1)$; right panel: high-current regime $I \gg D(2S-1)$.

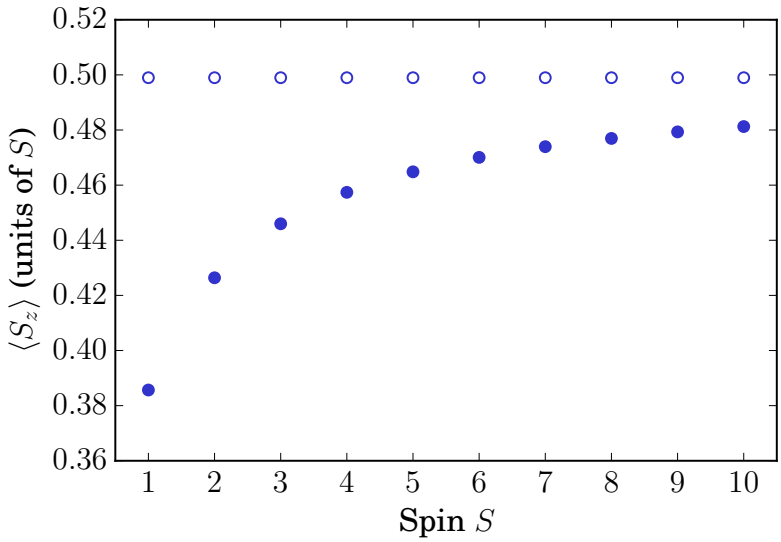

Figure 2.8.: Mean spin component in the current direction $\langle S_z \rangle$ per molecule as a function of the total spin S, for an ensemble of randomly oriented molecular magnets on the surface of a three-dimensional topological insulator. Open circles are for the intermediate-current regime $k_\mathrm{B}T \ll \hbar j \ll \hbar D(2S-1)$; filled circles are for the high-current regime $j \gg D(2S-1)$.

weakly coupled to the surface. Whereas based on simple spin conservation arguments one expects a complete response for a molecular magnet at the edge of a two-dimensional topological insulator if the molecule's magnetic anisotropy axis is aligned appropriately with the spin quantization axis of the surface state, the situation is more complicated for molecular magnets on the surface of a three-dimensional topological insulator and/or for an arbitrary orientation of the magnetic anisotropy axis. For a molecule on the surface of a three-dimensional topological insulator, a full current-induced polarization is achieved only if the molecule's magnetic anisotropy axis is aligned with the current direction and the magnitude j of the current density is in an "intermediate" range $k_\mathrm{B}T \ll \hbar j/k_\mathrm{F} \ll \hbar D(2S-1)$, with $\hbar DS^2$ the molecule's anisotropy energy and S the magnitude of its spin. Yet, even for a surface covered by molecules with randomly oriented anisotropy axes the application of a surface current should result in a net magnetic moment per molecule for all current strengths.

The minimal current density j required to polarize the molecule and the resulting steady-state distribution of the molecule's magnetic states depends more on properties of the topological insulator surface than properties of the molecular magnet itself. The condition for an appreciable current-induced polarization is $j \gg k_\mathrm{B}Tk_\mathrm{F}/\hbar$, *i.e.*, the disortion of the Fermi surface by the applied current should be large in comparison to the blurring of the Fermi surface by temperature. This is a condition that is easier to achieve if the chemical potential is in the vicinity of the Dirac point, so that k_F is small, and a relatively small current density implies a large shift of the distribution function. The role of the anisotropy energy is to set a crossover scale $j \sim D(2S-1)k_\mathrm{F}$, above which current-induced transitions allow the molecule to be in all spin states, whereas for lower current densities only the magnetic ground states $|S\rangle$ and $|-S\rangle$ are accessible. Again, the crossover between these regimes happens at lower current densities if the chemical potential is closer to the Dirac point.

Details of the coupling between the molecule and the surface play a crucial role when it comes to setting the switching rate. This applies both to the zero-current spontaneous switching between the degenerate magnetic ground states $|S\rangle$ and $|-S\rangle$ and to the current-induced changes between these states. If the temperature is below the blocking temperature, appreciable switching rates can be obtained only in the "high-current regime" $j \gg D(2S-1)k_\mathrm{F}$, where we found the switching rate to be of order $\Gamma_\mathrm{switch} \sim J^2 j/k_\mathrm{F}$, where J is the dimensionless exchange coupling. An upper limit for this rate is found by setting $J \sim 1$, although we expect that the presence of the organic shell will typically lead to much smaller exchange couplings for single-molecule magnets on a topological insulator surface. Taking a current density j at the lower end of the high-current regime, $j \sim D(2S-1)k_\mathrm{F}$, we find an upper bound for switching times in the range of 10^{-11} s for a molecule with a blocking temperature of a few K, but most likely significantly longer if J is smaller.

Our calculations have shown that in-plane currents can be used as an effective tool to switch the orientation of the spin of molecular magnets adsorbed on the surface of a three-dimensional topological insulator, even if no complete polarization is achieved for

molecules without a specially aligned magnetic anisotropy axis. We hope that our observations, together with other theoretical studies highlighting the intriguing physics of molecular magnets on TI surfaces [Ower 15], will motivate further experimental and theoretical research in this direction.

3. Dynamical scattering of single-electron wave packets

The ability to characterize properties of wavepackets is an important milestone on the road to electronic realization of quantum optics experiments. It has been proposed to use the transmission of a wavepacket through a constriction with an energy and time dependent transmission probability $T(E,t)$ to perform "tomography" of the wavepacket, *i.e.*, to measure its joint energy-time content [Katoaka, Fletcher, and Johnson, Phys. Status Solidi B 254, 16000547 (2016)]. Here we present a quantum-mechanical theory of how the charge Q transmitted through such a dynamic constriction depends on the Wigner distribution $\rho_{\rm in}(E,t)$ of the wavepacket. Remarkably, for a constriction for which the time-dependence arises from a gate voltage with a linear time dependence, the quantum-mechanical theory agrees with the semiclassical expectation $Q = \int dEdtT(E,t)\rho_{\rm in}(E,t)$.

3.1. Introduction

Electron quantum optics is a relatively new field, aiming to reproduce quantum optics experiments with electron wave packets instead of photons [Gren 11, Bocq 14, Marg 17, Baue 18]. It offers the prospects of probing the interaction between just a few electrons, as well as studying phenomena on the scale of electron coherence time. The field has potentially promising applications in signal processing [Rous 17] and quantum sensing [Demk 12]. Electron quantum optics requires reliable single-electron sources that emit electrons above the Fermi sea into one-dimensional chiral channels, manipulation of the emitted electrons, and controlled measurement after they have passed through the waveguides. Electronic analogs of paradigmatic quantum optics interference experiments, such as the Mach-Zehnder and the Hanbury Brown-Twiss interferometers, have been realized experimentally [Ji 03, Nede 06, Nede 07a, Henn 99, Oliv 99, Kies 02, Nede 07b, Bocq 12]. On-demand single-electron sources have also been successfully fabricated and currently offer an impressive emission frequency in the gigahertz range [Poth 92, Swit 99, Feve 07, Blum 07, Fuji 08, Peko 08, Kaes 08, Wrig 08, Kaes 09, Chor 12, Conn 13, Dubo 13, Ubbe 15, dHol 15].

On the theory side, an important step in establishing the analogy between electron and photon quantum optics has been the investigation of the electric current fluctuations in phase-coherent conductors [Leso 89, Butt 90, Mart 92, Butt 92], paving the way to proposals and analyses of electron interferometry realizations [Samu 04, Ferr 13, Wahl 14, Thib 16]. An additional necessary ingredient in developing electron quantum optics has been the description of electron emission from single-particle sources and its characterization in terms of current, noise, and accuracy [Kaes 08, Hekk 91, Arra 05, Hass 07, Mosk 08, Olkh 08, Hass 08, Haac 13, Ubbe 15, Kash 17, Liti 17, Misi 17].

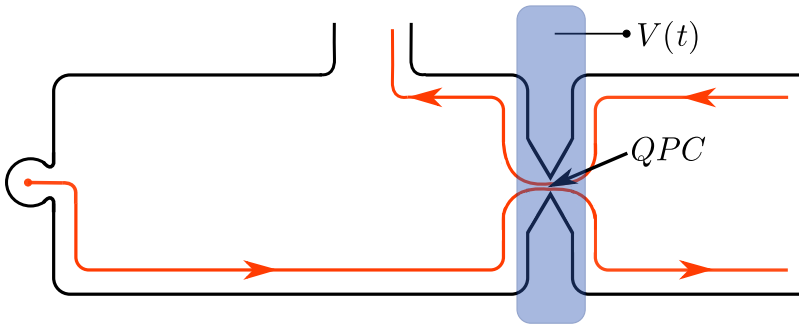

Figure 3.1.: (color online) A sketch of the setup: Two counterpropagating chiral edge states (orange) in a quantum Hall system pass through a quantum point contact (QPC) in which backscattering between the edges is possible. The transmission probability of the QPC can be modulated by a voltage gate placed on top of the QPC. It is assumed that the gate voltage $V(t)$ is spatially uniform in the center region of the QPC, where backscattering between the edge channels takes place. Switching the energy-dependent transmission $T(E)$ of the QPC when a wavepacket emitted from a single electron source (left) passes through the constriction allows for a "tomography"—the measurement of its joint energy-time content—of the wavepacket.

Recently, several advanced detection schemes to characterize single-electron wave packets traveling in one-dimensional edge channels high above the Fermi energy have been reported [Flet 13, Ubbe 15, Wald 15, Kata 16a, John 17, Kata 16b]. These detection schemes rely on measuring the transmission probability of the incoming wavepacket through a constriction with an energy- or time-dependent transmission probability, see Fig. 3.1. For example, by applying a step-like potential in time and varying the onset of the potential, one can determine the arrival time distribution of the wave packet [Flet 13, Wald 15, Kata 16a, Kata 16b], while applying a time-independent potential barrier of height V will give the energy distribution as V is varied [Flet 13, Wald 15].

In a recent work by Fletcher *et al.* [Flet], a classical electron tomography protocol has been proposed and realized that reconstructs the joint energy-time probability distribution $p(E,t)$ of the incoming electrons by measuring the transmitted charge through an energy barrier whose height is varied linearly in time. The two parameters that characterize the barrier (the offset in energy V_0 and the slope α in the time-energy plane) provide a two-dimensional map of the charge $Q(V_0,\alpha)$. The experimental setup can be described using the model of Fig. 3.1, where the time-dependent energy barrier is modelled with a static constriction subject to a (locally) uniform gate voltage $V(t)$. The classical-limit expression for the transmitted charge in this case reads [Flet 13, Kata 16b]

$$Q = e \int dE dt\, T(E) p(E + V(t), t), \tag{3.1}$$

where $T(E)$ is the energy-dependent transmission probability of the constriction in the ab-

sence of the gate voltage. [1] [2] If $T(E)$ is a sufficiently sharp step-function, then Eq. (3.1) represents a conventional tomographic projection of a two-dimensional "image" $p(E,t)$. Using a back-projection algorithm from image processing applications [Smit 97], Fletcher *et al.* [Flet] have performed reconstructions of the incoming energy-time probability distribution $p(E,t)$ from experimentally measured $Q(V_0,\alpha)$.

In this work, we derive a general expression for the transmitted charge for an arbitrary time-dependence of $V(t)$ and show that the classical probability distribution $p(E,t)$ in this case needs to be replaced by a modified Wigner function. We also show that if the gate voltage $V(t)$ has a linear dependence on time, the semiclassical expression Eq. (3.1) is exact. This confirms that the protocol proposed in [Flet] can be used not only for classical but also for quantum tomography, i.e., quantum state reconstruction. We argue that if there are deviations from a linear time dependence of the gate potential, the modified Wigner function instead of the actual incoming Wigner function will be observed. We note that the Wigner distribution function has previously been found to be a useful concept in electron quantum optics [Ferr 13, Jull 14, Kash 17]. It becomes even more relevant as Heisenberg-limited wave packet emission and detection becomes more feasible.

Our manuscript is organized as follows: In Sec. 3.2 we give a precise definition of our system and of the approximations involved, as well as introduce the Wigner distribution function. Our main result, a quantum version of Eq. (3.1), is presented and derived in Sec. 3.3. In that Section we also discuss special cases, such as a gate voltage with a linear time dependence (for which Eq. (3.1) is exact), a gate voltage with sharp edges, and the limit of a slowly varying gate voltage. Section 3.4 illustrates our results, by comparing the "classical" and "quantum" expressions for a few typical examples. In Section 3.5 we discuss how our results relate to experiments. We conclude in Sec. 3.6.

3.2. Model

We consider a constriction with two counterpropagating quantum Hall edge channels. The coordinate x measures the distance along the edge, taking the center of the constriction as the origin, such that points to the left (right) of the constriction have negative (positive) x, see Fig. 3.2. The Hamiltonian for the two counterpropagating edge states reads

$$\hat{H} = -i\hbar v\hat{\sigma}_3\frac{\partial}{\partial x} + \hat{H}_{\rm bs} + \hat{V}(x,t), \tag{3.2}$$

where v is the electron velocity, $\hat{\sigma}_3$ is the Pauli matrix, and the 2×2 matrix structure refers to the two edges. The second term $\hat{H}_{\rm bs}$ describes backscattering in the constriction, and

$$\hat{V}(x,t) = \begin{pmatrix} V_{\rm L}(x,t) & 0 \\ 0 & V_{\rm R}(x,t) \end{pmatrix} \tag{3.3}$$

[1] The expression given in Ref. [Kata 16b] is slightly more general than Eq. (3.1), featuring a transmission probability $T(E,t)$ that depends on energy and time. Equation (3.1) follows upon setting $T(E,t) = T(E-V(t))$, which is the relevant E and t dependence for the geometry considered in Ref. [Kata 16b].

[2] Strictly speaking, in Eq. (3.1) $V(t)$ should be replaced by the integral of the electric field for electrons traveling along the edge, which need not be equal to $V(t)$ for a time-dependent gate potential, see Sec. 3.3.

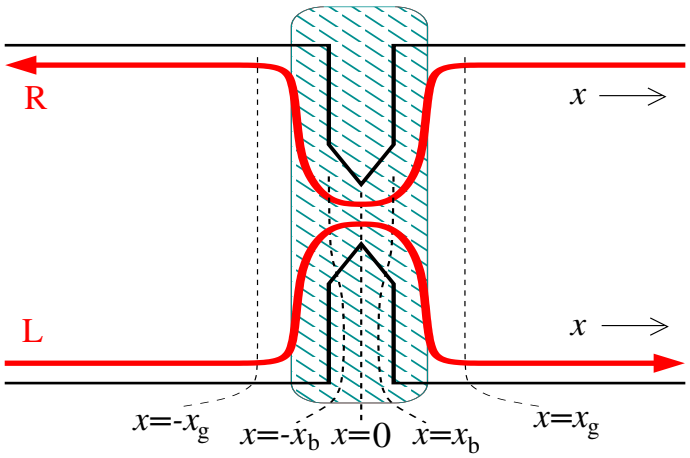

Figure 3.2.: Constriction with two counterpropagating quantum Hall edge modes. The coordinate x measures the distance from the center of the constriction at $x = 0$. Backscattering takes place within the region $-x_\mathrm{b} < x < x_\mathrm{b}$ only; the gate voltage $V(x,t)$ is spatially uniform and equal for both edge modes in this region. The gate voltage is zero for $x > x_\mathrm{g}$ and $x < -x_\mathrm{g}$.

is a gate potential. The backscattering Hamiltonian H_bs is characterized by its transmission probability

$$T(E) = |\tau(E)|^2, \tag{3.4}$$

in the absence of the gate voltage $V(x,t)$, where $\tau(E)$ is the transmission amplitude.

Motivated by the experimental setup of Refs. [Flet 13, Wald 15, Kata 16a, Kata 16b], we take the backscattering term $\hat{H}_\mathrm{bs}$ to be nonzero for $|x| < x_\mathrm{b}$ only, reflecting the fact that backscattering exclusively takes place near the center of the constriction, which is where the two counterpropagating edge states are closest. At the same time, we assume that

$$V_\mathrm{L}(x,t) = V_\mathrm{R}(x,t) = V(t) \text{ for } |x| < x_\mathrm{b}, \tag{3.5}$$

i.e., we take the gate potential to be spatially uniform inside the region where backscattering takes place. Finally, we set the gate potential to zero sufficiently far away from the constriction,

$$V_\mathrm{L}(x,t) = V_\mathrm{R}(x,t) = 0 \text{ for } |x| > x_\mathrm{g}. \tag{3.6}$$

We consider a wavepacket incident on the constriction, such that it reaches the center of the constriction for $t \approx 0$. For times $t \ll 0$ this initial state is described by the wavefunction

$$\psi_\mathrm{in}(x,t) = \varphi_\mathrm{in}(t - x/v) \begin{pmatrix} 1 \\ 0 \end{pmatrix}, \tag{3.7}$$

where the function $\varphi_\mathrm{in}(t)$ is peaked near $t = 0$. The initial-state wavefunction is normalized such that

$$\int_{-\infty}^{\infty} dt |\varphi_\mathrm{in}(t)|^2 = 1. \tag{3.8}$$

Similarly, for times $t \gg 0$ the wavepacket is described by the wavefunction

$$\psi_{\text{out}}(x,t) = \begin{pmatrix} \varphi_{\text{out}}(t - x/v) \\ \varphi'_{\text{out}}(t + x/v) \end{pmatrix}, \tag{3.9}$$

where $\varphi_{\text{out}}(t - x/v)$ represents the transmitted part of the wave packet, and $\varphi'_{\text{out}}(t + x/v)$ represents the reflected part.

Instead of the function $\varphi_{\text{in}}(t)$ it is convenient to use the Wigner transform $\rho_{\text{in}}(E,t)$, which is defined as

$$\rho_{\text{in}}(E,t) = \frac{1}{\pi\hbar} \int_{-\infty}^{+\infty} dt' e^{2iEt'/\hbar} \varphi^*_{\text{in}}(t - t') \varphi_{\text{in}}(t + t'). \tag{3.10}$$

The classical limit of the Wigner distribution function $\rho(E,t)$ is the joint probability density $p(E,t)$ of energy E and time t and corresponds to a Dirac delta distribution peaked around the classical trajectory $E(t)$. Correspondingly, the spread of the Wigner distribution around the classical trajectory is a measure of the quantumness of the wave packet [Kash 17]. The interpretation of $\rho(E,t)$ as a joint probability distribution is not rigorous, though, since the Wigner distribution can also take on negative values. Integrating $\rho(E,t)$ with respect to one of its arguments, however, one obtains a positive function, which is the probability density of the other argument, *i.e.*,

$$\begin{aligned} p(E) &= \int_{-\infty}^{+\infty} \rho(E,t) dt, \\ p(t) &= \int_{-\infty}^{+\infty} \rho(E,t) dE. \end{aligned} \tag{3.11}$$

3.3. Transmitted charge

We now proceed with the calculation of the charge Q transmitted through the constriction,

$$Q = e \int dt |\varphi_{\text{out}}(t)|^2. \tag{3.12}$$

For this calculation it is sufficient to consider the right-moving edge only. We drop the spinor notation of the previous Section, use the scalar wavefunction $\psi(x,t)$ to refer to the wavefunction component at the right-moving edge, and write $V(x,t)$ instead of $V_{\text{L}}(x,t)$.

It is instructive to first discuss the limiting cases of a constriction with a time-independent transmission probability $T(E)$ and a constriction with a transmission probability $T(t)$ that depends on time, but not on energy. In both cases it is a relatively simple calculation to show that the transmitted charge is given as a special case of the classical equation (3.1), with $p(E,t)$ replaced by $\rho_{\text{in}}(E,t)$. Indeed, for a time-independent transmission probability $T(E)$ one finds

$$Q = e \int dE dt T(E) \rho_{\text{in}}(E,t), \tag{3.13}$$

whereas for an energy-independent transmission probability $T(t)$ one has

$$Q = e \int dE dt T(t) \rho_{\mathrm{in}}(E,t). \tag{3.14}$$

We now consider the general case, in which the transmission probability depends on energy and time, specializing to the geometry described in Sec. 3.2, for which the time dependence comes from the gate potential $V(x,t)$.

Since the gate voltage $V(x,t) = 0$ for $x < -x_{\mathrm{g}}$, the initial-state solution (3.7) is valid for all $x < -x_{\mathrm{g}}$. Similarly, the expression (3.9) for the transmitted wavepacket is valid for all $x > x_{\mathrm{g}}$. In the first step of our calculation we solve the time-dependent Schrödinger equation to calculate the wavefunction at all positions $x \leq -x_{\mathrm{b}}$ and $x > x_{\mathrm{b}}$,

$$\begin{aligned} \psi(x,t) &= \varphi_{\mathrm{in}}(t - x/v) e^{-\frac{i}{\hbar}\int_{-\infty}^{t} dt' V[x - v(t-t'),t']}, && x < -x_{\mathrm{b}}, \\ \psi(x,t) &= \varphi_{\mathrm{out}}(t - x/v) e^{\frac{i}{\hbar}\int_{t}^{\infty} dt' V[x - v(t-t'),t']}, && x > x_{\mathrm{b}}. \end{aligned} \tag{3.15}$$

In a second step we perform the gauge transformation

$$\tilde{\psi}(x,t) = \psi(x,t) e^{\frac{i}{\hbar}\int_{-\infty}^{t} V(t')dt'}, \tag{3.16}$$

where $V(t)$ is the value of the gate voltage at the center of the constriction, see Eq. (3.5). For $-x_{\mathrm{b}} < x < x_{\mathrm{b}}$ the transformed wavefunction $\tilde{\psi}$ satisfies a Schrödinger equation without gate voltage, so that

$$\tilde{\psi}(x_{\mathrm{b}}, t + x_{\mathrm{b}}/v) = \int \tau(t - t') \tilde{\psi}(-x_{\mathrm{b}}, t' - x_{\mathrm{b}}/v) dt', \tag{3.17}$$

where

$$\tau(t) = \frac{1}{2\pi\hbar} \int dE \tau(E) e^{-iEt/\hbar} \tag{3.18}$$

is the Fourier transform of the constriction's transmission amplitude $\tau(E)$. [The Fourier transform $\tau(t)$ should not be confused with the time-dependent transmission probability $T(t)$ of Eq. (3.14).] The choice of the offsets in the time arguments in Eq. (3.17) ensure that, for a perfectly transmitting constriction with $\tau(t) = \delta(t)$, $\tilde{\psi}(x,t)$ is a function of $t - x/v$ only. Combining Eqs. (3.15) and (3.17) we find

$$\varphi_{\mathrm{out}}(t) = \int dt' \tilde{\tau}(t,t') \varphi_{\mathrm{in}}(t'), \tag{3.19}$$

with

$$\begin{aligned} \tilde{\tau}(t,t') = e^{-\frac{i}{\hbar}\int_{-\infty}^{t'} dt'' V[-v(t'-t''),t''] - \frac{i}{\hbar}\int_{t'}^{t} dt'' V(t'')} \\ \times e^{-\frac{i}{\hbar}\int_{t}^{\infty} dt'' V[-v(t-t''),t']} \tau(t-t'). \end{aligned} \tag{3.20}$$

Calculating the transmitted charge gives an expression that closely resembles the classical result (3.1) or the limiting cases (3.13) and (3.14),

$$Q = e \int dt dE T(E) \tilde{\rho}(E,t), \tag{3.21}$$

but with the function

$$\begin{aligned}\tilde{\rho}(E,t) = \frac{1}{\pi\hbar} \int dt' \varphi_{\rm in}(t+t') \varphi^*_{\rm in}(t-t')\, e^{2iEt'/\hbar} \\ \times e^{-\frac{i}{\hbar}\int_{-\infty}^{t'} dt'' V[v(t''-t'),t''+t] + \frac{i}{\hbar}\int_{-t'}^{t'} dt'' V(t''+t)} \\ \times e^{\frac{i}{\hbar}\int_{-\infty}^{-t'} dt'' V[v(t''+t'),t''+t]}\end{aligned} \tag{3.22}$$

instead of the classical probability density $p(E,t)$ or the Wigner distribution $\rho_{\rm in}(E,t)$. The integral relation (3.21) and the expression (3.22) are the key results of this chapter. It is tempting to identify the function $\tilde{\rho}(E,t)$ with the Wigner distribution function of the wavepacket somehow modified by the presence of the time-dependent gate voltage, but we have not found a consistent way in which this can be done. Nevertheless, as will be discussed in Sec. 3.5, $\rho(\tilde{E},t)$ can be measured as the outcome of a tomographic reconstruction.

Equation (3.22) takes a considerably simpler form in a few special cases, which we now discuss separately.

Time-independent potential $V(x,t) = V(x)$. — One verifies that for a time-independent potential $V(x,t) = V(x)$ the first and last integrals in the exponentials cancel, so that

$$\tilde{\rho}(E,t) = \rho_{\rm in}(E+V,t), \tag{3.23}$$

where V is the value of the spatially uniform potential in the scattering region. We see that the time-independent V just changes the energy reference level in Eq. (3.13), as expected from gauge invariance.

Gate potential with sharp edges.— In the limit of a spatially constant gate voltage with a sharp edge,

$$V(x,t) = \begin{cases} V(t) & -x_{\rm g} < x < x_{\rm g}, \\ 0 & \text{else}, \end{cases} \tag{3.24}$$

one finds

$$\begin{aligned}\tilde{\rho}(E,t) = \frac{1}{\pi\hbar} \int dt' \varphi_{\rm in}(t+t') \varphi^*_{\rm in}(t-t') \\ \times e^{\frac{2i}{\hbar}Et' + \frac{i}{\hbar}\int_{-t'}^{t'} dt'' V(t+t''-x_{\rm g}/v)}.\end{aligned} \tag{3.25}$$

Note that the value of the gate potential at $t = -x_g/v$ enters, i.e., when the wave packet crosses the edge of the gate.

Linear time dependence.— The experiment of Ref. [Flet] features a potential with a linear time dependence,

$$V(x,t) = V_0(x) + tV_1(x), \tag{3.26}$$

In this case we find that the function $\tilde{\rho}(E,t)$ can be expressed directly in terms of the Wigner distribution $\rho_{\text{in}}(E,t)$ of the incoming wavepacket,

$$\tilde{\rho}(E,t) = \rho_{\text{in}}[E + \mathcal{V}(t), t], \tag{3.27}$$

with

$$\begin{aligned}\mathcal{V}(t) &= \int_{-\infty}^{0} dx \left(\frac{\partial V(x,t')}{\partial x}\right)_{t'\to t+x/v} \\ &= V_0(0) - \frac{1}{v}\int_{-\infty}^{0} dx V_1(x) + V_1(0)t\end{aligned} \tag{3.28}$$

equal to the integral of the electric field along the electron's trajectory. (Note that $\tilde{V}(t)$ need not be equal to the value of the potential $V(x,t)$ at $x = 0$.) Upon comparing Eqs. (3.21) and (3.27) with Eq. (3.1) we conclude that for a potential with linear time dependence the quantum-mechanical theory reproduces the semiclassical approximation (3.1).

Slowly varying potential.— If the rate of change of the gate voltage is slow compared to the velocity of the wave packet, it is reasonable to expand

$$V(x,t) = V_0(x) + V_1(x)t + \frac{1}{2}V_2(x)t^2 + \dots. \tag{3.29}$$

Truncating after the quadratic term, this leads to the formal expression

$$\tilde{\rho}(E,t) = e^{-\frac{1}{24}V_2(0)\hbar^2\frac{\partial^3}{\partial E^3}}\rho_{\text{in}}[E + \mathcal{V}(t), t], \tag{3.30}$$

where

$$\begin{aligned}\mathcal{V}(t) &= \int_{-\infty}^{0} dx \left(\frac{\partial V(x,t')}{\partial x}\right)_{t'\to t+x/v} \\ &= V_0(0) - \int_{-\infty}^{0} dx \left[\frac{V_1(x)}{v} + \frac{V_2(x)x}{v^2}\right] \\ &\quad + \left(V_1(0) - \int_{-\infty}^{0} dx \frac{V_2(x)}{v}\right)t + \frac{1}{2}V_2(0)t^2.\end{aligned} \tag{3.31}$$

Equation (3.30) contains the result (3.27) for a gate potential with a linear time dependence and is a good starting point for an expansion in a small second derivative $V_2(x)$ of the time-dependent gate potential.

Linear time dependence superimposed on an arbitrary gate potential $V'(x,t)$.— If on top of a linear time dependence the potential $V(x,t)$ also contains arbitrary additional terms $V'(x,t)$,

$$V(x,t) = V_0(x) + tV_1(x) + V'(x,t), \tag{3.32}$$

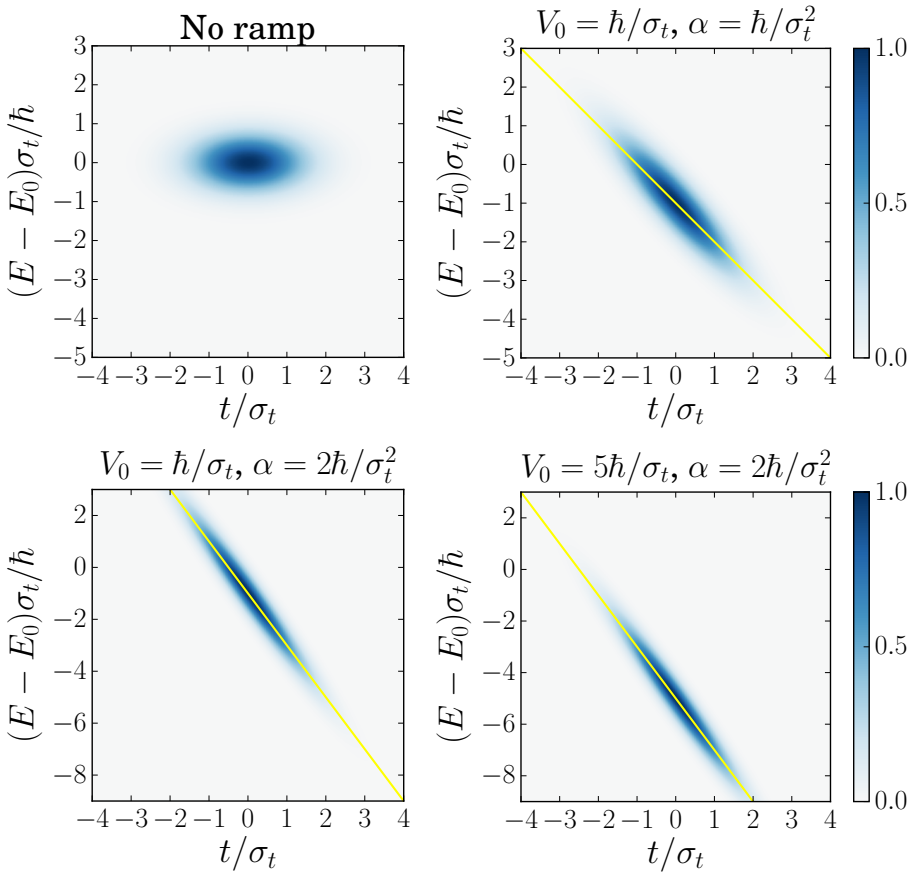

Figure 3.3.: Modified Wigner distribution in units of $1/\hbar$ of a Gaussian wave function after entering a gate with time-dependent potential $V(t) = \alpha t + V_0$ for different values of the ramp rate α and the offset V_0 as shown above. The upper left panel shows the Wigner distribution $\rho_{\text{in}}(E, t)$ of the incoming wavepacket.

the modified Wigner function $\tilde{\rho}(E, t)$ can be expressed as

$$\tilde{\rho}(E, t) = \tilde{\rho}'(E + \mathcal{V}(t), t), \tag{3.33}$$

where $\mathcal{V}(t)$ is given by Eq. (3.28) and $\tilde{\rho}'(E + \mathcal{V}(t), t)$ is calculated with respect to $V'(x, t)$ only. The relevance of this result will be discussed in Sec. 3.5. (Note that Eq. (3.33) simplifies to Eq. (3.27) for the special case $V'(x, t) = 0$.)

3.4. Examples

In this Section we show explicit results for three examples: A gate voltage with linear time dependence, a gate voltage with an abrupt step-like time dependence, and a gate voltage with parabolic time dependence. We take the spatial profile of the gate voltage $V(x, t)$ of the form (3.24), *i.e.*, a spatially uniform potential with sharp edges at $x = \pm x_{\text{g}}$. We also shift the x axis by x_b, so that the point where the wave function enters the scattering region

is $x = 0$ and difference between the integral $\tilde{V}(t)$ of the electric field and the potential $V(t)$ at the center of the constriction can be neglected, see Eq. (3.28). For the incoming wavepacket we take the Gaussian form,

$$\varphi_{\mathrm{in}}(t) = \frac{1}{(2\pi\sigma_t^2)^{1/4}} e^{iE_0 t - \frac{t^2}{4\sigma_t^2}}. \tag{3.34}$$

The scale σ_t sets the characteristic width in the time domain. The energy of the wavepacket is centered around E_0, with fluctuations of order $\hbar/\sigma_t$. The Wigner distribution $\rho_{\mathrm{in}}(E,t)$ corresponding to the wavefunction (3.34) is

$$\rho_{\mathrm{in}}(E,t) = \frac{1}{\pi\hbar} e^{-2(E-E_0)^2\sigma_t^2/\hbar^2 - t^2/2\sigma_t^2}. \tag{3.35}$$

In the three examples discussed below we compute the modified Wigner distribution $\tilde{\rho}(E,t)$, which enters in the expression (3.21) for the transmitted charge, as well as the transmitted charge Q for a quantum point contact with energy-dependent transmission probability [Fert 87]

$$T(E) = \frac{1}{1 + e^{-\pi E/\delta}}, \tag{3.36}$$

where δ gives the width of the energy window in which the transmission changes from 0 to 1 and where we have chosen the zero of energy to coincide with the tipping point of the quantum point contact. For the numerical calculations we will take the idealized limit $\delta \to 0$, corresponding to a point contact that perfectly selects the electron's energy.

3.4.1. Linear ramp

We first consider the case of a gate voltage with a linear time dependence,

$$V(t) = \alpha t + V_0. \tag{3.37}$$

Gate voltages with different offsets V_0 are related by a delay time $t_{\mathrm{d}} = -V_0/\alpha$. For this case the modified Wigner distribution can be obtained from Eq. (3.27), which gives

$$\tilde{\rho}(E,t) = \frac{1}{\pi\hbar} e^{-2(E-E_0+V(t))^2\sigma_t^2/\hbar^2 - t^2/2\sigma_t^2}. \tag{3.38}$$

The modified Wigner distribution for different values of the ramp rate α and the offset V_0 is shown in Figure 3.3, along with the non-transformed Wigner distribution. In comparison to the original Wigner distribution ρ_{in}, the modified distribution $\tilde{\rho}$ has a shifted center energy, determined by the offset V_0, and it is stretched along a straight line with slope $-\alpha$. Figure 3.4 shows the transmitted charge as a density plot in the case of a linear ramp as a function of the parameters α and V_0. As mentioned in the previous Section, for a linear ramp the full quantum-mechanical theory of Sec. 3.3 gives the same result as the classical limit of Eq. (3.1).

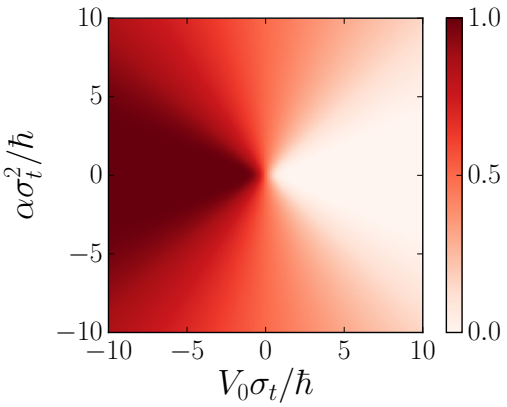

Figure 3.4.: Transmitted charge through the QPC for the case of a linear voltage ramp, as a function of the ramp rate α and the offset V_0.

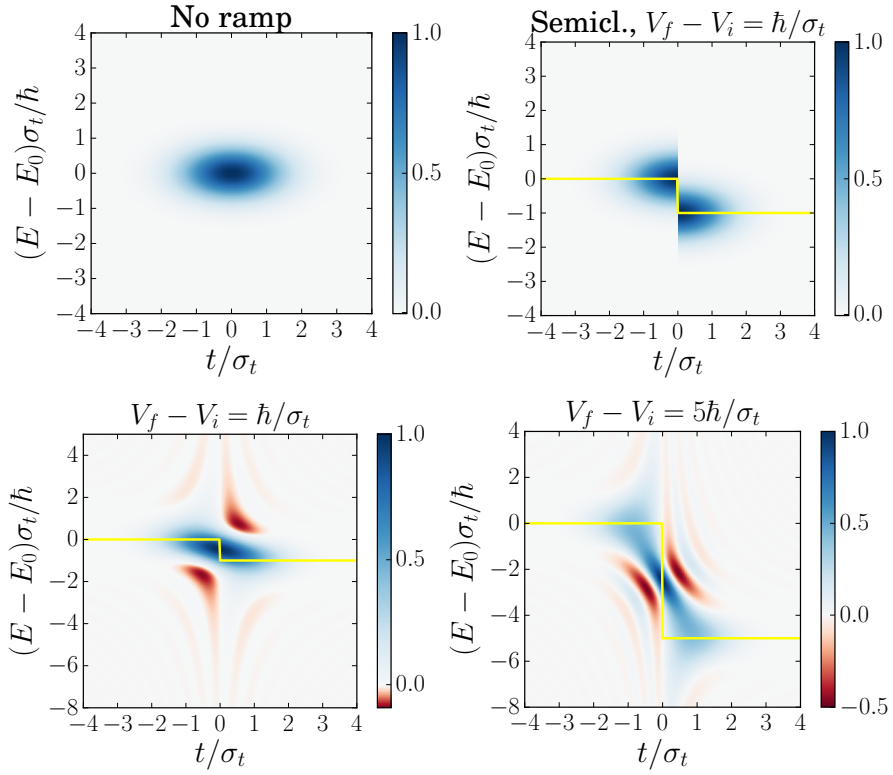

Figure 3.5.: Modified Wigner distribution in units of $1/\hbar$ of a Gaussian wave function after passing through a step-like ramp for different values of the barrier height $V_\mathrm{f} - V_\mathrm{i}$, compared to a non-transformed Wigner distribution (top left panel), as well as the semiclassical approximation (top right panel). We have set $V_\mathrm{i} = E_0$ and $t_0 = 0$.

3.4.2. Step-like ramp

As mentioned in the introduction, performing the detection measurement with an energy-independent transmission probability that abruptly switches on or off allows one to measure the electron probability distribution as a function of time. Such an instantaneous switching on or off of the quantum point contact requires an increase of the gate voltage $V(t)$ by an amount much larger than the energy uncertainty $\hbar/\sigma_t$ of the incoming wavepacket. Information about time and energy can be obtained if the gate voltage jumps by a finite amount at time $t = t_0$,

$$V(t) = \begin{cases} V_\mathrm{i} & \text{for } t < t_0, \\ V_\mathrm{f} & \text{for } t > t_0. \end{cases} \tag{3.39}$$

For a Gaussian incoming wavepacket, the modified Wigner distribution can then be calculated from Eq. (3.25),

$$\begin{aligned} \tilde{\rho}(E,t) = \frac{1}{\pi\hbar} e^{-2(E-E_0+V(t))^2\sigma_t^2/\hbar^2 - \frac{t^2}{2\sigma_t^2}} \operatorname{Re}\left\{ \operatorname{erf}\left[\frac{t-t_0}{\sqrt{2}\sigma_t} + \frac{i\sqrt{2}(E-E_0+V(t))\sigma_t}{\hbar} \right] \right\} \\ + \frac{1}{\pi\hbar} \operatorname{Re}\left\{ e^{-2(E+\bar{V})^2 - \frac{t^2}{2\sigma_t^2} - i(V_\mathrm{f}-V_\mathrm{i})(t-t_0)/\hbar} \operatorname{erfc}\left[\frac{|t-t_0|}{\sqrt{2}\sigma_t} + \frac{i\sqrt{2}(E+\bar{V})}{\hbar} \right] \right\}, \end{aligned} \tag{3.40}$$

where we abbreviated

$$\bar{V} = \frac{1}{2}(V_\mathrm{f} + V_\mathrm{i}) - E_0. \tag{3.41}$$

A comparison between the initial-state Wigner function $\rho_\mathrm{in}(E,t)$, the modified Wigner function $\tilde{\rho}(E,t)$ for two different parameter choices, and the semiclassical expectation $\rho_\mathrm{in}(E+V(t),t)$ is shown Fig. 3.5. Because of the abrupt time dependence at $t = t_0$, the semiclassical expectation is a poor approximation, as can be seen in the figure. In particular, the true modified distribution function is a continuous function of E and t, whereas the semiclassical expectation has a discontinuous jump by $V_\mathrm{f} - V_\mathrm{i}$ at $t = t_0$. The two lower panels of the figure show that in contrast to a linear ramp, a step-like ramp transforms the Wigner distribution such that it assumes negative values.

In Fig. 3.6 we show the transmitted charge at a fixed step height $V_\mathrm{f} - V_\mathrm{i} = 3\hbar/\sigma_t$ as a function of the center potential $\bar{V}$ and the switch time t_0. The top left panel shows the exact result (3.21), and the top right panel the semiclassical approximation (3.1). Their difference is shown in the bottom panel. As expected, if $|\bar{V}|$ is sufficiently large, the transmitted charge is independent of t_0 and approaches 0 or 1 (corresponding to maximum possible transmittance). For intermediate values of $\bar{V}$, there is a transition from 0 to 1 transmitted charge as t_0 goes from large negative to large positive values. Although the exact and the semiclassical results both reproduce the correct limits for large $|\bar{V}|$ and $|t_0|$, the behavior for small $\bar{V}$ and t_0 shows qualitative differences (such as shape of the median $Q = e/2$ curve), as well as quantitative differences (more than $0.1e$, see bottom panel).

3.4.3. Parabolic ramp

The third example is the case of a parabolic ramp, which may serve as an approximation of a periodic (sinusoidal) gate potential near the maximum or minimum of the potential.

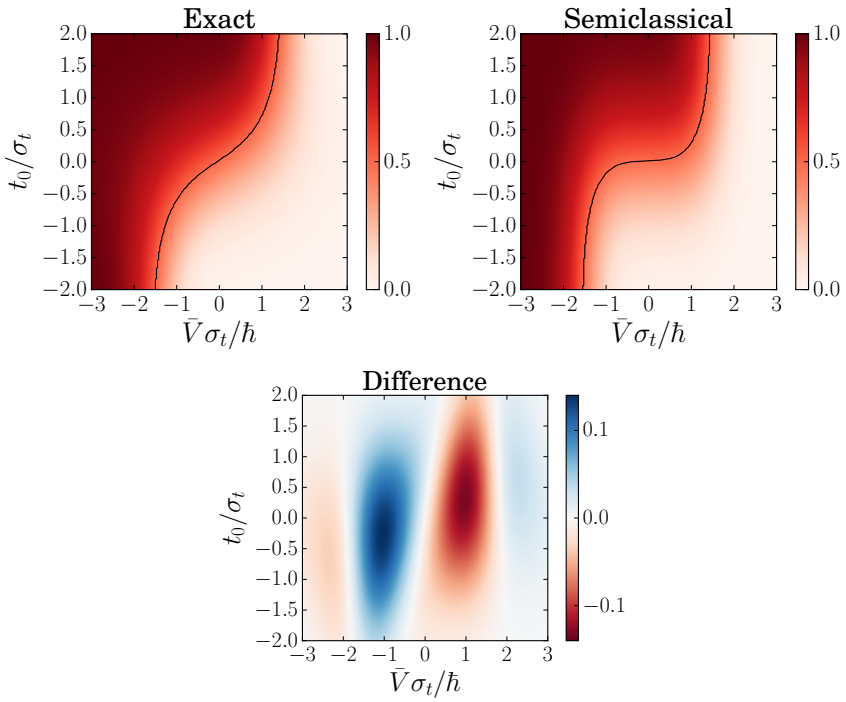

Figure 3.6.: Transmitted charge through the QPC for the case of a step-like ramp as a function of $\bar{V} = (V_\mathrm{f} + V_\mathrm{i})/2 - E_0$ and the switching time t_0. The height of the step $V_\mathrm{f} - V_\mathrm{i}$ is kept fixed and equal to $3\hbar/\sigma_t$. The top left panel shows the exact result; the top right panel shows the semiclassical approximation (3.1). The black curve in the two top panels shows the $Q = e/2$ median. The bottom panel shows the difference between the exact and the semiclassical result.

We consider a gate potential of the form

$$V(t) = V_0 - \frac{1}{2}W(t-t_0)^2. \tag{3.42}$$

Again calculating the modified Wigner function from Eq. (3.25), we find

$$\begin{aligned}\tilde{\rho}(E,t) = &\frac{\sqrt{2/\pi}}{\sigma_t \sqrt[3]{|W|\,\hbar^2}} e^{-\frac{E-E_0+V(t)}{W\sigma_t^2} - \frac{t^2}{2\sigma_t^2} + \frac{\hbar^2}{12W^2\sigma_t^6}} \\ &\times \mathrm{Ai}\left[-\frac{2}{\sigma_t \sqrt[3]{W\hbar}}\left(E - E_0 + V(t) - \frac{\hbar}{8W\sigma_t^3}\right)\right],\end{aligned} \tag{3.43}$$

where $\mathrm{Ai}(z)$ is the Airy function of the first kind.

Figure 3.7 contains a comparison between the exact result for the modified Wigner function, the semiclassical approximation (3.27) and a slow-potential approximation obtained by truncating the exponential in Eq. (3.30) at first order in the second derivative of the potential, for different values of W and for $V_0 = E_0 + \hbar/\sigma_t$, $t_0 = 0$. The figure confirms that both the semiclassical and the slow-potential approximation are good approximations for the modified Wigner function $\tilde{\rho}(E,t)$ if $|W| \ll \hbar/\sigma_t^3$, whereby the slow-potential approximation also faithfully reproduces some of the fringes at larger values of W, which are absent from the semiclassical approximation.

In Fig. 3.8 we show the transmitted charge for two different values of the the curvature parameter W, with separate panels for the exact result, the semiclassical approximation, and the slow-potential approximation. Their difference is shown in the bottom panels. The transmitted charge goes from zero for values of $V_0 - E_0$ far below the line $V_0 - E_0 = \frac{1}{2}Wt_0^2$ to 1 for values of $V_0 - E_0$ far above this line. The differences between the exact and the slow-potential solution grows with W, remaining below 1% for $W = 0.2\hbar/\sigma_t^3$ and going up to 10% for $W = 2\hbar\sigma_t^2$.

3.5. Connection to experiment

In this section, we discuss the relevance of our results to the electron tomography protocol proposed in Ref. [Flet]. As mentioned in the introduction, this protocol provides a map of the transmitted charge $Q(V_0, \alpha)$ (through an energy- and time-dependent barrier) for a gate voltage $V(t) = \alpha t + V_0$ with a linear time dependence as a function of the energy offset V_0 and the energy-time slope $\alpha = \alpha_0 \tan\theta$, where α_0 is a scale factor adapted to the characteristic time and energy scales of the experiment. The quantity

$$\begin{aligned}\frac{\partial Q(V_0,\theta)}{\partial V_0} &= e\int dt dE \frac{\partial T(E - V_0 - \alpha_0 t\tan\theta)}{\partial V_0}\rho_{\mathrm{in}}(E,t) \\ &= e\int dt \rho_{\mathrm{in}}(V_0 + \alpha_0 t\tan\theta, t)\end{aligned} \tag{3.44}$$

represents the Radon transform [Dean 92] of the function $\rho_{\mathrm{in}}(E,t)$, which is experimentally obtained from $\partial Q(V_0,\theta)/\partial V_0$ by the inverse Radon transform using numerical back-projection. In Eq. (3.44) we have used the fact that, according to Eq. (3.27), for a linear ramp the modified Wigner function $\tilde{\rho}(E,t)$ can be expressed in terms of the incoming

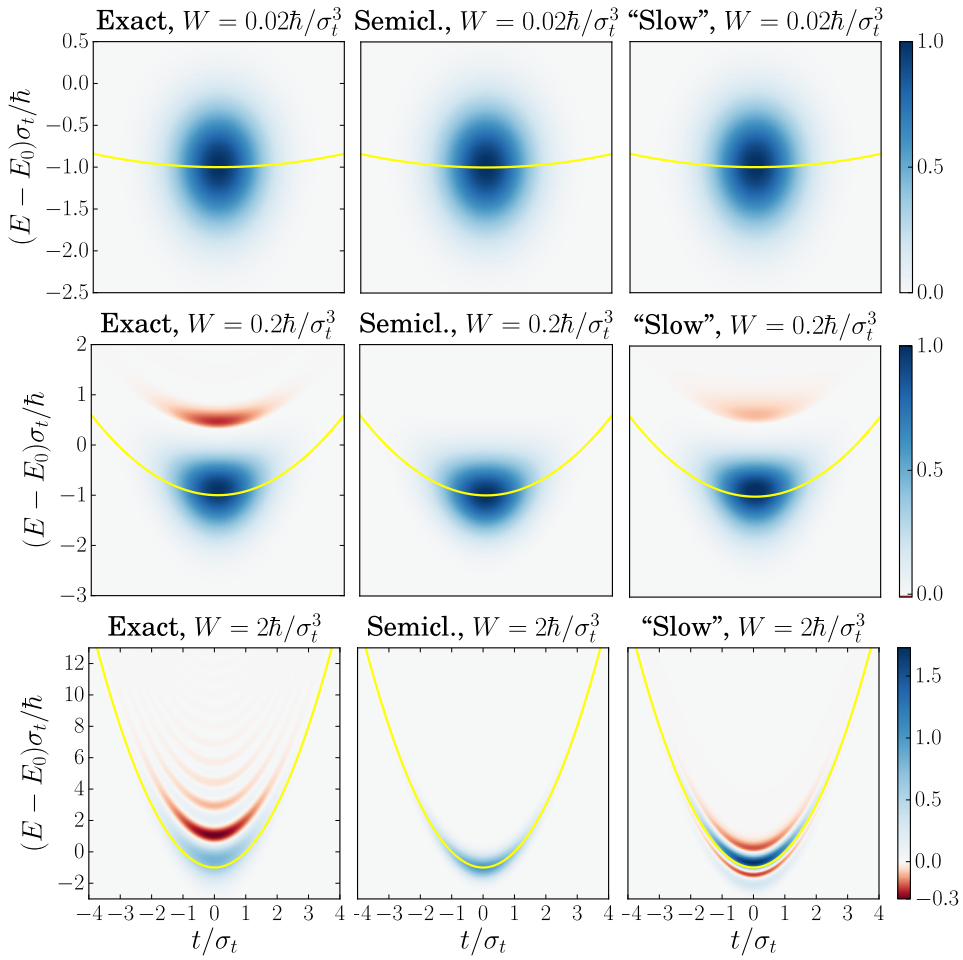

Figure 3.7.: Modified Wigner distribution $\tilde{\rho}$ in units of $1/\hbar$ for a Gaussian wavepacket incident on the QPC. The gate potential $V(t)$ is taken to have the parabolic time dependence (3.42) with $W = 0.02\hbar/\sigma_t^3$ (top), $W = 0.2\hbar/\sigma_t^3$ (center), and $W = 2\hbar/\sigma_t^3$ (bottom). We have set $V_0 = E_0 + \hbar/\sigma_t$ and $t_0 = 0$. The left column shows the full quantum-mechanical result (3.21), the center column shows the semiclassical approximation (3.27), and right column shows the slow-potential approximation, obtained by truncating the exponential in Eq. (3.30) at first order in W.

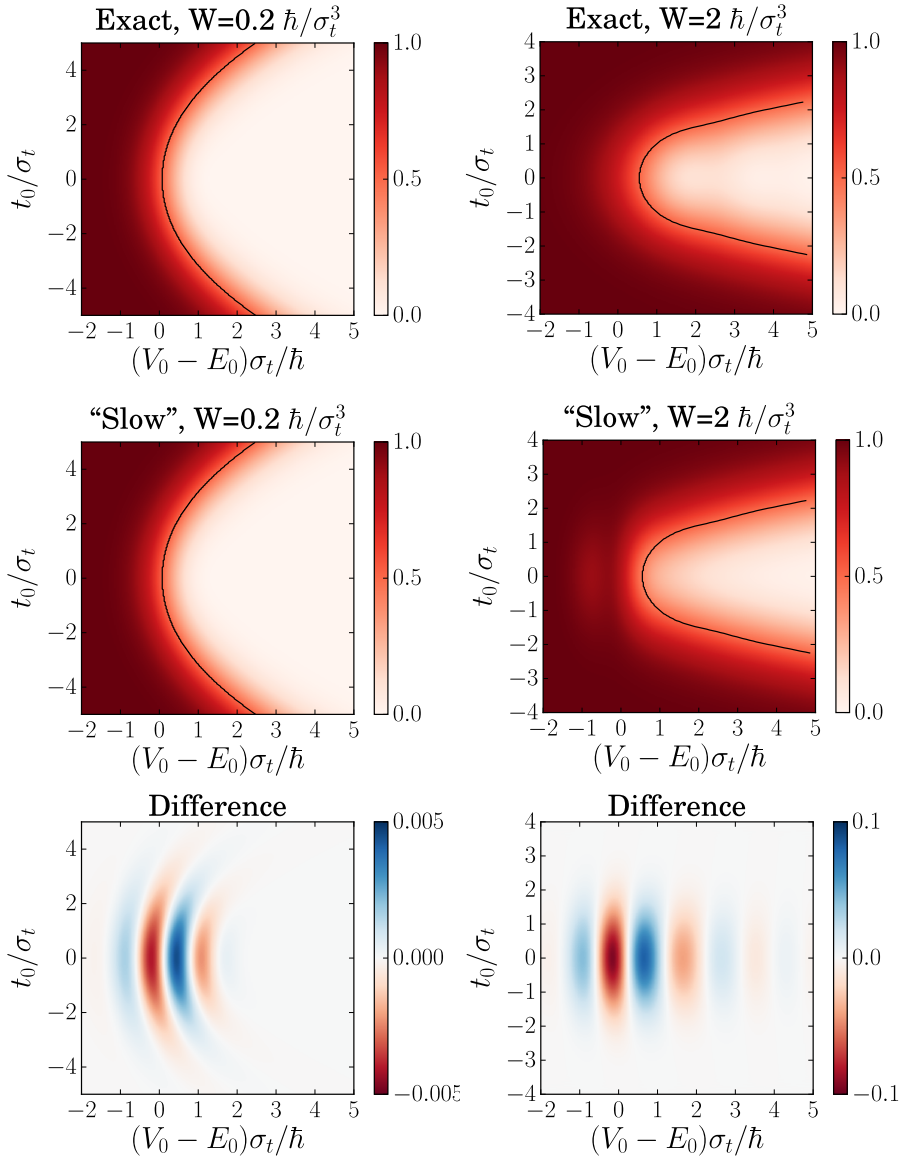

Figure 3.8.: Transmitted charge Q for a Gaussian wavepacket incident on a QPC subject to a gate potential with the parabolic time dependence (3.42) with $W = 0.2\hbar/\sigma_t^3$ (left) and $W = 2\hbar/\sigma_t^3$ (right). The top row is obtained from the full quantum-mechanical expression Eq. (3.21), the center row uses the slow-potential approximation (3.30) with the exponential truncated after first order in the second derivative of the potential. The bottom row shows the difference between the slow-potential approximation and the full quantum-mechanical result.

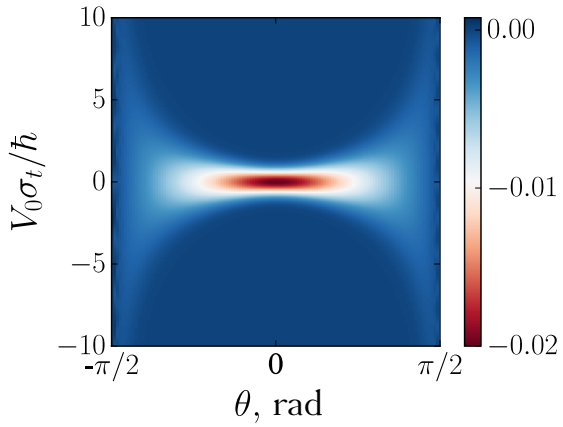

Figure 3.9.: The Radon transform, defined in Eq. (3.44), of the Wigner distribution of a Gaussian wave packet $\rho_{\text{in}}(E,t)$ such as described by Eq. (3.35). We have set $\alpha_0 = \hbar/\sigma_t^2$.

Wigner function $\rho_{\text{in}}(E,t)$ by adding $V(t)$ to the energy. We have also assumed that the transmission probability (3.36) has a sharp enough step in energy space so that its derivative can be replaced by a delta function, which is the case in the tomography experiment of Ref. [Flet]. (A finite width δ of the step of the transmission probability $T(E)$ effectively yields a convolution of the underlying image with a spread function $-\partial T/\partial E$.) To ensure the sharpness of $T(E)$ in the energy space, however, it has to have a width $\Delta t \geq \hbar/\delta$ in time representation, meaning the time that the wave function spends in the scattering region, which in our calculation is on the order of x_b/v, has to be larger than $\hbar/\delta$. This sets the condition

$$\frac{x_b}{v}\delta \geq \hbar \tag{3.45}$$

for an experimental quantum tomography realization.

To illustrate the Radon transform, in Fig. 3.9 we have shown the quantity $\partial Q(V_0,\theta)/\partial V_0$ calculated for the incoming Wigner distribution $\rho_{\text{in}}(E,t)$ of a Gaussian wave packet, exactly like the one depicted in the top left panel of Fig. 3.3. The Radon transform is the line integral of $\rho_{\text{in}}(E,t)$ along the straight line $E = V_0 + \alpha_0 t\tan\theta$. Because the Gaussian distribution has no energy-time correlations, the non-zero values of the Radon transform are concentrated around $\theta = 0$. A correlation between energy and time that has a slope β in the time-energy plane would introduce a shift by $\arctan\beta$ along the θ axis [Flet]. Notice that the width of the non-zero regions along the V_0 axis corresponds to the energy width $\hbar/\sigma_t$ of the Gaussian distribution.

If there are deviations from the linear tomography protocol described in [Flet], the inverse Radon transform of $\partial Q(V_0,\theta)/\partial V_0$ will lead to a function that is different from the desired $\rho_{\text{in}}(E,t)$. A possible concern is the shape of the spatial dependence of $V(x,t)$. The result of Eqs. (3.27) and (3.28) show, however, that a non-sharp edge of the potential would only introduce a constant shift in $\bar{V}(t)$ compared to $V(t)$, leaving the Radon transform unchanged. We have also seen that our calculation does not put any constraints on the

spatial size of the wave packet, as long as the dispersion can be neglected.

As mentioned in Sec. 3.3, the modified Wigner function $\tilde{\rho}(E,t)$ is not a physical observable and does not represent the Wigner function of the wave packet at any stage. However, it can be experimentally obtained as the outcome of tomographic reconstruction. To see this, we consider a gate voltage $V(t)$ that is the sum of a linear part $V_0 + \alpha t$, as in the experiment of Ref. [Flet], and an additional perturbation $V'(t)$. This scenario is discussed theoretically at the end of Sec. 3.3, see Eqs. (3.32) and (3.33). Analogously to Eq. (3.44), the modified Wigner function corresponding to the perturbation $V'(t)$ only, can be expressed as

$$\frac{\partial Q(V_0,\theta)}{\partial V_0} = e \int dt \tilde{\rho}'(V_0 + \alpha_0 t \tan\theta, t), \tag{3.46}$$

where we have inserted $\mathcal{V}(t) = V_0 + \alpha_0 t \tan\theta$ and absorbed the correction to $V(t)$ due to a possibly non-sharp edge of the gate into V_0. This result means that, if we perform the inverse Radon transform of $\partial Q(V_0,\theta)/\partial V_0$ (which experimentally would correspond to numerical back-projection of the measured $\partial Q(V_0,\theta)/\partial V_0$), the outcome would be the modified Wigner transform calculated for the non-linear part $V'(t)$ of the potential $V(t)$ only. For example, the function $\tilde{\rho}(E,t)$ of Eq. (3.40) can be measured using the linear tomographic reconstruction protocol of Ref. [Flet] while applying a gate voltage that is the sum of Eq. (3.37) and Eq. (3.39), i.e.,

$$V(t) = \begin{cases} V_0 + \alpha t + V_\mathrm{i} & \text{for } t < t_0, \\ V_0 + \alpha t + V_\mathrm{f} & \text{for } t > t_0. \end{cases} \tag{3.47}$$

By introducing such a sharp voltage "kick" on top of a linear time dependence of the gate potential, it is possible to determine whether the electron source is coherent, since negative values in the measurement of $\tilde{\rho}'(E,t)$ indicate interference between phase-coherent parts of the incoming wave packet. This is relevant for the investigation of the properties of single-electron sources that emit electrons high above the Fermi energy, since these are largely still unexplored.

Our results also provide a way to describe a different kind of problem: sampling the potential $V(t)$ with single electrons whose incoming distribution is well known. In this case, the deviations in the measurement of $\rho_\mathrm{in}(E,t)$ from the actual incoming distribution can allow us to determine the noise in the applied potential.

3.6. Conclusion

Inspired by a recent experiment [Flet], we have constructed a fully quantum-mechanical description of a dynamical scattering problem of electron wave packets in a one-dimensional chiral channel passing through a constriction subject to a time-dependent gate potential $V(t)$. We have shown that the expression for the transmitted charge in this system is analogous to the classical expression, with a modified Wigner distribution function $\tilde{\rho}$ being the quantum analog of the classical probability distribution. In particular, if the gate voltage has a linear time dependence, as in the recent experiment of Fletcher *et al.* [Flet], the

modified Wigner distribution is obtained from the Wigner function of the incoming electron by a time-dependent shift of the energy E. In this case the full quantum-mechanical theory agrees with the classical-limit estimate (3.1), meaning that the protocol proposed by Fletcher *et al.* also works in the quantum regime.

We have shown that certain conditions have to be fulfilled for the linear tomography model to be valid. To ensure a sharp step in the transmission probability (3.36), the time that the wave function spends inside the scattering region has to be sufficiently large, leading to the requirement $x_b\delta/v \geq \hbar$. We have shown that neither the spatial width of the wave function nor the shape of the edge of the gate (before the scattering region) can spoil the protocol.

A linear time dependence of the gate voltage is in general a good approximation if the electron wavepacket is focused in the time domain. Our full quantum-mechanical theory provides the tools to analyze experiments with a general time dependence of the gate voltage, relevant for wavepackets that are stretched in the time domain. The results presented here can be used to describe existing and propose new tomography protocols. They can also serve to analyze a reverse problem: determining the gate potential $V(t)$ when the incoming electron distribution is known. We have also proposed a way to measure the modified Wigner function using the tomographic reconstruction protocol proposed by Fletcher *et al.* [Flet], which could be used to probe the coherence of electron sources.

4. Single-molecule transistor

In this chapter, we employ a rate equation approach to explain the experimental results reported by Martínez-Blanco *et al.* [Mart 15], in particular the appearance of a conductance gap in the dI/dV measurements of a molecular transistor at all gate potentials. The crucial ingredient in the model is the existence of two different molecular conformations with differently charged lowest-energy states. This leads to a modified picture of the Coulomb blockade regime, with the two Coulomb diamond pictures of the two conformations superimposed on top of each other. It also allows us to explain the experimentally observed hysteresis.

The chapter is organized as follows: We start with a motivation of the problem and describe the relevant experiment in Section 4.1. In Section 4.2.1 we rederive the familiar Coulomb diamond picture to illustrate our approach, and extend it to the case of two molecular conformations in Section 4.2.2. We present the results and discuss their agreement with experiment in Section 4.3. We conclude in Section 4.4.

4.1. Introduction

Ever since the invention of the first transistor in 1947 by Bardeen, Brattain, and Shockley, there has been an effort to improve transistor efficiency in terms of energy consumption, speed, and size. The progress in solid state physics has largely been responsible for (and driven by) the technological advancements in the last 50 years. With the size of electronic computation units decreasing exponentially, limitations to the conventional way of manufacturing transistors have appeared, such as energy dissipation and interference. In 1977, Thouless showed [Thou 77] that for small enough conductors, their size influences their transport properties. This was followed by decades of exploration of the electronic conductance characteristics on the meso- and nanoscale. A particular milestone in this regard was the first experimental realization of the single-electron transistor [Fult 87]. Since then, many experiments have realized the single-electron transistor in different settings: as electrostatically-defined quantum dots in semiconductor heterostructures [Schu 97], nanocrystal particles attached to leads [Klei 96, Klei 97, Murr 00, Fuec 10], break junctions [Ohni 98, Selz 06], carbon nanotubes [Bock 97, Tans 97, Yao 99, Post 01], semiconductor nanowires [Heis 13], and graphene quantum dots [Pono 08]. A theory to describe the transport through quantum dots has also been developed [Been 91, Brou 95, Brou 98, Been 97, Imry 99, Silv 00, Alha 00].

In contrast to a conventional transistor, a single-electron transistor [Naza 09] transports electrons through it one by one. This is possible because the transistor is operated in the Coulomb blockade regime where the small size of the conductor (which is usually defined with eletrostatic gates) makes the quantization of the energy levels observable and the charging energy of the dot becomes large compared to the tunneling energy and

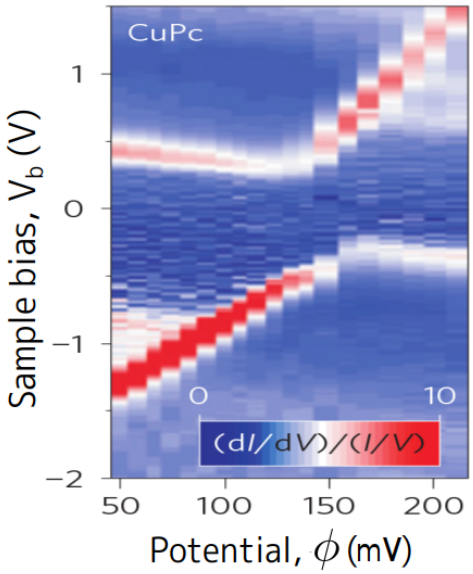

Figure 4.1.: STM measurement data of the normalized differential current through a single-molecule transistor as a function of the gate voltage ϕ and bias voltage V_b. Figure taken from [Mart 15].

the temperature. The study of single-electron transistors provides insights into electronic properties on the quantum level, such as interference, sequential electron tunneling, and coherent tunneling in regimes where sequential tunneling is blocked and higher order processes can be observed, as well as current quantization and conductance oscillations.

From an application standpoint, single-electron transistors offer the prospect of controlling the transport of individual electrons and reducing the size of electronic devices. A fundamental limitation on the size of such devices is the size of an atom, regardless of the method used to fabricate it. Since achieving this limit with top-down approaches (such as lithography) is challenging, different self-assembling systems have been proposed. Among them are (mostly organic) molecules that can serve as quantum dots due to their discrete energy levels. A shortcoming of this approach has been the lack of ability to gate the molecules, which in the case of lithographic quantum dots was done using metallic gates applied on top of a two-dimensional electron gas.

However, in a recent experiment by Martínez-Blanco *et al.* [Mart 15], it was possible to gate a phthalocyanine molecule adsorbed on an InAs(111)A surface using positively charged indium ions positioned on the surface with a scanning tunneling microscope (STM) tip. They were able to create different configurations of the indium ions that allowed for a wide range of gating potentials in the millivolt domain. The bias voltage was applied through the STM tip, with the tip serving as the source and the InAs surface as the drain. The measurement of the current flowing through the molecule as a function of the gate and bias voltages revealed an interesting result that differed from those of previous single-electron transistors: there was a conductance gap at all gate voltages. The corresponding figure from Ref. [Mart 15] is shown in Fig. 4.1.

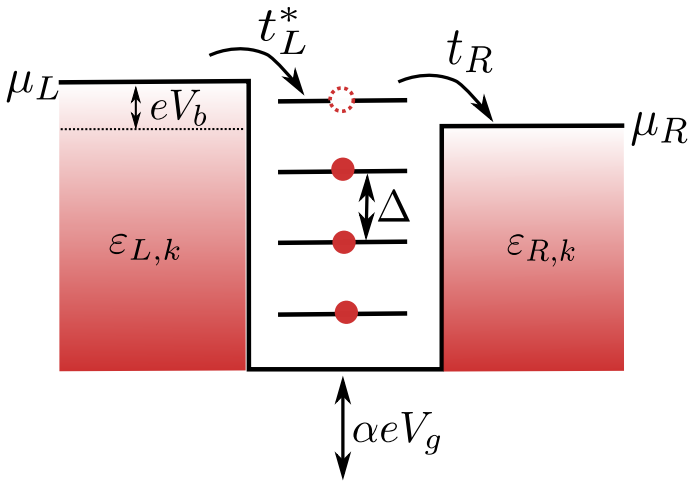

Figure 4.2.: A sketch of the model. A quantum dot with discrete energy levels and average spacing Δ connected to two leads with chemical potentials μ_L and μ_R and electronic states $\varepsilon_{L,k}$ and $\varepsilon_{R,k}$. A bias $eV_b = \mu_L - \mu_R$ is applied. The energy levels of the dot can be shifted by the gate voltage V_g. The tunneling amplitude from the dot to the leads is $t_{L/R}$.

We will now show that this experimental result can be explained if the molecule can assume two different conformations that each separately would give the conventional Coulomb blockade diagrams but, when combined, behave qualitatively in the way seen in Fig. 4.1.

4.2. Model

4.2.1. Coulomb blockade

We will start by solving the problem in the case of only one molecular conformation, which will lead to the known Coulomb diamond picture. This will both illustrate the basis of our approach and provide a direct comparison between the conventional case and the case with two molecular conformations.

A sketch of the system is shown in Fig. 4.2. The molecule, which we model as a quantum dot with discrete energy levels, is connected to two leads, left (L) and right (R), with chemical potentials μ_L and μ_R, respectively. The difference $\mu_L - \mu_R = eV_b$ is the bias voltage applied to the dot. The average spacing Δ between the dot levels is assumed to be larger than the bias voltage, $\Delta > V_b$, and much larger than the temperature, $\Delta \gg k_B T$. The energy spectrum $\varepsilon_{L/R,k}$ of the states in the leads is effectively continuous compared to the discrete energy levels on the dot and obeys the Fermi-Dirac distribution. We work in the wide-band limit and assume that the tunneling amplitude between the dot and the leads, denoted by $t_{L/R}$, is independent of energy. In addition, we assume $|t_{L/R}| \ll k_B T$, so that electron coherence is destroyed by the temperature and the tunneling is sequential. The gate voltage V_g can shift the levels of the dot with a lever arm factor α which we

derive below. Additionally, we also allow for the bias voltage V_b to shift the energy levels with a lever arm factor η. This combines to the total Hamiltonian of the system,

$$\mathcal{H} = H_{\text{dot}} + H_{\text{leads}} + H_{\text{tunnel}}, \tag{4.1}$$

where

$$H_{\text{dot}} = \sum_n \varepsilon_n \hat{c}_n^\dagger \hat{c}_n + U(\hat{N}) \tag{4.2}$$

is the Hamiltonian of the dot with $\hat{N} = \sum_n \hat{c}_n \hat{c}_n^\dagger$ the number operator,

$$H_{\text{leads}} = \sum_{j=L,R} \sum_k (\varepsilon_{j,k} - \mu_j) \hat{c}_{j,k}^\dagger \hat{c}_{j,k} \tag{4.3}$$

describes the states in both leads, and

$$H_{\text{tunnel}} = \sum_{j=L,R} \sum_k \sum_n \left(t_j \hat{c}_{j,k}^\dagger \hat{c}_n + t_j^* \hat{c}_n^\dagger \hat{c}_{j,k} \right) \tag{4.4}$$

describes tunneling.

While ε_n are the single-particle energy levels of the dot due to spatial confinement alone, the second term in H_{dot} contains the effects of Coulomb interaction between the N electrons on the dot, as well as the effects of the gate and bias voltages. Typically, $U(\hat{N}) \gg \varepsilon_n$ for dots with a large number of electrons N. $U(\hat{N})$ can be expressed as

$$U(\hat{N}) = \frac{e^2}{2C_\Sigma} \hat{N}^2 + \alpha e \hat{N} V_g + \eta e \hat{N} V_b, \tag{4.5}$$

where C_Σ is the total capacitance between the dot and the electrodes, and α, η are derived using Kirchhoff's circuit laws. The corresponding circuit is shown in Fig. 4.3, with C_L, C_R, and C_g denoting the capacitances between the dot and the left lead, right lead, and the gate, respectively. The charges on the three capacitors are denoted by q_L, q_R, and q_g. The charge on the dot is eN and has to be an integer number of elementary charges. The Kirchhoff equations then read

$$\begin{cases} -q_L + q_R + q_g = eN, \\ \dfrac{q_L}{C_L} + \dfrac{q_R}{C_R} = V_b, \\ \dfrac{q_R}{C_R} - \dfrac{q_g}{C_g} = V_g. \end{cases} \tag{4.6}$$

Solving for q_L, q_R, and q_g and inserting the result into the expression for the electrostatic energy on the dot,

$$U_N = \frac{q_L^2}{2C_L} + \frac{q_R^2}{2C_R} + \frac{q_g^2}{2C_g} - q_L V_b + q_g V_g, \tag{4.7}$$

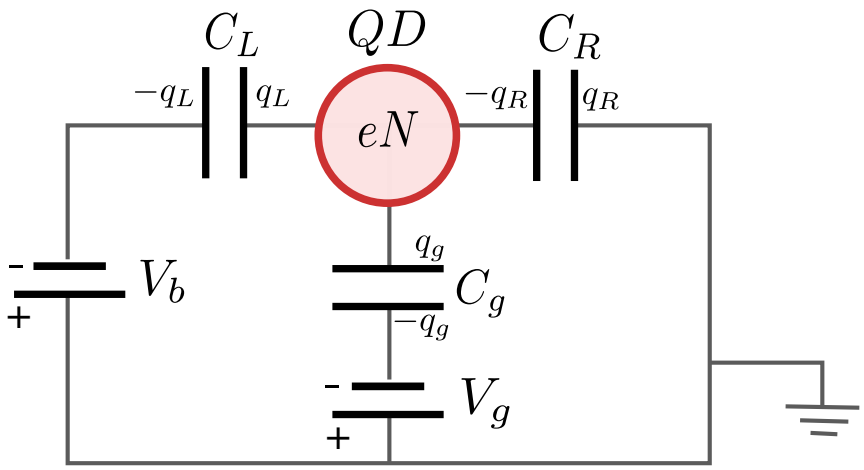

Figure 4.3.: The circuit used for deriving the electrostatic energy U_N of the dot (red circle). The capacitances between the dot and the left, right, and gate electrodes are denoted with C_L, C_R, and C_g, respectively. The corresponding charges on the capacitor plates are q_L, q_R, and q_g. The charge on the dot is eN with N an integer number.

we obtain after comparing terms with Eq. (4.5):

$$\alpha = \frac{C_g}{C_L + C_R + C_g} \equiv \frac{C_g}{C_\Sigma} \quad \text{and} \quad \eta = \frac{C_L}{C_L + C_R + C_g} \equiv \frac{C_L}{C_\Sigma}. \tag{4.8}$$

We can now derive the conditions for the existence of sequential tunneling through the dot. This will be possible if at least one dot level is in the bias window between μ_R and μ_L. If the applied bias is positive, $V_b = \mu_L - \mu_R > 0$, the current will flow from the left lead to the right, and the two conditions for this are

$$\begin{cases} U_{N+1} - U_N - eV_b \leq 0, \\ U_N - U_{N+1} \leq 0, \end{cases} \tag{4.9}$$

where the first condition requires that it is energetically favorable for an electron to enter the dot from the left lead into the $(N+1)$-th level, while the second condition makes tunneling to the right lead from the same level possible. We have not included the single-particle energies ε_n in these expressions since they do not depend on the applied voltages and therefore will not influence the slopes in the V_g-V_b diagram that determine the regions of sequential tunneling. For a current flow in the opposite direction (and therefore negative V_b), the conditions are

$$\begin{cases} U_N - U_{N+1} + eV_b \leq 0, \\ U_{N+1} - U_N \leq 0. \end{cases} \tag{4.10}$$

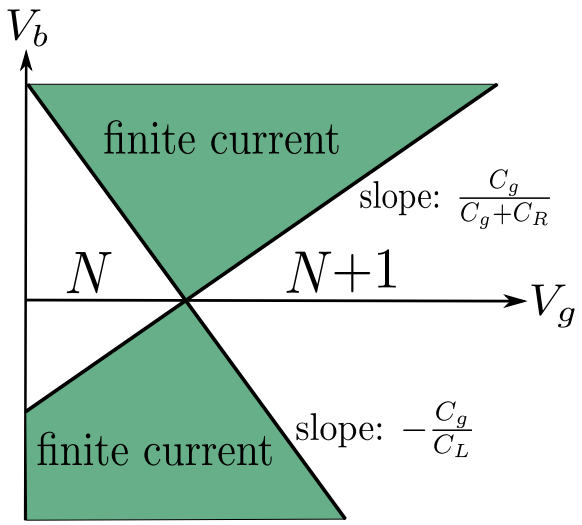

Figure 4.4.: Diagram showing regions with zero current (white) and finite current (green) as a function of the gate voltage V_g and bias voltage V_b. In the white regions, sequential tunneling is blocked by Coulomb interaction, and the quantum dot is in a well-defined stable charge state with N or $N+1$ electrons. In the green regions, the $(N+1)$-th level is within the bias window and sequential tunneling leads to a finite current.

Solving the inequalities (4.9) and (4.10) for V_b as a function of V_g, we obtain

$$\begin{cases} V_b \geq \dfrac{C_g}{C_g+C_R}V_g + \dfrac{e(2N+1)}{2(C_g+C_R)}, \\ V_b \geq -\dfrac{C_g}{C_L}V_g - \dfrac{e(2N+1)}{2C_L} \end{cases} \tag{4.11}$$

for a current from the left to the right lead and

$$\begin{cases} V_b \leq \dfrac{C_g}{C_g+C_R}V_g + \dfrac{e(2N+1)}{2(C_g+C_R)}, \\ V_b \leq -\dfrac{C_g}{C_L}V_g - \dfrac{e(2N+1)}{2C_L} \end{cases} \tag{4.12}$$

for a current from the right to the left lead. In the V_g-V_b plane this gives regions where the system is conducting, known as Coulomb diamonds. They are schematically shown in Fig. 4.4. As seen in the figure, the conductance gap closes as the number of electrons on the dot changes by 1. At this charge degeneracy point, both charge states have the same energy, equal to $\mu_L = \mu_R$ ($V_b = 0$ at this point).

To find a quantitative expression for the current flowing through the dot, we use a rate equations approach. As mentioned before, the assumption of weak coupling between the dot and the leads, $|t_{L/R}| \ll k_B T$, allows us to only consider sequential tunneling. In this

regime the electrons spend a long time on the dot compared to the tunneling timescale and the level broadening in the dot is very small. We assign a probability $P_N(t)$ to finding N electrons on the dot and denote the transition rate between two different charge states by $\Gamma_{N\to N\pm1}$. Such a transition takes place when an electron enters or leaves the dot, which can happen via the left or the right lead. $\Gamma_{N\to N\pm1}$ is therefore a sum of the transition rates to or from the two leads,

$$\Gamma_{N\to N\pm1} = \Gamma^L_{N\to N\pm1} + \Gamma^R_{N\to N\pm1}. \tag{4.13}$$

To derive the transition rates, we use Fermi's golden rule and treat the tunneling Hamiltonian H_{tunnel} from Eq. 4.4 as a perturbation to $H_{\text{dot}} + H_{\text{leads}}$. For $\Gamma^L_{N\to N+1}$ this gives

$$\Gamma^L_{N\to N+1} = \frac{2\pi}{\hbar}\sum_k \left|\langle N+1|\, H_{\text{tunnel}}\, |N;L,k\rangle\right|^2 \delta(U_{N+1}+\varepsilon_{N+1}-U_N-\varepsilon_N-\varepsilon_k) \tag{4.14}$$

$$= \frac{|t_L|^2}{2\pi\hbar}\int d\varepsilon_k d\varepsilon_{k'}\left|\langle L,k'|\, L,k\rangle\right|^2 \delta(U_{N+1}+\varepsilon_{N+1}-U_N-\varepsilon_N-\varepsilon_k) \tag{4.15}$$

$$= \frac{|t_L|^2}{\hbar} f(U_{N+1}+\varepsilon_{N+1}-U_N-\varepsilon_N-eV_b), \tag{4.16}$$

where we have assumed that the states in the lead obey the Fermi-Dirac distribution $f(\varepsilon) = (e^{\varepsilon/k_BT}+1)^{-1}$, and have taken the continuous limit $\sum_k \to \frac{1}{2\pi}\int d\varepsilon_k$. We have also set $\mu_R = 0$ and therefore $\mu_L = eV_b$. The initial state $|N;L,k\rangle = |N\rangle \otimes |L,k\rangle$ describes a dot with N electrons and a state in the left lead. The final state $|N+1\rangle = |N+1\rangle \otimes |0\rangle$ describes a state with $N+1$ electrons in the dot. In an analogous way we obtain

$$\Gamma^R_{N\to N+1} = \frac{|t_R|^2}{\hbar} f(U_{N+1}+\varepsilon_{N+1}-U_N-\varepsilon_N) \tag{4.17}$$

and therefore

$$\Gamma_{N\to N+1} = \frac{|t_L|^2}{\hbar} f(U_{N+1}+\varepsilon_{N+1}-U_N-\varepsilon_N-eV_b) + \frac{|t_R|^2}{\hbar} f(U_{N+1}+\varepsilon_{N+1}-U_N-\varepsilon_N). \tag{4.18}$$

The rate for tunneling out of the dot is

$$\Gamma_{N+1\to N} = \frac{|t_L|^2}{\hbar} f(U_N+\varepsilon_N-U_{N+1}-\varepsilon_{N+1}+eV_b) + \frac{|t_R|^2}{\hbar} f(U_N+\varepsilon_N-U_{N+1}-\varepsilon_{N+1}). \tag{4.19}$$

We can now set up the rate equations. Assuming the bias voltage is low enough ($V_b < \Delta$) such that only two charge states (N and $N+1$) take part in the transport, we have

$$\begin{cases} \dfrac{dP_N(t)}{dt} = \Gamma_{N+1\to N}P_{N+1}(t) - \Gamma_{N\to N+1}P_N(t), \\ \dfrac{dP_{N+1}(t)}{dt} = \Gamma_{N\to N+1}P_N(t) - \Gamma_{N+1\to N}P_{N+1}(t), \\ P_N(t) + P_{N+1}(t) = 1, \end{cases} \tag{4.20}$$

where the third equation is probability conservation. To find the stationary probabilities, we set the left hand side of the first two equations to zero, and solving this leads to

$$P_N = \frac{\Gamma_{N+1\to N}}{\Gamma_{N+1\to N} + \Gamma_{N\to N+1}} \quad \text{and} \quad P_{N+1} = \frac{\Gamma_{N\to N+1}}{\Gamma_{N+1\to N} + \Gamma_{N\to N+1}}. \tag{4.21}$$

The expression for current I in the stationary case is

$$I = e\left(\Gamma^L_{N\to N+1} P_N - \Gamma^L_{N+1\to N} P_{N+1}\right). \tag{4.22}$$

Since we are interested in the current for the case with two conformations, we will now extend these results to include different conformations.

4.2.2. Extension to two conformations

The motivation for introducing two different molecular conformations is the following. For each of the conformations, which we will denote by a and b, a Coulomb diamond picture such as the one depicted in Fig. 4.4 will hold. But the charge degeneracy point need not be the same for both conformations, and if the N-th charge state of conformation a has lower energy than the N-th charge state of conformation b, but the opposite is true for $N+1$, then the finite current region will be restricted to the region where the individual finite current regions of a and b overlap. This is illustrated in Fig. 4.5, where we have specified $N = 0$, since this is the case in the experiment. If the molecule is not charged, conformation with the lower energy is always a. If it is charged (with one electron from the STM tip), the stable conformation is always b. As the gate voltage increases and shifts the energy of the charged states with respect to the neutral ones, the stable state of the system goes from the neutral state of a to the charged state of b. Since the molecule will be in conformation a at the charge degeneracy point of conformation b, and vice versa, there will always be a conductance gap in the V_g-V_b diagram. This is in qualitative agreement with the experimental results shown in Fig. 4.1.

To calculate the current in the case of two conformations, we extend Eq. (4.22) to

$$I = e\left(\Gamma^{L,a}_{N\to N+1} P_N + \Gamma^{L,b}_{N\to N+1} P_N - \Gamma^{L,a}_{N+1\to N} P_{N+1} - \Gamma^{L,b}_{N+1\to N} P_{N+1}\right), \tag{4.23}$$

where the transition rates $\Gamma^{L,a/b}_{N\to N\pm1}$ are derived in the same way as in the previous section, only with different single-particle energies $\varepsilon^{a,b}_n$ for each conformation. We assume the same capacitive coupling C_L, C_R, C_g to the electrodes for both conformations, leaving U_N independent of a and b. The tunneling amplitude $t_{L/R}$ is also assumed the same for both conformations. The transition rates therefore read

$$\Gamma^{a/b}_{N\to N+1} = \frac{|t_L|^2}{\hbar} f(U_{N+1} + \varepsilon^{a/b}_{N+1} - U_N - \varepsilon^{a/b}_N - eV_b) + \frac{|t_R|^2}{\hbar} f(U_{N+1} + \varepsilon^{a/b}_{N+1} - U_N - \varepsilon^{a/b}_N) \tag{4.24}$$

and

$$\Gamma^{a/b}_{N+1\to N} = \frac{|t_L|^2}{\hbar} f(U_N + \varepsilon^{a/b}_N - U_{N+1} - \varepsilon^{a/b}_{N+1} + eV_b) + \frac{|t_R|^2}{\hbar} f(U_N + \varepsilon^{a/b}_N - U_{N+1} - \varepsilon^{a/b}_{N+1}). \tag{4.25}$$

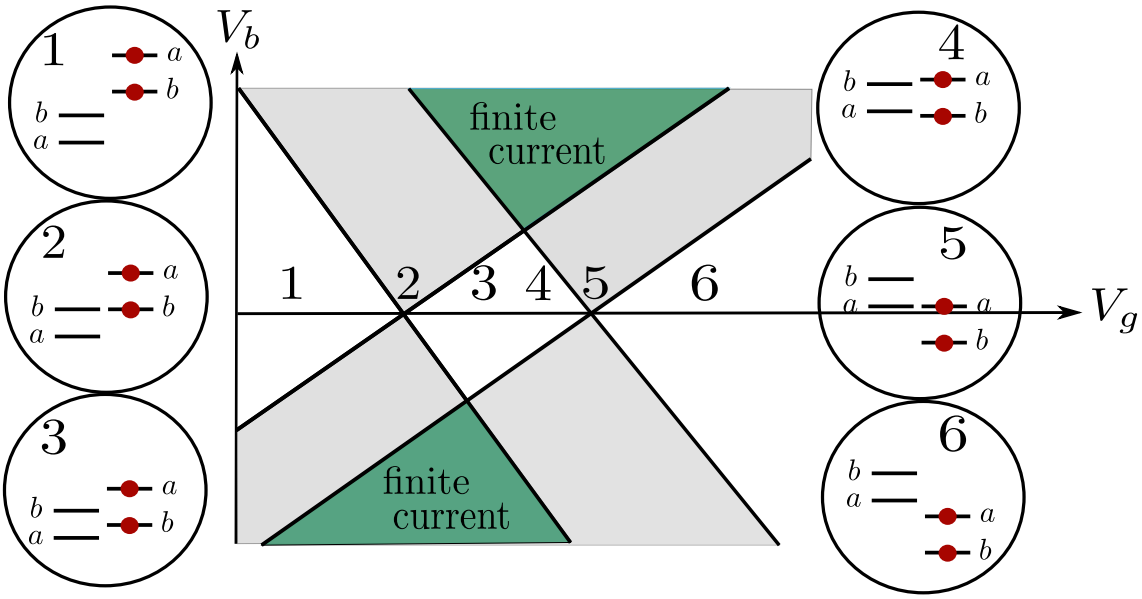

Figure 4.5.: Diagram showing regions with zero current (white and grey) and finite current (green) as a function of the gate voltage V_g and bias voltage V_b for the case with two molecular conformations a and b. In the white regions, sequential tunneling is blocked by Coulomb interaction for both conformations. In the grey regions it is only blocked for one conformation, but since the other is energetically more favourable, there is no current. In the green regions both conformations are conducting, and the current is finite. The circles contain schematics in energy space of the lowest occupied molecular orbital for each conformation in the neutral and in the charged state (we have set $N = 0$). Each circle corresponds to the region with the respective label. The border between regions 3 and 4 (not drawn here) corresponds to the neutral state of a having the same energy as the charged state of b; the precise border will be calculated and shown later.

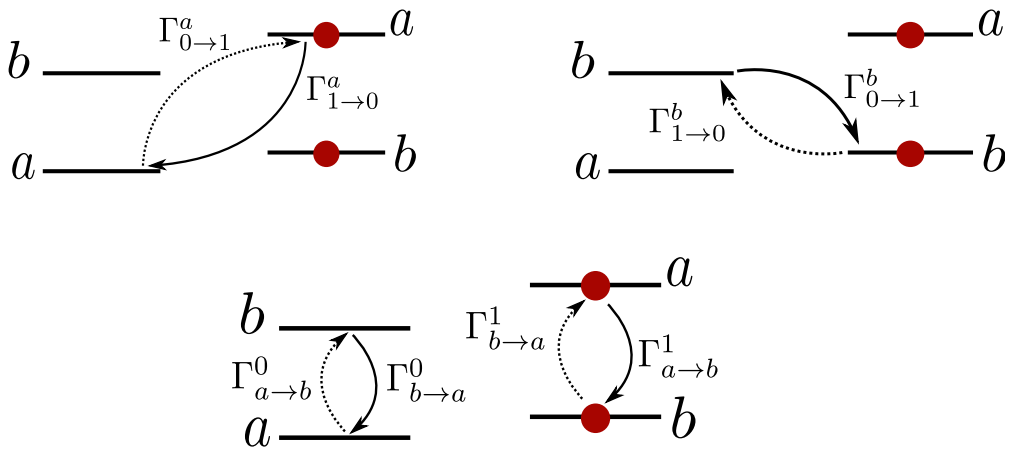

Figure 4.6.: Schematic of the allowed direct transition rates between the different states. A circle on the line denotes a charged state, a line without a circle denotes a neutral state.

In addition, we also include thermally-induced transitions between the two conformations if they are in the same charge state. These rates are proportional to the Bose-Einstein distribution $n(\varepsilon) = (e^{\varepsilon/k_BT} - 1)^{-1}$:

$$\Gamma^N_{a\to b} = \gamma\, n(\varepsilon^b_N - \varepsilon^a_N) \tag{4.26}$$

$$\Gamma^N_{b\to a} = -\gamma\, n(\varepsilon^a_N - \varepsilon^b_N). \tag{4.27}$$

$$\Gamma^{N+1}_{a\to b} = -\gamma\, n(\varepsilon^b_{N+1} - \varepsilon^a_{N+1}) \tag{4.28}$$

$$\Gamma^{N+1}_{b\to a} = \gamma\, n(\varepsilon^a_{N+1} - \varepsilon^b_{N+1}). \tag{4.29}$$

In the above expressions we have already assumed that $\varepsilon^a_N < \varepsilon^b_N$ and $\varepsilon^b_{N+1} < \varepsilon^a_{N+1}$ for $N = 0$ in our case. We do not allow for direct transitions that include both a conformational and a charge state change. A schematic picture of the allowed transitions is shown in Fig. 4.6.

With all transition rates defined, we can set up the rate equations for the case with two

conformations:

$$\begin{cases} \dfrac{dP_N^a(t)}{dt} = \Gamma^a_{N+1\to N} P^a_{N+1}(t) - \Gamma^a_{N\to N+1} P^a_N(t) + \Gamma^N_{b\to a} P^b_N(t) - \Gamma^N_{a\to b} P^a_N(t), \\ \dfrac{dP_N^b(t)}{dt} = \Gamma^b_{N+1\to N} P^b_{N+1}(t) - \Gamma^b_{N\to N+1} P^b_N(t) + \Gamma^N_{a\to b} P^a_N(t) - \Gamma^N_{b\to a} P^b_N(t), \\ \dfrac{dP_{N+1}^a(t)}{dt} = \Gamma^a_{N\to N+1} P^a_N(t) - \Gamma^a_{N+1\to N} P^a_{N+1}(t) + \Gamma^{N+1}_{b\to a} P^b_N(t) - \Gamma^{N+1}_{a\to b} P^a_N(t), \\ \dfrac{dP_{N+1}^b(t)}{dt} = \Gamma^b_{N\to N+1} P^b_N(t) - \Gamma^b_{N+1\to N} P^B_{N+1}(t) + \Gamma^{N+1}_{a\to b} P^a_N(t) - \Gamma^{N+1}_{b\to a} P^b_N(t), \\ P^a_N(t) + P^a_{N+1}(t) + P^b_N(t) + P^b_{N+1}(t) = 1. \end{cases} \tag{4.30}$$

Solving for the stationary probabilities P^a_N, P^b_N, P^a_{N+1}, and P^b_{N+1} and inserting the result into Eq. (4.23), we obtain the current flowing through the molecule.

4.3. Results

We now present the results obtained with the approach described in the previous section. Figure 4.7 shows the current calculated using Eq. 4.23. As can be seen by comparing with Fig. 4.1, it qualitatively resembles the experimental results, with a conductance gap at all gate voltages and two conducting regions determined by the Coulomb blockade lines of the two conformations. The slope of these lines (as well as the fact that in the experiment it appears to be different for all the four lines) and the precise size of the gap are not quantitatively the same as in the experimental results, which was to be expected since we have tried to set up the simplest model that would describe the appearance of the gap but have left out details such as the precise orbital structure of the molecule as well as the possibly different capacitive couplings of the two conformations to the substrate or the tip.

However, there are other qualitative features that our model captures. The blue line in Fig. 4.7 indicates the border between the two regions where the different conformations are stable and is the solution of the equation

$$P^0_a + P^1_a = P^0_b + P^1_b. \tag{4.31}$$

If the bias voltage is increased while keeping the gate voltage fixed, crossing this line would lead to a conformational switching of the molecule. If it is done faster than the conformational transition rate, the response of the molecule would be delayed and hysteresis could be observed. This is indeed the case, as shown in Fig. 4.8. The left panel contains the coercivity (which characterizes the extent of the hysteresis and will be defined below) of the molecule calculated within our model for the same set of parameters as in Fig. 4.7, while the right panel contains the experimental data. In our model, coercivity is determined by calculating the time-dependent probabilities $P^0_a(t)$ and $P^1_b(t)$ via Eq. (4.30) as the bias voltage V_b is ramped from $-1\,V$ to $1\,V$ and back at different speeds. An example for the ramping speed $500\,mV/s$ is shown in Fig. 4.9. The red dashed line corresponds

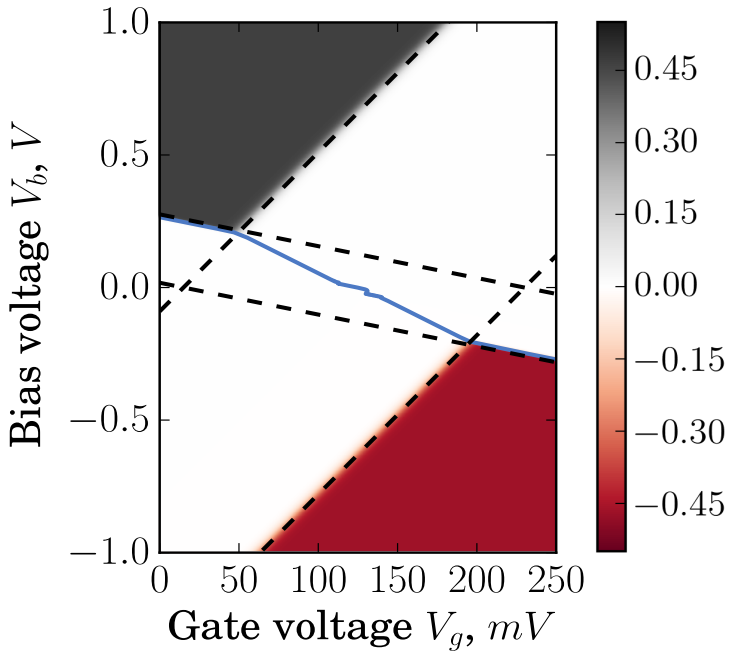

Figure 4.7.: Current (in nA) as a function of the gate voltage V_g and the bias voltage V_b. We have set $\varepsilon_0^a = 420\,meV$, $\varepsilon_1^a = 650\,meV$, $\varepsilon_0^b = 530\,meV$, $\varepsilon_1^b = 545\,meV$, $C_L = 10^{-15}\,F$, $C_R = 10^{-17}\,F$, $C_g = 1.9 \cdot 10^{-16}\,F$, $|t_L|^2/\hbar = 3 \cdot 10^9\,s^{-1}$, $|t_R|^2/\hbar = 10^{11}\,s^{-1}$, $\gamma = 10^7\,s^{-1}$, and $k_BT = 30K$, with the left electrode being the tip, and the right electrode being the substrate. The dashed lines are the Couloumb diamond lines for the two conformations, and the blue line is the border between the two regions where different conformations are stable (a is stable to the left of the line, while b is stable to the right of the line).

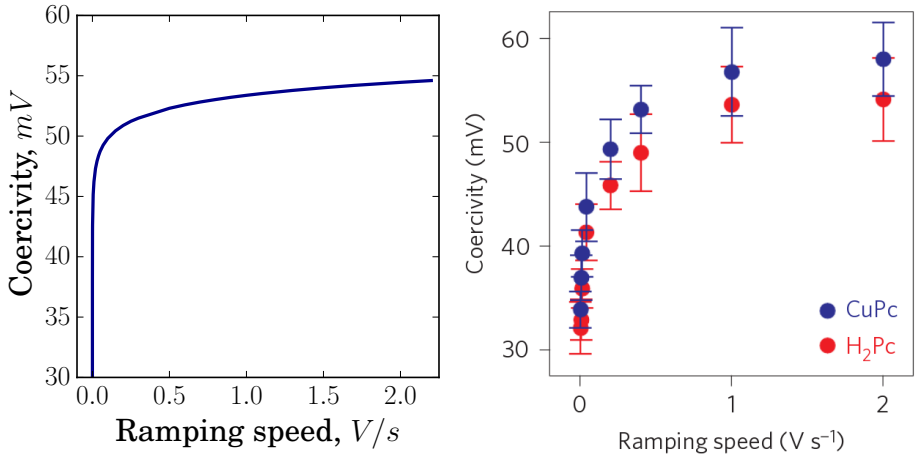

Figure 4.8.: Left panel: theoretical result for the coercivity as a function of the ramping speed. All parameters as in Fig. 4.7, $V_g = 150\,mV$. Right panel: experimental data for coercivity, taken from [Mart 15].

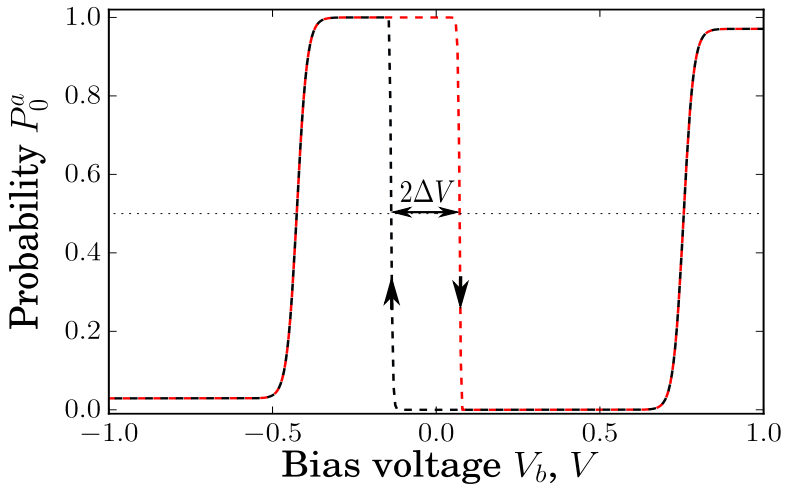

Figure 4.9.: Probability $P_0^a(t)$ as a function of the bias voltage V_b as the bias voltage is ramped from $-1\,V$ to $1\,V$ (red dashed line) and back (black dashed line) with the speed $500\,mV/s$. All the parameters are the same as in Fig. 4.8, and $V_g = 150\,mV$. As indicated with the arrows, coercivity ΔV is defined as half the distance between the two bias voltage points at which $P_0^a(t) = 1/2$ and that enclose the region of hysteresis.

to increasing bias voltage, and the black dashed line corresponds to decreasing bias voltage. The hysteresis happens around $V_b = 0$. The coercivity ΔV is defined as half of the difference in bias voltage between the two points closest to $V_b = 0$ (or at whichever bias voltage the hysteresis takes place) where P_a^0 is equal to $1/2$.

In experiment, the coercivity is measured based on the co-tunneling current. Since in the region of the conductance gap sequential tunneling is blocked, it is possible to observe the co-tunneling current. From the different I-V_b slopes for the different conformations it is possible to know which conformation the molecule is in and thus measure coercivity. As seen in Fig. 4.8, there is good qualitative agreement between our model and the measured data.

4.4. Conclusion

To conclude, we have been able to explain the qualitative behavior of a single-molecule transistor reported in Ref. [Mart 15] using a simple rate equation model by assuming that the molecule can exist in two different conformations whose lowest-energy states are differently charged. This assumption is backed by the experimental observation of two different molecular conformations using STM imaging. The molecule can also be viewed as a conformational switch whose state can be controlled with bias and gate voltages.

Our model captures the qualitative features of the current-voltage curves, such as the existence of a conduction gap for all gate voltages, as well as hysteretic behavior regarding conformational switching when the bias voltage is ramped back and forth.

The value of temperature used as an input in our model ($T = 30K$) to get the best resemblance with the experimental data is roughly an order of magnitude higher than that in the experiment ($T = 5K$). However, it might not be meaningful to compare these two values, since the value of the temperature is much smaller than the energy spread of the lowest unoccupied molecular orbital level in the experiment, while our model assumes that the opposite limit is true. This might partly account for the quantitative differences between the model and the experiment.

The slope of the Coulomb diamond lines obtained from our model is the same for both molecular conformations, which is not the case in the experiment. Since the slope is determined by the coupling between the molecule and the three gates, this could be ameliorated by setting the capacitances to be different for the different conformations.

The charge degeneracy point in the experiment does not lie at zero bias voltage, as can be seen if the Coulomb diamond lines are continued till they cross. This can be achieved in our model by raising the temperature, but an extension of the model that includes the shape of the molecular orbitals could lead to more satisfying results in this regard.

5. Conclusion

This thesis has dealt with three different mesoscopic systems that all involve some kind of switching process. We have seen that the control of a discrete property (spin state, charge state, conformation) of a system is possible by varying external parameters such as voltage. These systems can therefore serve as nanoscale switches. The study of switching processes at small size scales and their quantum mechanical treatment is necessitated by the miniaturization of electronics and by the importance of switching devices in electronics.

First, we investigated the possibility of switching the spin of a magnetic molecule on the surface of a topological insulator by applying an electric field to the surface. The spin-momentum locking of the surface spins of a topological insulator provides a way to control the spin of an electron by controlling its momentum. This means that instead of applying a magnetic field as is common for manipulating spins, it is possible to control magnetic degrees of freedom with electric fields.

We have found that while for a two-dimensional topological insulator with a one-dimensional edge a complete switching of the magnetic molecule is indeed possible, the situation is more complicated in the case of a three-dimensional topological insulator. Complete switching is only possible if the direction of the current is aligned with the magnetic anisotropy axis of the molecule and if the current density is in the optimal range—much larger than the temperature but much smaller than the scale set by the anisotropy energy. However, the net magnetization in the direction of the current even for an ensemble of randomly oriented molecules is always nonzero. Surprisingly, the effectiveness of the switching decreases as the current density is increased beyond the optimal range. This is explained by the fact that, once the current density exceeds the anisotropy scale considerably, transitions between all states, not just the ones with the highest spin projection, become easily accessible. We note that the current density needed to overcome thermal fluctuations is smaller if the chemical potential is close to the Dirac point (since the current density is measured against the Fermi wave vector). Another parameter in the model is the coupling strength between the molecule and the surface, which sets the timescale during which the molecule remains in the switched state. As a conservative estimate, we find the switching time to be on the order of 11^{-11} s, although it is likely to be much larger, given that the spin in high-spin molecules is usually surrounded by an organic shell, which decreases the coupling.

In Chapter 3, we looked at single-electron wave packet scattering in a quantum point contact under different kinds of time-dependent potentials, among them a step-like time-dependent potential that is switched on abruptly and can be used to measure the arrival time distribution of the wave packet. The scattering takes place in the one-dimensional chiral quantum Hall edge channels, since the problem is motivated by electron quantum optics experiments where quantum Hall edges are used as ballistic wave guides. Our main goal was to find a general quantum mechanical expression for the transmitted charge

through the quantum point contact and to provide a formalism to describe a recent electron tomography experiment.

We treated the problem by introducing a modified Wigner function which absorbs the time-dependence of the potential. This led to an expression for the transmitted charge that resembles the semiclassical result, with the quantum analog of the classical probability density being the modified Wigner function. Remarkably, we found that the semiclassical result is exact for the case of a linear voltage ramp, meaning that the linear classical electron tomography protocol realized by Fletcher *et al.* is also valid in the quantum case. We have also shown that by superimposing an additional potential on top of a linear one, the modified Wigner function can be obtained as the outcome of a tomography experiment. This can be used to deterime the coherence of electron sources.

In Chapter 4, we set up and solved a rate equation model for a single-molecule transistor tunnel-coupled to two leads (a substrate and an STM tip). In contrast to the expected Coulomb diamond picture in the bias voltage-gate voltage diagram of a single-electron transistor, the experimentally measured conductance of the particular phthalocyanine molecular transistor is zero for all gate voltages. To explain this result, we extended the rate equation model for a single-electron transistor to include the possibility for the molecule to be in two different conformations.

We calculated the current as a function of the gate and bias voltages, as well as the coercivity of the conformational switching process. The results were in qualitative agreement with the experimental data. To reach a quantitative agreement, our simple model should be extended to include different capacitive couplings to the electrodes for the different conformations and the particular shape of the molecular orbitals.

Appendix

A. Appendix to Chapter 2

A.1. Molecular magnets with half-integer spin

In the case of a molecular magnet with half-integer spin S the states $|1/2\rangle$ and $|-1/2\rangle$ are degenerate, which means that transitions between these states cannot be described by means of a rate equation, but that they need to be described with a master equation for the (reduced) density matrix

$$\rho = \begin{pmatrix} \rho_{1/2,1/2} & \rho_{1/2,-1/2} \\ \rho_{1/2,-1/2} & \rho_{-1/2,-1/2} \end{pmatrix}. \tag{A.1}$$

The diagonal elements $\rho_{s,s} = P_s$ are the probabilities to find the molecule in spin state $|s\rangle$, $s = \pm 1/2$; the off-diagonal elements describe coherences beween these two spin states.

To allow for a unified treatment of a molecular magnet coupled to the edge of a two-dimensional TI and a molecular magnet at the surface of a three-dimensional TI, we write matrix elements of the exchange Hamiltonian (2.1) for the two-dimensional case as

$$\langle \varphi', s' | H_{\rm ex} | \varphi, s \rangle = \frac{1}{2} J v \hbar m_{s',s}(\varphi', \varphi), \tag{A.2}$$

where we use the propagation angle $\varphi = 0$ for a right-moving electron (labeled with $\tau = +1$ in Sec. 2.2) and $\varphi = \pi$ for a left-moving electron (labeled with $\tau = -1$). Matrix elements of the exchange Hamiltonian (2.28) for the three-dimensional case are written

$$\langle \varphi', s' | H_{\rm ex} | \varphi, s \rangle = \frac{J v \hbar}{k_{\rm F}} m_{s',s}(\varphi', \varphi). \tag{A.3}$$

The rates $\Gamma_{s',s}$, see Eqs. (2.20) and (2.31), are then expressed as

$$\Gamma_{s',s} = J^2 \int \frac{d\varphi}{2\pi} \frac{d\varphi'}{2\pi} |m_{s',s}(\varphi', \varphi)|^2 g[I(\cos\varphi' - \cos\varphi)/2 + D(s^2 - s'^2)], \tag{A.4}$$

where the double integration $\int (d\varphi/2\pi)(d\varphi'/2\pi)$ should be replaced by a double sum $(1/4)\sum_{\varphi,\varphi'=0,\pi}$ for the case of a two-dimensional TI. The explicit expressions for the $m(\varphi', \varphi)$ read

$$\begin{aligned} \hbar m(\varphi', \varphi) = {} & 2(S_z \cos\theta - S_x \sin\theta)\cos\varphi_+ \\ & + (S_x \cos\theta + S_z \sin\theta)(\cos\phi \sin\varphi_+ + i \sin\phi \sin\varphi_-) \\ & + i S_y (\cos\phi \sin\varphi_- + i \sin\phi \sin\varphi_+), \end{aligned} \tag{A.5}$$

where $\varphi_\pm = (\varphi' \pm \varphi)/2$, see the text below Eq. (2.30).

Because of the large energy differences between spin states with different values of $|s|$ and the lack of direct transitions between the degenerate spin states $|s\rangle$ and $|-s\rangle$ for $|s| > 1/2$, the rates (A.4) are sufficient to calculate the (rate of change of the) probabilities P_s that the molecule is in spin state $|s\rangle$ for $|s| > 1/2$, see Eq. (2.8). On the other hand, for the degenerate spin states $|1/2\rangle$ and $|-1/2\rangle$ we must use the full density matrix ρ, see Eq. (A.1). The equation of motion for this density matrix has the well-known Lindblad form [Koss 72, Lind 76]

$$\begin{aligned}\frac{d\rho}{dt} &= -\frac{i}{\hbar}(\overline{H_{\rm ex}}\rho - \rho\overline{H_{\rm ex}}) \\ &+ \sum_{\pm}\left[\Gamma_{\pm 1/2,\pm 3/2}\Pi_{\pm 1/2}P_{\pm 3/2} - \frac{1}{2}\Gamma_{\pm 3/2,\pm 1/2}\left(\Pi_{\pm 1/2}\rho + \rho\Pi_{\pm 1/2}\right)\right] \\ &+ J^2\int\frac{d\varphi}{2\pi}\frac{d\varphi'}{2\pi}g[I(\cos\varphi' - \cos\varphi)/2] \\ &\times\left\{m(\varphi',\varphi)\rho m(\varphi',\varphi)^\dagger - \frac{1}{2}\left[m(\varphi',\varphi)^\dagger m(\varphi',\varphi)\rho + \rho m(\varphi',\varphi)^\dagger m(\varphi',\varphi)\right]\right\},\end{aligned} \tag{A.6}$$

where the projection matrices $\Pi_{1/2}$, and $\Pi_{-1/2}$ are defined as

$$\Pi_{1/2} = \begin{pmatrix} 1 & 0 \\ 0 & 0 \end{pmatrix}, \quad \Pi_{-1/2} = \begin{pmatrix} 0 & 0 \\ 0 & 1 \end{pmatrix}. \tag{A.7}$$

One verifies that the Lindblad equation (A.6) simplifies to the standard rate equation (2.8) if the density matrix ρ is a diagonal matrix, $\rho = \mathrm{diag}\,(P_{1/2}, P_{-1/2})$.

The first term in Eq. (A.6) contains the expectation value of the exchange Hamiltonian projected onto the spin states $|\pm 1/2\rangle$. It acts as an effective magnetic field driving coherent transitions between the states $|1/2\rangle$ and $|-1/2\rangle$. This term plays no role for states $|s\rangle$ with $|s| > 1/2$ because it is much smaller than the anisotropy field if the exchange coupling is weak, $|J| \ll 1$. However, for transitions between the states $|1/2\rangle$ and $|-1/2\rangle$ there is no anisotropy field, and the exchange field competes with the similarly small scattering-induced transitions between the states $|1/2\rangle$ and $|-1/2\rangle$. With the same notation as above we have

$$\overline{H_{\rm ex}} = \frac{JI\hbar}{2}\int\frac{d\varphi}{2\pi}m(\varphi,\varphi)\cos\phi, \tag{A.8}$$

where, for a molecule coupled to the edge of a two-dimensional topological insulator, the integration $\int(d\varphi/2\pi)$ should be replaced by a summation $(1/2)\sum_{\varphi=0,\pi}$. Performing the angular integration gives

$$\overline{H_{\rm ex}} = \frac{JI\hbar}{8}\begin{pmatrix} 2\cos\theta & -(2S+1)\sin\theta \\ -(2S+1)\sin\theta & -2\cos\theta \end{pmatrix}, \tag{A.9}$$

which is indeed what one expects for an exchange field in the z direction, recalling that the spin states $|s\rangle$ are defined with respect to the anisotropy axis $\mathbf{e} = \cos\theta\mathbf{e}_z + \sin\theta\cos\phi\mathbf{e}_x + \sin\theta\sin\phi\mathbf{e}_y$.

A solution of the Lindblad equation proceeds by parameterizing

$$\rho = \frac{1}{2}\rho_0\tau_0 + \frac{1}{2}\sum_{j=x,y,z}\rho_j\tau_j, \tag{A.10}$$

where τ_0 is the 2×2 identity matrix and the τ_j are the Pauli matrices in the space spanned by $|1/2\rangle$ and $|-1/2\rangle$. We give the equation of motion for ρ for the intermediate and high current regimes, in which we may approximate $g[I(\cos\varphi'-\cos\varphi)/2] \approx I(\cos\varphi-\cos\varphi')/2$ if $\cos\varphi > \cos\varphi'$ and $g[I(\cos\varphi'-\cos\varphi)/2] \approx 0$ otherwise (including the case $\cos\varphi = \cos\varphi'$).

In the two-dimensional case there is a contribution from $\varphi = 0$, $\varphi = \pi$ only. The equations of motion read

$$\begin{aligned}
\frac{d\rho_0}{dt} &= \sum_{\pm}\left[\Gamma_{\pm 1/2,\pm 3/2}P_{\pm 3/2} - \frac{1}{2}\Gamma_{\pm 3/2,\pm 1/2}(\rho_0 \pm \rho_z)\right], \\
\frac{d\rho_x}{dt} &= -\frac{JI}{8}\rho_y\cos\theta + \frac{J^2I}{8}\Big\{ -\rho_x[4\sin^2\theta + (2S+1)^2] \\
&\quad + 2(\rho_z\cos\theta - 2\rho_0)(2S+1)\sin\theta\Big\} - \frac{1}{2}\rho_x\sum_{\pm}\Gamma_{\pm 3/2,\pm 1/2}, \\
\frac{d\rho_y}{dt} &= \frac{JI}{16}\left[2\rho_x\cos\theta + \rho_z(2S+1)\sin\theta\right] - \frac{J^2I}{8}\rho_y\left[4\sin^2\theta + (2S+1)^2\cos^2\theta\right] \\
&\quad - \frac{1}{2}\rho_y\sum_{\pm}\Gamma_{\pm 3/2,\pm 1/2}, \\
\frac{d\rho_z}{dt} &= -\frac{JI}{16}(2S+1)\rho_y\sin\theta + \frac{J^2I}{8}(2S+1)\Big\{(2S+1)[2\rho_0\cos\theta - \rho_z(\cos^2\theta+1)] \\
&\quad + 2\rho_x\sin\theta\cos\theta\Big\} \\
&\quad + \sum_{\pm}\left[\pm\Gamma_{\pm 1/2,\pm 3/2}P_{\pm 3/2} - \frac{1}{2}\Gamma_{\pm 3/2,\pm 1/2}(\rho_z \pm \rho_0)\right],
\end{aligned} \tag{A.11}$$

In the three-dimensional case the equations of motion are

$$\begin{aligned}
\frac{d\rho_0}{dt} &= \sum_{\pm}\left[\Gamma_{\pm 1/2,\pm 3/2}P_{\pm 3/2} - \frac{1}{2}\Gamma_{\pm 3/2,\pm 1/2}(\rho_0 \pm \rho_z)\right], \\
\frac{d\rho_x}{dt} &= -\frac{JI}{8}\rho_y\cos\theta - \frac{J^2I}{3\pi^2}\left\{\rho_x\left[4+\sin^2\theta+2(2S+1)^2\right] + 4\sin\theta\cos\theta\rho_z\right\} \\
&\quad - \frac{J^2I}{4}\rho_0(2S+1)\sin\theta - \frac{1}{2}\rho_x\sum_{\pm}\Gamma_{\pm 3/2,\pm 1/2}, \\
\frac{d\rho_y}{dt} &= \frac{JI}{16}\left[2\rho_x\cos\theta + \rho_z(2S+1)\sin\theta\right] \\
&\quad - \frac{J^2I}{3\pi^2}\rho_y\left[4+4\sin^2\theta+(2S+1)^2(1+\cos^2\theta)\right] - \frac{1}{2}\rho_y\sum_{\pm}\Gamma_{\pm 3/2,\pm 1/2}, \\
\frac{d\rho_z}{dt} &= -\frac{JI}{16}(2S+1)\rho_y\sin\theta \\
&\quad + \frac{J^2I}{3\pi^2}(2S+1)\left[2\rho_x\sin\theta\cos\theta - \rho_z(2S+1)(4-\sin^2\theta)\right] \\
&\quad + \frac{J^2I}{8}(2S+1)^2\rho_0\cos\theta \\
&\quad + \sum_{\pm}\left[\pm\Gamma_{\pm 1/2,\pm 3/2}P_{\pm 3/2} - \frac{1}{2}\Gamma_{\pm 3/2,\pm 1/2}(\rho_z \pm \rho_0)\right].
\end{aligned} \tag{A.12}$$

In the intermediate-current regime we may set

$$\Gamma_{\pm 3/2,\pm 1/2} \approx \frac{J^2D}{2}(2S-1)(2S+3), \tag{A.13}$$

see Eqs. (2.20) and (2.33). For the high-current regime we may approximate $\Gamma_{\pm 3/2,\pm 1/2}$ by Eqs. (2.24) and (2.38) for the two-dimensional and three-dimensional cases, respectively.

When searching for a stationary solution, the contributions from transitions to/from the spin states $|\pm 3/2\rangle$ vanish in the equations of motion for ρ_0 and ρ_z because of detailed balance. They remain, however, in the equations of motion for ρ_x and ρ_y. Once the ratio $P_{1/2}/P_{-1/2}$ has been determined from the stationary solution of the Lindblad equations (A.11) or (A.12), the remaining probabilities P_s for $|s| > 1/2$ can be found from detailed balance,

$$P_{|s|} = \frac{\Gamma_{|s|,|s|-1}P_{|s|-1}}{\Gamma_{|s|-1,|s|}}, \quad s = \pm 3/2, \ldots, \pm S, \tag{A.14}$$

and from the normalization condition $\sum_s P_s = 1$.

We now report expressions for the ratio $P_{1/2}/P_{-1/2}$ for the intermediate and high current regimes $k_BT \ll \hbar I \ll \hbar D(2S-1)$ and $I \gg D(2S-1)$ for a spin coupled to the edge of a two-dimensinal TI and to the surface of a three-dimensional TI. The expressions for the intermediate-current regime are simplified using the inequalities $I \ll D(2S-1)$ and $J \ll 1$, but we make no assumptions regarding the relative magnitude of these two quantities. (Note that the intermediate current regime does not exist for $S = 1/2$.) The expressions for the high-current limit are simplified using the inequality $J \ll 1$.

In the intermediate-current regime we find for the case of a molecular magnet coupled to the edge of a two-dimensional TI

$$\frac{P_{1/2}}{P_{-1/2}} = \frac{G_+(\theta)}{G_-(\theta)}, \tag{A.15}$$

with

$$G_\pm(\theta) = (1 \pm \cos\theta)^2 + \frac{I \sin^2\theta}{16DJ^2(2S-1)(2S+3)}. \tag{A.16}$$

This result agrees with what one obtains from naive application of the rate equations if $I \ll J^2D(2S-1)$, but differs otherwise because of the effect of the current-induced exchange field (A.9). Note that $G_-(\theta) = G_+(\pi-\theta)$. The resulting steady-state probability distribution is

$$\begin{aligned} P_S &= 1 - P_{-S} \\ &= \frac{G_+(\theta)(1+\cos\theta)^{4S-2}}{G_+(\theta)(1+\cos\theta)^{4S-2} + G_-(\theta)(1-\cos\theta)^{4S-2}}. \end{aligned} \tag{A.17}$$

The current-induced switching rate from $|-S\rangle$ to $|S\rangle$ can be calculated as the transition rate from $|-1/2\rangle$ to $|1/2\rangle$ starting with the initial condition

$$\begin{aligned} \rho(0) &= \frac{(1+\cos\theta)^{S-1/2}}{2^{S-1/2}} \Pi_{-1/2} \\ &\quad \times e^{2\pi\hbar(S-1/2)(I-D(S+1/2))/k_\mathrm{B}T}, \end{aligned}$$

which is the reduced density matrix after current-induced equilibration of all states with $s < 0$, including the state $|-1/2\rangle$, but without including transitions from $|-1/2\rangle$ to $|1/2\rangle$. Within a time $\sim 2/J^2D(2S-1)(2S+3)$, which is short in comparison to the time required to transition from to $|-1/2\rangle$ to $|1/2\rangle$, a quasi-steady state is reached for the reduced density matrix ρ, in which the off-diagonal component ρ_y becomes nonzero,

$$\rho_y \approx \frac{\rho_z I(2S+1)}{8JD(2S-1)(2S+3)}.$$

The current-induced switching rate $\Gamma_\mathrm{switch}(I)$ is then found as the rate of change of $P_{1/2}$ in this quasi-steady state, which gives

$$\begin{aligned} \Gamma_\mathrm{switch}(I) &= \frac{J^2 I(2S+1)^2}{2^{S+7/2}} G_+(\theta)(1+\cos\theta)^{S-1/2} \\ &\quad \times e^{2\pi\hbar(S-1/2)(I-D(S+1/2))/k_\mathrm{B}T}, \end{aligned} \tag{A.18}$$

where $G_+(\theta)$ was defined in Eq. (A.16). The switching rate for the opposite process is given the same expression, but with the replacement $\theta \to \pi - \theta$.

For the high-current limit and a two-dimensional TI we find $P_{1/2}/P_{-1/2} = G_+(\theta)/G_-(\theta)$ with the function $G_\pm(\theta)$ defined as

$$G_\pm(\theta) = \frac{1 \pm \cos\theta}{2} + \frac{3(2S-1)(2S+3)}{32} \sin^2\theta, \tag{A.19}$$

which is different from the result one obtains from naive application of the rate equations. For $S = 1/2$ the ratio $P_{1/2}/P_{-1/2}$ is consistent with a spin polarized in the z direction. The resulting probability distribution P_s reads

$$\begin{aligned} P_{\pm|s|} &= \frac{4\cos\theta G_{\pm}(\theta)}{G_{+}(\theta)(1+\cos\theta)^{2S-1} + G_{-}(\theta)(1-\cos\theta)^{2S-1}} \\ &\quad \times \frac{(1\pm\cos\theta)^{2(|s|+S-1)}(1\mp\cos\theta)^{2(S-|s|)}}{(1+\cos\theta)^{2S+1} - (1-\cos\theta)^{2S+1}}. \end{aligned} \tag{A.20}$$

Equation (2.16) of the main text is a good order-of-magnitude estimate for the rate $\Gamma_{\text{switch}}(I)$ at which this steady-state distribution is approached.

For a molecule on the surface of a three-dimensional TI with an applied current in the intermediate-current regime $k_{\text{B}}T \ll \hbar I \ll \hbar D(2S-1)$ the stationary solution of the Lindblad equation (A.12) gives the ratio $P_{1/2}/P_{-1/2} = G_{+}(\theta)/G_{-}(\theta)$ with

$$G_{\pm}(\theta) = F_{\pm}(\theta) + \frac{\pi I \sin^2\theta}{32DJ^2(2S-1)(2S+3)}, \tag{A.21}$$

where the function $F_{\pm}(\theta)$ was defined in Eq. (2.39) of the main text. This expression simplifies to the ratio $P_{1/2}/P_{-1/2} = F_{+}(\theta)/F_{-}(\theta)$ one obtains by considering rates only in the limit $I \ll DJ^2(2S-1)$. The corresonding steady-state distribution reads

$$\begin{aligned} P_S &= 1 - P_{-S} \\ &= \frac{G_{+}(\theta)F_{+}(\theta)^{4S-2}}{G_{+}(\theta)F_{+}(\theta)^{4S-2} + G_{-}(\theta)F_{-}(\theta)^{4S-2}}. \end{aligned} \tag{A.22}$$

The switching rate from $|-S\rangle$ to $|S\rangle$ is calculated in the same way as for the case of a two-dimensional TI, and one finds

$$\begin{aligned} \Gamma_{\text{switch}}(I) &= \frac{J^2 I(2S+1)^2 G_{+}(\theta)}{8\pi} \\ &\quad \times \left(\frac{2(1+\cos\theta)^2 k_{\text{B}}T}{\pi^2\hbar I}\right)^{S-1/2} \\ &\quad \times e^{2\pi\hbar(S-1/2)(I-D(S+1/2))/k_{\text{B}}T}. \end{aligned} \tag{A.23}$$

The switching rate for the inverse transition is again given by the replacement $\theta \to \pi - \theta$.

Finally, for the high-current regime in three dimensions we find that the stationary solution of the Lindblad equation (A.12) has $P_{1/2}/P_{-1/2} = G_{+}(\theta)/G_{-}(\theta)$ with

$$\begin{aligned} G_{\pm}(\theta) &= \frac{1}{2} \pm \frac{3\pi^2}{64}\cos\theta \\ &\quad + \frac{(2S-1)(2S+3)}{64}(8-\sin^2\theta)\sin^2\theta. \end{aligned} \tag{A.24}$$

The corresponding steady-state distribution reads

$$\begin{aligned} P_{\pm|s|} &= \frac{F_{+}(\theta) - F_{-}(\theta)}{G_{+}(\theta)F_{+}(\theta)^{S-1/2} + G_{-}(\theta)F_{-}(\theta)^{S-1/2}} \\ &\quad \times \frac{G_{\pm}(\theta)F_{\pm}(\theta)^{|s|+S-1}F_{\mp}(\theta)^{S-|s|}}{F_{+}(\theta)^{S+1/2} - F_{-}(\theta)^{S+1/2}}. \end{aligned} \tag{A.25}$$

This distribution is approached at the rate given by Eq. (2.16) of the main text.

If the magnetic anisotropy axis is aligned with the current direction, the rate equation approach can be used throughout. In this case the transition rates $\Gamma_{1/2,-1/2}$ and $\Gamma_{-1/2,1/2}$ for the intermediate and high-current regimes read

$$\Gamma_{\pm 1/2,\mp 1/2} = J^2 I (S+1/2)^2 \left[\frac{8}{3\pi^2} \pm \frac{1}{4} \right]. \tag{A.26}$$

In the intermediate-current regime, the steady-state spin polarization of the molecule is complete; The probability P_{-S} vanishes $\propto (k_{\rm B}T/\hbar I)^{2S-1}$ if S is half integer, whereas all other probabilities are exponentially small in $\hbar D(2S-1)/k_{\rm B}T$. The switching rate out of the state $|-S\rangle$ is, in the intermediate-current regime,

$$\begin{aligned} \Gamma_{\rm switch}(I) &= \frac{J^2 \hbar I (S+1/2)^2 (32+3\pi^2)}{12\pi^2\hbar} \left(\frac{8k_{\rm B}T}{\pi^2 \hbar I} \right)^{S-1/2} \\ &\quad \times e^{2\pi\hbar(S-1/2)(I-D(S+1/2)/k_{\rm B}T}. \end{aligned} \tag{A.27}$$

In the high-current regime the order-of-magnitude estimate (2.16) for the switching rate also applies to the half-integer spin case.

Bibliography

[Alha 00] Y. Alhassid, *"The statistical theory of quantum dots"*, Rev. Mod. Phys. **72**, 895–968, Oct 2000.

[Ando 08] K. Ando, S. Takahashi, K. Harii, K. Sasage, J. Ieda, S. Maekawa, and E. Saitoh, *"Electric Manipulation of Spin Relaxation Using the Spin Hall Effect"*, Phys. Rev. Lett. **101**, 036601, Jul 2008.

[Arra 05] L. Arrachea, *"Green-function approach to transport phenomena in quantum pumps"*, Phys. Rev. B **72**, 125349, Sep 2005.

[Bade 10] S. Bader and S. Parkin, *"Spintronics"*, Annual Review of Condensed Matter Physics **1**, 71–88, Apr 2010.

[Baib 88] M. N. Baibich, J. M. Broto, A. Fert, F. N. Van Dau, F. Petroff, P. Etienne, G. Creuzet, A. Friederich, and J. Chazelas, *"Giant Magnetoresistance of (001)Fe/(001)Cr Magnetic Superlattices"*, Phys. Rev. Lett. **61**, 2472–2475, Nov 1988.

[Baue 18] C. Bauerle, C. Glattli, T. Meunier, F. Portier, P. Roche, P. Roulleau, S. Takada, and X. Waintal, *"Coherent control of single electrons: a review of current progress"*, Reports on Progress in Physics, Jan 2018.

[Been 91] C. W. J. Beenakker, *"Theory of Coulomb-blockade oscillations in the conductance of a quantum dot"*, Phys. Rev. B **44**, 1646–1656, Jul 1991.

[Been 97] C. W. J. Beenakker, *"Random-matrix theory of quantum transport"*, Rev. Mod. Phys. **69**, 731–808, Jul 1997.

[Berg 96] L. Berger, *"Emission of spin waves by a magnetic multilayer traversed by a current"*, Phys. Rev. B **54**, 9353–9358, Oct 1996.

[Bern 06] B. A. Bernevig, T. L. Hughes, and S.-C. Zhang, *"Quantum Spin Hall Effect and Topological Phase Transition in HgTe Quantum Wells"*, Science **314**, 1757–1761, Dec 2006.

[Bina 89] G. Binasch, P. Grünberg, F. Saurenbach, and W. Zinn, *"Enhanced magnetoresistance in layered magnetic structures with antiferromagnetic interlayer exchange"*, Phys. Rev. B **39**, 4828–4830, Mar 1989.

[Blum 07] M. D. Blumenthal, B. Kaestner, L. Li, S. Giblin, T. J. B. M. Janssen, M. Pepper, D. Anderson, G. Jones, and D. A. Ritchie, *"Gigahertz quantized charge pumping"*, Nature Physics **3**, 343–347, May 2007.

[Bock 97] M. Bockrath, D. H. Cobden, P. L. McEuen, N. G. Chopra, A. Zettl, A. Thess, and R. E. Smalley, *"Single-Electron Transport in Ropes of Carbon Nanotubes"*, Science **275**, 1922–1925, Mar 1997.

[Bocq 12] E. Bocquillon, F. D. Parmentier, C. Grenier, J.-M. Berroir, P. Degiovanni, D. C. Glattli, B. Plaçais, A. Cavanna, Y. Jin, and G. Fève, *"Electron Quantum Optics: Partitioning Electrons One by One"*, Phys. Rev. Lett. **108**, 196803, May 2012.

[Bocq 14] E. Bocquillon, V. Freulon, F. D. Parmentier, J.-M. Berroir, B. Plaçais, C. Wahl, J. Rech, T. Jonckheere, T. Martin, C. Grenier, D. Ferraro, P. Degiovanni, and G. Fève, *"Electron quantum optics in ballistic chiral conductors"*, Annalen der Physik **526**, 1–30, Jan 2014.

[Boga 08] L. Bogani and W. Wernsdorfer, *"Molecular spintronics using single-molecule magnets"*, Nature Materials **7**, 179–186, Mar 2008.

[Brai 05] S. Braig and P. W. Brouwer, *"Rate equations for Coulomb blockade with ferromagnetic leads"*, Phys. Rev. B **71**, 195324, May 2005.

[Brau 04] M. Braun, J. König, and J. Martinek, *"Theory of transport through quantum-dot spin valves in the weak-coupling regime"*, Phys. Rev. B **70**, 195345, Nov 2004.

[Brou 95] P. W. Brouwer, *"Generalized circular ensemble of scattering matrices for a chaotic cavity with nonideal leads"*, Phys. Rev. B **51**, 16878–16884, Jun 1995.

[Brou 98] P. W. Brouwer, *"Scattering approach to parametric pumping"*, Phys. Rev. B **58**, R10135–R10138, Oct 1998.

[Brun 12] C. Brüne, A. Roth, H. Buhmann, E. M. Hankiewicz, L. W. Molenkamp, J. Maciejko, X.-L. Qi, and S.-C. Zhang, *"Spin polarization of the quantum spin Hall edge states"*, Nature Physics **8**, 486–491, Jun 2012.

[Butt 90] M. Büttiker, *"Scattering theory of thermal and excess noise in open conductors"*, Phys. Rev. Lett. **65**, 2901–2904, Dec 1990.

[Butt 92] M. Büttiker, *"Scattering theory of current and intensity noise correlations in conductors and wave guides"*, Phys. Rev. B **46**, 12485–12507, Nov 1992.

[Cand 11] A. Candini, S. Klyatskaya, M. Ruben, W. Wernsdorfer, and M. Affronte, *"Graphene Spintronic Devices with Molecular Nanomagnets"*, Nano Letters **11**, 2634–2639, Jul 2011.

[Chen 14] J. Chen, M. B. A. Jalil, and S. G. Tan, *"Current-Induced Spin Torque on Magnetization Textures Coupled to the Topological Surface States of Three-Dimensional Topological Insulators"*, Journal of the Physical Society of Japan **83**, 064710, May 2014.

[Chor 12] S. J. Chorley, J. Frake, C. G. Smith, G. A. C. Jones, and M. R. Buitelaar, *"Quantized charge pumping through a carbon nanotube double quantum dot"*, Applied Physics Letters **100**, 143104, Apr 2012.

[Chou 06] H. T. Chou, D. Goldhaber-Gordon, S. Schmult, M. J. Manfra, A. M. Sergent, and R. J. Molnar, *"Single-electron transistors in GaN /AlGaN heterostructures"*, Applied Physics Letters **89**, 033104, Jul 2006.

[Chri 00] G. Christou, D. Gatteschi, D. N. Hendrickson, and R. Sessoli, *"Single-Molecule Magnets"*, MRS Bulletin **25**, 66–71, Jan 2000.

[Clel 13] A. N. Cleland. *Foundations of Nanomechanics: From Solid-State Theory to Device Applications (Advanced Texts in Physics)*. Springer (2013).

[Conn 13] M. R. Connolly, K. L. Chiu, S. P. Giblin, M. Kataoka, J. D. Fletcher, C. Chua, J. P. Griffiths, G. A. C. Jones, V. I. Fal'Ko, C. G. Smith, and T. J. B. M. Janssen, *"Gigahertz quantized charge pumping in graphene quantum dots"*, Nature Nanotechnology **8**, 417–420, Jun 2013.

[Dean 92] S. R. Deans. *The Radon Transform and Some of Its Applications*. Krieger Pub Co (1992).

[Demk 12] R. Demkowicz-Dobrzański, J. Kołodyński, and M. Guţă, *"The elusive Heisenberg limit in quantum-enhanced metrology"*, Nature Communications **3**, 1063, Sep 2012.

[dHol 15] S. d'Hollosy, M. Jung, A. Baumgartner, V. A. Guzenko, M. H. Madsen, J. Nygård, and C. Schönenberger, *"Gigahertz Quantized Charge Pumping in Bottom-Gate-Defined InAs Nanowire Quantum Dots"*, Nano Letters **15**, 4585–4590, Jul 2015.

[Dubo 13] J. Dubois, T. Jullien, C. Grenier, P. Degiovanni, P. Roulleau, and D. C. Glattli, *"Integer and fractional charge Lorentzian voltage pulses analyzed in the framework of photon-assisted shot noise"*, Phys. Rev. B **88**, 085301, Aug 2013.

[Emor 13] S. Emori, U. Bauer, S.-M. Ahn, E. Martinez, and G. S. D. Beach, *"Current-driven dynamics of chiral ferromagnetic domain walls"*, Nature Materials **12**, 611–616, Jul 2013.

[Fan 13] X. Fan, J. Wu, Y. Chen, M. J. Jerry, H. Zhang, and J. Q. Xiao, *"Observation of the nonlocal spin-orbital effective field"*, Nature Communications **4**, 1799, Apr 2013.

[Fan 14] Y. Fan, P. Upadhyaya, X. Kou, M. Lang, S. Takei, Z. Wang, J. Tang, L. He, L.-T. Chang, M. Montazeri, G. Yu, W. Jiang, T. Nie, R. N. Schwartz, Y. Tserkovnyak, and K. L. Wang, *"Magnetization switching through giant spin-orbit torque in a magnetically doped topological insulator heterostructure"*, Nature Materials **13**, 699–704, Jul 2014.

[Ferr 13] D. Ferraro, A. Feller, A. Ghibaudo, E. Thibierge, E. Bocquillon, G. Fève, C. Grenier, and P. Degiovanni, *"Wigner function approach to single electron coherence in quantum Hall edge channels"*, Phys. Rev. B **88**, 205303, Nov 2013.

[Fert 87] H. A. Fertig and B. I. Halperin, *"Transmission coefficient of an electron through a saddle-point potential in a magnetic field"*, Phys. Rev. B **36**, 7969–7976, Nov 1987.

[Feve 07] G. Fève, A. Mahé, J.-M. Berroir, T. Kontos, B. Plaçais, D. C. Glattli, A. Cavanna, B. Etienne, and Y. Jin, *"An On-Demand Coherent Single-Electron Source"*, Science **316**, 1169, May 2007.

[Fisc 16] M. H. Fischer, A. Vaezi, A. Manchon, and E.-A. Kim, *"Spin-torque generation in topological insulator based heterostructures"*, Phys. Rev. B **93**, 125303, Mar 2016.

[Flet] J. D. Fletcher, N. Johnson, E. Locane, P. See, G. A. C. Jones, J. P. Griffiths, I. Farrer, D. A. Ritchie, M. Pepper, P. W. Brouwer, V. Kashcheyevs, and M. Kataoka, *"Classical tomography of single-electron wavepacket energy and time distributions". To be published.*

[Flet 13] J. D. Fletcher, P. See, H. Howe, M. Pepper, S. P. Giblin, J. P. Griffiths, G. A. C. Jones, I. Farrer, D. A. Ritchie, T. J. B. M. Janssen, and M. Kataoka, *"Clock-Controlled Emission of Single-Electron Wave Packets in a Solid-State Circuit"*, Phys. Rev. Lett. **111**, 216807, Nov 2013.

[Frie 10] J. R. Friedman and M. P. Sarachik, *"Single-Molecule Nanomagnets"*, Annual Review of Condensed Matter Physics **1**, 109–128, Apr 2010.

[Fu 07] L. Fu, C. L. Kane, and E. J. Mele, *"Topological Insulators in Three Dimensions"*, Phys. Rev. Lett. **98**, 106803, Mar 2007.

[Fuec 10] M. Fuechsle, S. Mahapatra, F. A. Zwanenburg, M. Friesen, M. A. Eriksson, and M. Y. Simmons, *"Spectroscopy of few-electron single-crystal silicon quantum dots"*, Nature Nanotechnology **5**, 502–505, Jul 2010.

[Fuji 08] A. Fujiwara, K. Nishiguchi, and Y. Ono, *"Nanoampere charge pump by single-electron ratchet using silicon nanowire metal-oxide-semiconductor field-effect transistor"*, Applied Physics Letters **92**, 042102, Jan 2008.

[Fult 87] T. A. Fulton and G. J. Dolan, *"Observation of single-electron charging effects in small tunnel junctions"*, Phys. Rev. Lett. **59**, 109–112, Jul 1987.

[Gare 13] K. Garello, I. M. Miron, C. O. Avci, F. Freimuth, Y. Mokrousov, S. Blügel, S. Auffret, O. Boulle, G. Gaudin, and P. Gambardella, *"Symmetry and magnitude of spin-orbit torques in ferromagnetic heterostructures"*, Nature Nanotechnology **8**, 587–593, Aug 2013.

[Gatt 11] D. Gatteschi, R. Sessoli, and J. Villain. *Molecular Nanomagnets (Mesoscopic Physics and Nanotechnology)*. Oxford University Press (2011).

[Gren 11] C. Grenier, R. Hervé, G. Fève, and P. Degiovanni, *"Electron quantum optics in quantum Hall edge channels"*, Mod. Phys. Lett. B **25**, 1053–1073, May 2011.

[Guo 97] L. Guo, E. Leobandung, and S. Y. Chou, *"A room-temperature silicon single-electron metal–oxide–semiconductor memory with nanoscale floating-gate and ultranarrow channel"*, Applied Physics Letters **70**, 850–852, Aug 1997.

[Gurv 98] S. A. Gurvitz, *"Rate equations for quantum transport in multidot systems"*, Phys. Rev. B **57**, 6602–6611, Mar 1998.

[Haac 13] G. Haack, M. Moskalets, and M. Büttiker, *"Glauber coherence of single-electron sources"*, Phys. Rev. B **87**, 201302, May 2013.

[Hasa 10] M. Z. Hasan and C. L. Kane, *"Colloquium: Topological insulators"*, Rev. Mod. Phys. **82**, 3045–3067, Nov 2010.

[Hass 07] F. Hassler, G. B. Lesovik, and G. Blatter, *"Effects of Exchange Symmetry on Full Counting Statistics"*, Phys. Rev. Lett. **99**, 076804, Aug 2007.

[Hass 08] F. Hassler, M. V. Suslov, G. M. Graf, M. V. Lebedev, G. B. Lesovik, and G. Blatter, *"Wave-packet formalism of full counting statistics"*, Phys. Rev. B **78**, 165330, Oct 2008.

[Heis 13] M. Heiss, Y. Fontana, A. Gustafsson, G. Wüst, C. Magen, D. D. O'Regan, J. W. Luo, B. Ketterer, S. Conesa-Boj, A. V. Kuhlmann, J. Houel, E. Russo-Averchi, J. R. Morante, M. Cantoni, N. Marzari, J. Arbiol, A. Zunger, R. J. Warburton, and A. Fontcuberta I Morral, *"Self-assembled quantum dots in a nanowire system for quantum photonics"*, Nat. Mat. **12**, 439–444, May 2013.

[Hekk 91] F. Hekking and Y. V. Nazarov, *"Pauli pump for electrons"*, Phys. Rev. B **44**, 9110–9113, Oct 1991.

[Henn 99] M. Henny, S. Oberholzer, C. Strunk, T. Heinzel, K. Ensslin, M. Holland, and C. Schönenberger, *"The Fermionic Hanbury Brown and Twiss Experiment"*, Science **284**, 296–298, Apr 1999.

[Herm 13] C. F. Hermanns, M. Bernien, A. Krüger, C. Schmidt, S. T. Waßerroth, G. Ahmadi, B. W. Heinrich, M. Schneider, P. W. Brouwer, K. J. Franke, E. Weschke, and W. Kuch, *"Magnetic Coupling of* $Gd_3\mathbf{N}@\mathbf{C}_{80}$ *Endohedral Fullerenes to a Substrate"*, Phys. Rev. Lett. **111**, 167203, Oct 2013.

[Hoff 15] A. Hoffmann and S. D. Bader, *"Opportunities at the Frontiers of Spintronics"*, Phys. Rev. Applied **4**, 047001, Oct 2015.

[Hong 87] C. K. Hong, Z. Y. Ou, and L. Mandel, *"Measurement of subpicosecond time intervals between two photons by interference"*, Phys. Rev. Lett. **59**, 2044–2046, Nov 1987.

[Hsie 09a] D. Hsieh, Y. Xia, D. Qian, L. Wray, J. H. Dil, F. Meier, J. Osterwalder, L. Patthey, J. G. Checkelsky, N. P. Ong, A. V. Fedorov, H. Lin, A. Bansil, D. Grauer, Y. S. Hor, R. J. Cava, and M. Z. Hasan, *"A tunable topological insulator in the spin helical Dirac transport regime"*, Nature **460**, 1101–1105, Aug 2009.

[Hsie 09b] D. Hsieh, Y. Xia, L. Wray, D. Qian, A. Pal, J. H. Dil, J. Osterwalder, F. Meier, G. Bihlmayer, C. L. Kane, Y. S. Hor, R. J. Cava, and M. Z. Hasan, *"Observation of Unconventional Quantum Spin Textures in Topological Insulators"*, Science **323**, 919–922, Feb 2009.

[Huan 15] C. Huang, A. V. Rudnev, W. Hong, and T. Wandlowski, *"Break junction under electrochemical gating: testbed for single-molecule electronics"*, Chem. Soc. Rev. **44**, 889–901, Jan 2015.

[Iked 08] S. Ikeda, J. Hayakawa, Y. Ashizawa, Y. M. Lee, K. Miura, H. Hasegawa, M. Tsunoda, F. Matsukura, and H. Ohno, *"Tunnel magnetoresistance of 604% at 300K by suppression of Ta diffusion in CoFeB/MgO/CoFeB pseudo-spin-*

valves annealed at high temperature", Applied Physics Letters **93**, 082508, Aug 2008.

[Imry 99] Y. Imry and R. Landauer, *"Conductance viewed as transmission"*, Rev. Mod. Phys. **71**, S306–S312, Mar 1999.

[Ji 03] Y. Ji, Y. Chung, D. Sprinzak, M. Heiblum, D. Mahalu, and H. Shtrikman, *"An electronic Mach-Zehnder interferometer"*, Nature **422**, 415–418, Mar 2003.

[John 17] N. Johnson, J. D. Fletcher, D. A. Humphreys, P. See, J. P. Griffiths, G. A. C. Jones, I. Farrer, D. A. Ritchie, M. Pepper, T. J. B. M. Janssen, and M. Kataoka, *"Ultrafast voltage sampling using single-electron wavepackets"*, Applied Physics Letters **110**, 102105, Feb 2017.

[Jull 14] T. Jullien, P. Roulleau, B. Roche, A. Cavanna, Y. Jin, and D. C. Glattli, *"Quantum tomography of an electron"*, Nature **514**, 603–607, Oct 2014.

[Kaes 08] B. Kaestner, V. Kashcheyevs, S. Amakawa, M. D. Blumenthal, L. Li, T. J. B. M. Janssen, G. Hein, K. Pierz, T. Weimann, U. Siegner, and H. W. Schumacher, *"Single-parameter nonadiabatic quantized charge pumping"*, Phys. Rev. B **77**, 153301, Apr 2008.

[Kaes 09] B. Kaestner, C. Leicht, V. Kashcheyevs, K. Pierz, U. Siegner, and H. W. Schumacher, *"Single-parameter quantized charge pumping in high magnetic fields"*, Applied Physics Letters **94**, 012106, Jan 2009.

[Kahl 12] S. Kahle, Z. Deng, N. Malinowski, C. Tonnoir, A. Forment-Aliaga, N. Thontasen, G. Rinke, D. Le, V. Turkowski, T. S. Rahman, S. Rauschenbach, M. Ternes, and K. Kern, *"The Quantum Magnetism of Individual Manganese-12-Acetate Molecular Magnets Anchored at Surfaces"*, Nano Letters **12**, 518–521, Dec 2012.

[Kash 17] V. Kashcheyevs and P. Samuelsson, *"Classical-to-quantum crossover in electron on-demand emission"*, Phys. Rev. Lett. **95**, 245424, Jun 2017.

[Kast 92] M. A. Kastner, *"The single-electron transistor"*, Rev. Mod. Phys., **64**, 849–858, Jul 1992.

[Kata 16a] M. Kataoka, N. Johnson, C. Emary, P. See, J. P. Griffiths, G. A. C. Jones, I. Farrer, D. A. Ritchie, M. Pepper, and T. J. B. M. Janssen, *"Time-of-Flight Measurements of Single-Electron Wave Packets in Quantum Hall Edge States"*, Phys. Rev. Lett. **116**, 126803, Mar 2016.

[Kata 16b] M. Kataoka, J. D. Fletcher, and N. Johnson, *"Time-resolved single-electron wave-packet detection"*, Phys. Status Solidi B **254**, 1600547, (2016).

[Kell 08] M. W. Keller, *"Current status of the quantum metrology triangle"*, Metrologia **45**, 102, Jan 2008.

[Kies 02] H. Kiesel, A. Renz, and F. Hasselbach, *"Observation of Hanbury Brown-Twiss anticorrelations for free electrons"*, Nature **418**, 392–394, Jul 2002.

[Kim 13] J. Kim, J. Sinha, M. Hayashi, M. Yamanouchi, S. Fukami, T. Suzuki, S. Mitani, and H. Ohno, *"Layer thickness dependence of the current-induced effective field vector in Ta—CoFeB—MgO"*, Nature Materials **12**, 240–245, Mar 2013.

[Kimm 16] L. Kimme, B. Rosenow, and A. Brataas, *"Backscattering in helical edge states from a magnetic impurity and Rashba disorder"*, Phys. Rev. B **93**, 081301, Feb 2016.

[Kita 09] A. Kitaev, *"Periodic table for topological insulators and superconductors"*, AIP Conference Proceedings **1134**, 22–30, May 2009.

[Klei 96] D. L. Klein, P. L. McEuen, J. E. B. Katari, R. Roth, and A. P. Alivisatos, *"An approach to electrical studies of single nanocrystals"*, Applied Physics Letters **68**, 2574–2576, Aug 1996.

[Klei 97] D. L. Klein, R. Roth, A. K. L. Lim, A. P. Alivisatos, and P. L. McEuen, *"A single-electron transistor made from a cadmium selenide nanocrystal"*, Nature **389**, 699–701, Oct 1997.

[Knob 03] R. G. Knobel and A. N. Cleland, *"Nanometre-scale displacement sensing using a single electron transistor"*, Nature **424**, 291–293, Jul 2003.

[Koni 03] J. König and J. Martinek, *"Interaction-Driven Spin Precession in Quantum-Dot Spin Valves"*, Phys. Rev. Lett. **90**, 166602, Apr 2003.

[Koni 07] M. König, S. Wiedmann, C. Brüne, A. Roth, H. Buhmann, L. W. Molenkamp, X.-L. Qi, and S.-C. Zhang, *"Quantum Spin Hall Insulator State in HgTe Quantum Wells"*, Science **318**, 766, Nov 2007.

[Koni 08] M. König, H. Buhmann, L. W. Molenkamp, T. Hughes, C.-X. Liu, X.-L. Qi, and S.-C. Zhang, *"The Quantum Spin Hall Effect: Theory and Experiment"*, Journal of the Physical Society of Japan **77**, 031007, Mar 2008.

[Koro 92] A. N. Korotkov, D. V. Averin, K. K. Likharev, S. A. Vasenko, and M. Devoret.

Single-Electron Transistors as Ultrasensitive Electrometers, 45–59. Springer Berlin Heidelberg (1992).

[Koss 72] A. Kossakowski, *"On quantum statistical mechanics of non-Hamiltonian systems"*, Reports on Mathematical Physics **3**, 247–274, Dec 1972.

[Lafa 91] P. Lafarge, H. Pothier, E. R. Williams, D. Esteve, C. Urbina, and M. H. Devoret, *"Direct observation of macroscopic charge quantization"*, Zeitschrift für Physik B Condensed Matter **85**, 327–332, Oct 1991.

[Leso 89] G. B. Lesovik, *"Excess quantum noise in 2D ballistic point contacts"*, JETP **49**, 592, May 1989.

[Likh 85] K. K. Likharev and A. B. Zorin, *"Theory of the Bloch-wave oscillations in small Josephson junctions"*, Journal of Low Temperature Physics **59**, 347–382, May 1985.

[Lind 14] J. Linder, *"Improved domain-wall dynamics and magnonic torques using topological insulators"*, Phys. Rev. B **90**, 041412, Jul 2014.

[Lind 76] G. Lindblad, *"On the generators of quantum dynamical semigroups"*, Communications in Mathematical Physics **48**, 119–130, Jun 1976.

[Liti 17] D. Litinski, P. W. Brouwer, and M. Filippone, *"Interacting mesoscopic capacitor out of equilibrium"*, Phys. Rev. B **96**, 085429, Aug 2017.

[Liu 11] L. Liu, T. Moriyama, D. C. Ralph, and R. A. Buhrman, *"Spin-Torque Ferromagnetic Resonance Induced by the Spin Hall Effect"*, Phys. Rev. Lett. **106**, 036601, Jan 2011.

[Liu 12] L. Liu, C.-F. Pai, Y. Li, H. W. Tseng, D. C. Ralph, and R. A. Buhrman, *"Spin-Torque Switching with the Giant Spin Hall Effect of Tantalum"*, Science **336**, 555–558, Oct 2012.

[Lu 07] W. Lu and C. M. Lieber, *"Nanoelectronics from the bottom up"*, Nature Materials **6**, 841–850, Nov 2007.

[Lund 12] A. M. Lunde and G. Platero, *"Helical edge states coupled to a spin bath: Current-induced magnetization"*, Phys. Rev. B **86**, 035112, Jul 2012.

[Maci 09] J. Maciejko, C. Liu, Y. Oreg, X.-L. Qi, C. Wu, and S.-C. Zhang, *"Kondo Effect in the Helical Edge Liquid of the Quantum Spin Hall State"*, Phys. Rev. Lett. **102**, 256803, Jun 2009.

[Mahf 12] F. Mahfouzi, N. Nagaosa, and B. K. Nikolić, *"Spin-Orbit Coupling Induced Spin-Transfer Torque and Current Polarization in Topological-Insulator/Ferromagnet Vertical Heterostructures"*, Phys. Rev. Lett. **109**, 166602, Oct 2012.

[Mahf 16] F. Mahfouzi, B. K. Nikolić, and N. Kioussis, *"Antidamping spin-orbit torque driven by spin-flip reflection mechanism on the surface of a topological insulator: A time-dependent nonequilibrium Green function approach"*, Phys. Rev. B **93**, 115419, Mar 2016.

[Mala 15] L. Malavolti, V. Lanzilotto, S. Ninova, L. Poggini, I. Cimatti, B. Cortigiani, L. Margheriti, D. Chiappe, E. Otero, P. Sainctavit, F. Totti, A. Cornia, M. Mannini, and R. Sessoli, *"Magnetic Bistability in a Submonolayer of Sublimated Fe4 Single-Molecule Magnets"*, Nano Letters **15**, 535–541, Dec 2015.

[Mann 09] M. Mannini, F. Pineider, P. Sainctavit, C. Danieli, E. Otero, C. Sciancalepore, A. M. Talarico, M.-A. Arrio, A. Cornia, D. Gatteschi, and R. Sessoli, *"Magnetic memory of a single-molecule quantum magnet wired to a gold surface"*, Nature Materials **8**, 194–197, Mar 2009.

[Marg 09] L. Margheriti, M. Mannini, L. Sorace, L. Gorini, D. Gatteschi, A. Caneschi, D. Chiappe, R. Moroni, F. B. de Mongeot, A. Cornia, F. M. Piras, A. Magnani, and R. Sessoli, *"Thermal Deposition of Intact Tetrairon(III) Single-Molecule Magnets in High-Vacuum Conditions"*, Small **5**, 1460–1466, Mar 2009.

[Marg 17] A. Marguerite, E. Bocquillon, J.-M. Berroir, B. Plaçais, A. Cavanna, Y. Jin, P. Degiovanni, and G. Fève, *"Two-particle interferometry in quantum Hall edge channels"*, Physica Status Solidi B **254**, 1600618, Dec 2017.

[Mart 15] J. Martínez-Blanco, C. Nacci, S. C. Erwin, K. Kanisawa, E. Locane, M. Thomas, F. von Oppen, P. W. Brouwer, and S. Fölsch, *"Gating a single-molecule transistor with individual atoms"*, Nat. Phys. **11**, 640–644, Aug 2015.

[Mart 92] T. Martin and R. Landauer, *"Wave-packet approach to noise in multichannel mesoscopic systems"*, Phys. Rev. B **45**, 1742–1755, Jan 1992.

[Mell 14] A. R. Mellnik, J. S. Lee, A. Richardella, J. L. Grab, P. J. Mintun, M. H. Fischer, A. Vaezi, A. Manchon, E.-A. Kim, N. Samarth, and D. C. Ralph, *"Spin-transfer torque generated by a topological insulator"*, Nature **511**, 449–451, Jul 2014.

[Meng 14] Q. Meng, S. Vishveshwara, and T. L. Hughes, *"Spin-transfer torque and electric current in helical edge states in quantum spin Hall devices"*, Phys. Rev. B **90**, 205403, Nov 2014.

[Milt 10] M. J. T. Milton, J. M. Williams, and A. B. Forbes, *"The quantum metrology triangle and the redefinition of the SI ampere and kilogram; analysis of a reduced set of observational equations"*, Metrologia **47**, 279–286, Jun 2010.

[Miro 11] I. M. Miron, K. Garello, G. Gaudin, P.-J. Zermatten, M. V. Costache, S. Auffret, S. Bandiera, B. Rodmacq, A. Schuhl, and P. Gambardella, *"Perpendicular switching of a single ferromagnetic layer induced by in-plane current injection"*, Nature **476**, 189–193, Aug 2011.

[Misi 17] M. Misiorny, G. Fève, and J. Splettstoesser, *"Shaping charge excitations in chiral edge states with a time-dependent gate voltage"*, arXiv:1711.00119, Oct 2017.

[Mohr 16] P. J. Mohr, D. B. Newell, and B. N. Taylor, *"CODATA recommended values of the fundamental physical constants: 2014"*, Rev. Mod. Phys. **88**, 035009, Sep 2016.

[Moor 98] G. E. Moore, *"Cramming More Components Onto Integrated Circuits"*, Proceedings of the IEEE **86**, 82–85, Jan 1998.

[Mosk 08] M. Moskalets, P. Samuelsson, and M. Büttiker, *"Quantized Dynamics of a Coherent Capacitor"*, Phys. Rev. Lett. **100**, 086601, Feb 2008.

[Murr 00] C. B. Murray, , C. R. Kagan, and M. G. Bawendi, *"Synthesis and Characterization of Monodisperse Nanocrystals and Close-Packed Nanocrystal Assemblies"*, Annual Review of Materials Science **30**, 545–610, Aug 2000.

[Naza 09] Y. V. Nazarov and Y. M. Blanter. *Quantum Transport: Introduction to Nanoscience*. Cambridge University Press (2009).

[Naza 93] Y. V. Nazarov, *"Quantum interference, tunnel junctions and resonant tunneling interferometer"*, Physica B: Condensed Matter **189**, 57–69, Jun 1993.

[Ndia 17] P. B. Ndiaye, C. A. Akosa, M. H. Fischer, A. Vaezi, E.-A. Kim, and A. Manchon, *"Dirac spin-orbit torques and charge pumping at the surface of topological insulators"*, Phys. Rev. B **96**, 014408, Jul 2017.

[Nede 06] I. Neder, M. Heiblum, Y. Levinson, D. Mahalu, and V. Umansky, *"Unexpected Behavior in a Two-Path Electron Interferometer"*, Phys. Rev. Lett., **96**, 016804, Jan 2006.

[Nede 07a] I. Neder, M. Heiblum, D. Mahalu, and V. Umansky, *"Entanglement, Dephasing, and Phase Recovery via Cross-Correlation Measurements of Electrons"*, Phys. Rev. Lett. **98**, 036803, Jan 2007.

[Nede 07b] I. Neder, N. Ofek, Y. Chung, M. Heiblum, D. Mahalu, and V. Umansky, *"Interference between two indistinguishable electrons from independent sources"*, Nature **448**, 333–337, Jul 2007.

[Novo 04] K. S. Novoselov, A. K. Geim, S. V. Morozov, D. Jiang, Y. Zhang, S. V. Dubonos, I. V. Grigorieva, and A. A. Firsov, *"Electric Field Effect in Atomically Thin Carbon Films"*, Science **306**, 666–669, Oct 2004.

[Nowa 13] K. C. Nowack, E. M. Spanton, M. Baenninger, M. König, J. R. Kirtley, B. Kalisky, C. Ames, P. Leubner, C. Brüne, H. Buhmann, L. W. Molenkamp, D. Goldhaber-Gordon, and K. A. Moler, *"Imaging currents in HgTe quantum wells in the quantum spin Hall regime"*, Nature Materials **12**, 787–791, Sep 2013.

[Ohni 98] H. Ohnishi, Y. Kondo, and K. Takayanagi, *"Quantized conductance through individual rows of suspended gold atoms"*, Nature **395**, 780–783, Oct 1998.

[Oliv 99] W. D. Oliver, J. Kim, R. C. Liu, and Y. Yamamoto, *"Hanbury Brown and Twiss-Type Experiment with Electrons"*, Science **284**, 299–301, Apr 1999.

[Olkh 08] S. Ol'khovskaya, J. Splettstoesser, M. Moskalets, and M. Büttiker, *"Shot Noise of a Mesoscopic Two-Particle Collider"*, Phys. Rev. Lett. **101**, 166802, Oct 2008.

[Ower 15] S. Owerre and J. Nsofini, *"A toy model for quantum spin Hall effect"*, Solid State Communications **218**, 35–39, Sep 2015.

[Pash 00] Y. A. Pashkin, Y. Nakamura, and J. S. Tsai, *"Room-temperature Al single-electron transistor made by electron-beam lithography"*, Applied Physics Letters **76**, 2256–2258, Apr 2000.

[Peko 08] J. P. Pekola, J. J. Vartiainen, M. Möttönen, O.-P. Saira, M. Meschke, and D. V. Averin, *"Hybrid single-electron transistor as a source of quantized electric current"*, Nature Physics **4**, 120–124, Feb 2008.

[Pi 10] U. H. Pi, K. W. Kim, J. Y. Bae, S. C. Lee, Y. J. Cho, K. S. Kim, and S. Seo, *"Tilting of the spin orientation induced by Rashba effect in ferromagnetic metal layer"*, Applied Physics Letters **97**, 162507, Oct 2010.

[Piqu 04] F. Piquemal, A. Bounouh, L. Devoille, N. Feltin, O. Thevenot, and G. Trapon, *"Fundamental electrical standards and the quantum metrological triangle"*, Comptes Rendus Physique **5**, 857–879, Oct 2004.

[Pono 08] L. A. Ponomarenko, F. Schedin, M. I. Katsnelson, R. Yang, E. W. Hill, K. S.

Novoselov, and A. K. Geim, *"Chaotic Dirac Billiard in Graphene Quantum Dots"*, Science **320**, 356, Apr 2008.

[Post 01] H. W. C. Postma, T. Teepen, Z. Yao, M. Grifoni, and C. Dekker, *"Carbon Nanotube Single-Electron Transistors at Room Temperature"*, Science **293**, 76–79, Jul 2001.

[Poth 92] H. Pothier, P. Lafarge, C. Urbina, D. Esteve, and M. H. Devoret, *"Single-Electron Pump Based on Charging Effects"*, Europhys. Lett. **17**, 249, Jan 1992.

[Prob 15] B. Probst, P. Virtanen, and P. Recher, *"Controlling spin polarization of a quantum dot via a helical edge state"*, Phys. Rev. B **92**, 045430, Jul 2015.

[Ralp 08] D. Ralph and M. Stiles, *"Spin transfer torques"*, Journal of Magnetism and Magnetic Materials **320**, 1190–1216, Apr 2008.

[Reza 16] A. K. Reza, X. Fong, Z. A. Azim, and K. Roy, *"Modeling and Evaluation of Topological Insulator/Ferromagnet Heterostructure-Based Memory"*, IEEE Transactions on Electron Devices **63**, 1359–1367, Mar 2016.

[Rous 17] B. Roussel, C. Cabart, G. Fève, E. Thibierge, and P. Degiovanni, *"Electron quantum optics as quantum signal processing"*, Physica Status Solidi B **254**, 1600621, Jan 2017.

[Ryu 13] K.-S. Ryu, L. Thomas, S.-H. Yang, and S. Parkin, *"Chiral spin torque at magnetic domain walls"*, Nature Nanotechnology **8**, 527–533, Jul 2013.

[Samu 04] P. Samuelsson, E. V. Sukhorukov, and M. Büttiker, *"Two-Particle Aharonov-Bohm Effect and Entanglement in the Electronic Hanbury Brown˘Twiss Setup"*, Phys. Rev. Lett. **92**, 026805, Jan 2004.

[Sche 12] H. Scherer and B. Camarota, *"Quantum metrology triangle experiments: a status review"*, Measurement Science and Technology **23**, 124010, Dec 2012.

[Schn 08] A. P. Schnyder, S. Ryu, A. Furusaki, and A. W. W. Ludwig, *"Classification of topological insulators and superconductors in three spatial dimensions"*, Phys. Rev. B **78**, 195125, Nov 2008.

[Schn 09] A. P. Schnyder, S. Ryu, A. Furusaki, and A. W. W. Ludwig, *"Classification of Topological Insulators and Superconductors"*, AIP Conference Proceedings **1134**, 10–21, May 2009.

[Scho 98] R. J. Schoelkopf, P. Wahlgren, A. A. Kozhevnikov, P. Delsing, and D. E.

Prober, *"The Radio-Frequency Single-Electron Transistor (RF-SET): A Fast and Ultrasensitive Electrometer"*, Science **280**, 1238, May 1998.

[Schu 97] R. Schuster, E. Buks, M. Heiblum, D. Mahalu, V. Umansky, and H. Shtrikman, *"Phase measurement in a quantum dot via a double-slit interference experiment"*, Nature **385**, 417–420, Jan 1997.

[Selz 06] Y. Selzer and D. L. Allara, *"Single-Molecule Electrical Junctions"*, Annual Review of Physical Chemistry **57**, 593–623, May 2006.

[Silv 00] P. G. Silvestrov and Y. Imry, *"Towards an Explanation of the Mesoscopic Double-Slit Experiment: A New Model for Charging of a Quantum Dot"*, Phys. Rev. Lett. **85**, 2565–2568, Sep 2000.

[Silv 16] P. G. Silvestrov, P. Recher, and P. W. Brouwer, *"Noiseless manipulation of helical edge state transport by a quantum magnet"*, Phys. Rev. B **93**, 205130, May 2016.

[Slon 96] J. Slonczewski, *"Current-driven excitation of magnetic multilayers"*, Journal of Magnetism and Magnetic Materials **159**, L1–L7, Jun 1996.

[Smit 97] S. W. Smith. *The Scientist & Engineer's Guide to Digital Signal Processing.* California Technical Pub (1997).

[Song 15] X.-X. Song, Z.-Z. Zhang, J. You, D. Liu, H.-O. Li, G. Cao, M. Xiao, and G.-P. Guo, *"Temperature dependence of Coulomb oscillations in a few-layer two-dimensional WS_2 quantum dot"*, Scientific Reports **5**, 16113, Nov 2015.

[Swit 99] M. Switkes, C. M. Marcus, K. Campman, and A. C. Gossard, *"An Adiabatic Quantum Electron Pump"*, Science **283**, 1905–1908, Mar 1999.

[Tana 11] Y. Tanaka, A. Furusaki, and K. A. Matveev, *"Conductance of a Helical Edge Liquid Coupled to a Magnetic Impurity"*, Phys. Rev. Lett. **106**, 236402, Jun 2011.

[Tans 97] S. J. Tans, M. H. Devoret, H. Dai, A. Thess, R. E. Smalley, L. J. Geerligs, and C. Dekker, *"Individual single-wall carbon nanotubes as quantum wires"*, Nature **386**, 474–477, Apr 1997.

[Thib 16] E. Thibierge, D. Ferraro, B. Roussel, C. Cabart, A. Marguerite, G. Fève, and P. Degiovanni, *"Two-electron coherence and its measurement in electron quantum optics"*, Phys. Rev. B **93**, 081302, Feb 2016.

[Thou 77] D. J. Thouless, *"Maximum Metallic Resistance in Thin Wires"*, Phys. Rev. Lett. **39**, 1167–1169, Oct 1977.

[Tser 12] Y. Tserkovnyak and D. Loss, *"Thin-Film Magnetization Dynamics on the Surface of a Topological Insulator"*, Phys. Rev. Lett. **108**, 187201, Apr 2012.

[Ubbe 15] N. Ubbelohde, F. Hohls, V. Kashcheyevs, T. Wagner, L. Fricke, B. Kästner, K. Pierz, H. W. Schumacher, and R. J. Haug, *"Partitioning of on-demand electron pairs"*, Nature Nanotechnology **10**, 46–49, Jan 2015.

[Vayr 14] J. I. Väyrynen, M. Goldstein, Y. Gefen, and L. I. Glazman, *"Resistance of helical edges formed in a semiconductor heterostructure"*, Phys. Rev. B **90**, 115309, Sep 2014.

[Vayr 16] J. I. Väyrynen, F. Geissler, and L. I. Glazman, *"Magnetic moments in a helical edge can make weak correlations seem strong"*, Phys. Rev. B **93**, 241301, Jun 2016.

[Wahl 14] C. Wahl, J. Rech, T. Jonckheere, and T. Martin, *"Interactions and Charge Fractionalization in an Electronic Hong-Ou-Mandel Interferometer"*, Phys. Rev. Lett. **112**, 046802, Jan 2014.

[Wald 15] J. Waldie, P. See, V. Kashcheyevs, J. P. Griffiths, I. Farrer, G. A. C. Jones, D. A. Ritchie, T. J. B. M. Janssen, and M. Kataoka, *"Measurement and control of electron wave packets from a single-electron source"*, Phys. Rev. B **92**, 125305, Sep 2015.

[Wang 15] Y. Wang, P. Deorani, K. Banerjee, N. Koirala, M. Brahlek, S. Oh, and H. Yang, *"Topological Surface States Originated Spin-Orbit Torques in* Bi_2Se_3*"*, Phys. Rev. Lett. **114**, 257202, Jun 2015.

[Wrig 08] S. J. Wright, M. D. Blumenthal, G. Gumbs, A. L. Thorn, M. Pepper, T. J. B. M. Janssen, S. N. Holmes, D. Anderson, G. A. C. Jones, C. A. Nicoll, and D. A. Ritchie, *"Enhanced current quantization in high-frequency electron pumps in a perpendicular magnetic field"*, Phys. Rev. B **78**, 233311, Dec 2008.

[Yao 99] Z. Yao, H. W. C. Postma, L. Balents, and C. Dekker, *"Carbon nanotube intramolecular junctions"*, Nature **402**, 273–276, Nov 1999.

[Zuti 04] I. Zutić, J. Fabian, and S. Das Sarma, *"Spintronics: Fundamentals and applications"*, Rev. Mod. Phys. **76**, 323–410, Apr 2004.

Acknowledgements

First and foremost, I would like to thank my supervisor Piet Brouwer, for the opportunity to work in his group and for being so patient, accessible, and exceptionally kind. I greatly appreciate having been able to experience Piet's insights, intuition for physics, his quick mind, and, importantly for supervision, his ability to assume different ways of thinking.

I am grateful to Felix von Oppen for refereeing this thesis and for initiating the project on the single-molecule transistor.

I also thank Jesús Martínez-Blanco and Stefan Fölsch from the Paul Drude Institute for the opportunity to collaborate on this interesting project, as well as Mark Thomas for the teamwork.

I would also like to thank Slava Kashcheyevs for coming up with an idea for my last project and to Jon Fletcher and Masaya Kataoka from the National Physics Laboratory (UK) for the fruitful collaboration on this project.

I gratefully acknowledge financial support by the CRC 658 of the German Research Foundation.

I would like to thank everyone at the Dahlem Center for making the day-to-day interactions so enjoyable. A very warm thank you to the most wonderful office mates I could have wished for—Max and Max (in no particular order). I will miss you! I also thank Björn Sbierski, Maresa Rieder, Anton Bruch, Max Geier, Laura Baez, Christian Fräßdorf, Christian Klöckner, Sergio Acero, Daniel Litinski, Thomas Kiendl, Jonas Sonnenschein, Kevin Madsen, Martin Schneider, Emil Bergholtz, Flore Kunst, Jörg Behrmann, Mark Thomas, Alexandra Junck, Silvia Kusminskiy, Luka Trifunovic, Zhao Liu, Christoph Karrasch, Johannes Reuther, Yuval Vinkler, Rico Schmidt, Clemens Meyer zu Rheda, Dario Bercioux, and Michele Filippone for making these four years very memorable. Thank you to Gabriele Hermann, Marietta Wissmann, and Annette Schumann-Welde, not only for helping with the formalities, but also for the friendly chats and the kind attitude.

I am grateful to my family, especially my parents for encouraging all my interests and my little brother for giving me basketball lessons to take my mind off the PhD. I also thank Elvijs for his friendship.

Finally, I want to thank Eslam, whom by an incredible stroke of luck I am able to call my husband, for his never-ending support.

Curriculum Vitae

For reasons of data protection, the curriculum vitae is not published in the online version

Publications

Publications that constitute the contents of this thesis:

- E. Locane and P. W. Brouwer,
  "Current-induced switching of magnetic molecules on topological insulator surfaces",
  Phys. Rev. B **95**, 125437 (2017), https://doi.org/10.1103/PhysRevB.95.125437
  [Chapter 2].
  The initial idea of the project was proposed by P. W. Brouwer as part of the CRC 658 of the German Research Foundation. I contributed in performing the calculations, obtaining results and figures, and writing the manuscript.

- E. Locane, P. W. Brouwer, and V. Kashcheyevs,
  "Dynamical scattering of single-electron wave packets" (to be published)
  [Chapter 3].
  The initial idea of the project was proposed by V. Kashcheyevs. I contributed in performing the calculations, obtaining results and figures, and writing the manuscript.

- J. Martínez-Blanco, C. Nacci, S. C. Erwin, K. Kanisawa, E. Locane, M. Thomas, F. von Oppen, P. W. Brouwer, and S. Fölsch,
  "Gating a single-molecule transistor with individual atoms",
  Nat. Phys. **11**, 640–644 (2015), http://doi.org/10.1038/nphys3385
  [Chapter 4].
  The STM experiment and the experimental data analysis was performed by J. Martínez-Blanco, C. Nacci, and S. Fölsch. I contributed in performing the generic model calculations of the coupled electronic and conformational dynamics and in co-writing the theory parts of the manuscript.

Other publications:

- J. D. Fletcher, N. Johnson, E. Locane, P. See, G. A. C. Jones, J. P. Griffiths, I. Farrer, D. A. Ritchie, M. Pepper, P. W. Brouwer, V. Kashcheyevs, and M. Kataoka,
  "Classical tomography of single-electron wavepacket energy and time distributions"
  (to be published).